DCPT-04-100
IPPP-04-50

August 27th, 12am UK time

The Case for positron polarisation at the Linear Collider*

G. Moortgat-Pick[1**], B. Ananthanarayan[2], A.A. Babich[3], A. Bartl[4], J. Clarke[5], J.E. Clendenin[6], M. Diehl[7], H. Eberl[8], K. Floettmann[7**], H. Fraas[9], S. Heinemeyer[10], S. Hesselbach[4,9], T. Hirose[**], K. Hohenwarter-Sodek[4], T. Kernreiter[4], O. Kittel[9], S. Kraml[10], W. Majerotto[8], K. Moenig[18], K. Moffeit[6], S. Moretti[11], T. Nakanishi[**], O. Nachtmann[12], F. Nagel[12], U. Nauenberg[13**], T. Omori[15**], P. Osland[14], A.A. Pankov[3], N. Paver[16**], R. Pitthan[6**], W. Porod[17], P. Richardson[1], Saurabh D. Rindani[18], T.G. Rizzo[6**], P. Schüler[7**], C. Schwanenberger[19] D. Scott[5], J. Sheppard[6**], A. Stahl[20**], H. Steiner[**], G. Weiglein[1], M. Woods[6**], etc. not yet final

[1] *IPPP, University of Durham, U.K.*
[2] *Centre for Theoretical Studies, Indian Institute of Science,Bangalore, 560 012, India*
[3] *Pavel Sukhoi Technical University, Gomel, 246746 Belarus*
[4] *Institut für Theoretische Physik, Universität Wien, Austria*
[5] *Astec, Daresbury Lab, UK*
[6] *Stanford Linear Accelerator Center, Stanford, CA, 94309, USA*
[7] *DESY, Hamburg, Germany*
[8] *Inst. f. Hochenergiephysik, Österr. Akademie d. Wissenschaften, Austria*
[9] *Institut für Theoretische Physik, Universität Würzburg, Am Hubland, D-97074 Würzburg, Germany*
[10] Cern, Theory Division, Switzerland
[11] School of Physics and Astronomy, University of Southampton, Highfield, Southampton SO17 1BJ, UK.
[12] Institut für Theoretische Physik, Philosophenweg 16, 69120 Heidelberg, Germany
[13] University of Colorado, Boulder, USA
[14] Department of Physics, University of Bergen, Allégaten 55, N-5007 Bergen, Norway
[15] KEK, Japan
[16] Dipartimento di Fisica Teorica, Università di Trieste and
Istituto Nazionale di Fisica Nucleare, Sezione di Trieste, Trieste, Italy
[17] Institut für Theoretische Physik, Universität Zürich, Switzerland
[18] Theory Group, Physical Research Laboratory, Navrangpura, Ahmedabad 380 009, India
[19] Physikalisches Institut, Universität Bonn, Nußallee 12, 53112 Bonn, Germany
[20] Desy, Zeuthen, Germany

*For further informations, see `http://www.ippp.dur.ac.uk/~gudrid/power/write-up` .
**Member of Editorial Board

Contents

List of Figures

List of Tables

Chapter 1

Introduction

1.1 General remarks about the structure of couplings

In general the cross section of any process in an $\mathrm{e^+e^-}$ collider can be subdivided according to the initial helicity states (see Tab.1.1):

$$\begin{aligned}\sigma_{P_{e^-}P_{e^+}} &= \frac{1}{4}\{(1+P_{e^-})(1+P_{e^+})\sigma_{\mathrm{RR}} + (1-P_{e^-})(1-P_{e^+})\sigma_{\mathrm{LL}} \\ &\quad + (1+P_{e^-})(1-P_{e^+})\sigma_{\mathrm{RL}} + (1-P_{e^-})(1+P_{e^+})\sigma_{\mathrm{LR}}\}, \end{aligned} \tag{1}$$

where σ_{RL} stands for the cross section of the process when both the electron and the positron beam are 100% polarised in right-handed e^- and left-handed e^+; the cross sections σ_{LR}, σ_{RR} and σ_{LL} are defined analogously. We use the right-handed helicity basis, so that $P_{e^\pm} < 0$ means that the beam is left-handed polarised.

	e^-	e^+		
$\boldsymbol{\sigma}_{\mathbf{RR}}$	$\Rightarrow\ \rightarrow$	$\leftarrow\ \Leftarrow$	$\frac{1+\mathrm{P}_{e^-}}{2}\cdot\frac{1+\mathrm{P}_{e^+}}{2}$	$J_z = 0$
$\boldsymbol{\sigma}_{\mathbf{LL}}$	$\Leftarrow\ \rightarrow$	$\leftarrow\ \Rightarrow$	$\frac{1-\mathrm{P}_{e^-}}{2}\cdot\frac{1-\mathrm{P}_{e^+}}{2}$	
$\boldsymbol{\sigma}_{\mathbf{RL}}$	$\Rightarrow\ \rightarrow$	$\leftarrow\ \Rightarrow$	$\frac{1+\mathrm{P}_{e^-}}{2}\cdot\frac{1-\mathrm{P}_{e^+}}{2}$	$J_z = 1$
$\boldsymbol{\sigma}_{\mathbf{LR}}$	$\Leftarrow\ \rightarrow$	$\leftarrow\ \Leftarrow$	$\frac{1-\mathrm{P}_{e^-}}{2}\cdot\frac{1+\mathrm{P}_{e^+}}{2}$	

Table 1.1: Graphical representation of the various spin configurations in $\mathrm{e^+e^-}$ collisions. The thick arrow represents the direction of motion of the particle and the double-arrow its spin direction. The first column indicates the corresponding cross section, the third column the fraction of this configuration and the last column the total spin assuming a zero orbital angular momentum.

One has to distinguish two cases:
a) in annihilation diagrams the helicities of the incoming beams are coupled to each other, whereas

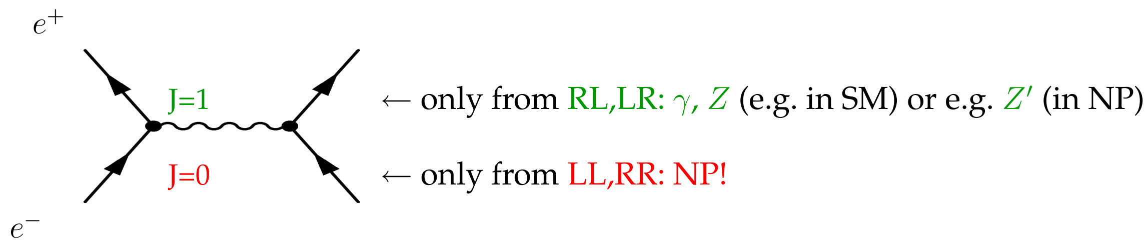

Figure 1: Possible configurations in annihilation diagrams: the helicities of the incoming e^+e^- beams are directly coupled. Within the Standard Model (SM) only the recombination into a vector particle with J=1 is possible, which is given by the LR and RL configurations. New physics (NP) models might allow J=0, which results LL or RR configurations.

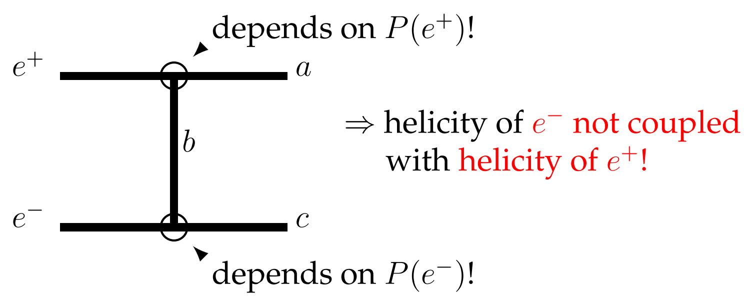

Figure 2: Possible configurations in exchanged diagrams: the helicity of the incoming e beam is directly coupled to the helicity of the final particle and is completely independent of the helicity of the second incoming particle. All possible helicity configurations are therefore possible in principle.

b) in exchanged diagrams the helicities of the incoming beams are directly coupled to the helicities of the final particles, see Fig. 2.

In case a) within the SM only the recombination into a vector particle with the total angular momentum $J = 1$ is possible, i.e. both beams have to carry opposite sign of helicities. New physics (NP) models might allow to produce also scalar particles, so that also $J = 0$ would be allowed, which results in same sign helicities of the incoming beams, see Fig. 1.

In case b) the exchanged diagrams could result in a vector, fermionic or scalar particle; the helicity of the incoming particle is directly coupled to the vertex and is independent of the helicity of the second incoming particle. Therefore all possible helicity configurations are possible in principle, see Fig. 2. Prominent candidates for case b) are single W production, see Fig. 3, where the $e^+W^+\bar{\nu}$ is only influenced by $P(e^+)$, and Bhabha scattering, where the γ, Z exchange in the crossed channel leads to higher cross sections for the LL configuration than the LR configurations, see Table 1.2.

unpolarised	$P_{e^-} = -80\%$	$P_{e^-} = -80\%$, $P_{e^+} = -60\%$	$P_{e^-} = -80\%$, $P_{e^+} = +60\%$
4.50 pb	4.63 pb	4.69 pb	4.58 pb

Table 1.2: Bhabha scattering at $\sqrt{s} = 500$ GeV: due to the γ, Z exchange in the crossed channel all possible helicity configurations are allowed, e.g. the configuration LL leads to higher cross sections than LR.

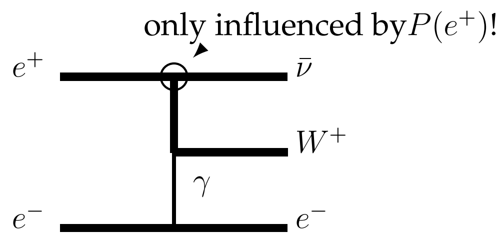

Figure 3: Single W^+ production: vertex $e^+W^+\bar{\nu}$ depends on $P(e^+)$.

	$\sigma_{\rm RL}/\sigma_0$	$\sigma_{\rm LR}/\sigma_0$	$\sigma_{\rm RR}/\sigma_0$	$\sigma_{\rm LL}/\sigma_0$	P_{eff}	$\mathcal{L}_{eff}/\mathcal{L}$
$P_{e^-}=0$, $P_{e^+}=0$	0.25	0.25	0.25	0.25	0.	0.5
$P_{e^-}=-1$, $P_{e^+}=0$	0	0.5	0	0.5	-1	0.5
$P_{e^-}=-0.8$, $P_{e^+}=0$	0.05	0.45	0.05	0.45	-0.8	0.5
$P_{e^-}=-0.8$, $P_{e^+}=+0.6$	0.02	0.72	0.08	0.18	-0.95	0.74

Table 1.3: Effective polarisation and the fraction of colliding particles for some valies of beam polarisation

In the case of $\rm e^+e^-$ annihilation into a vector particle (in the SM this would be $\rm e^+e^- \to \gamma/Z^0$) only the two J=1 configurations $\sigma_{\rm RL}$ and $\sigma_{\rm LR}$ contribute and the cross section for arbitrary beam polarizations is given by

$$\begin{aligned}\sigma_{P_{e^-}P_{e^+}} &= \frac{1+{\rm P}_{e^-}}{2}\,\frac{1-{\rm P}_{e^+}}{2}\,\sigma_{\rm RL} + \frac{1-{\rm P}_{e^-}}{2}\,\frac{1+{\rm P}_{e^+}}{2}\,\sigma_{\rm LR} \\ &= (1-{\rm P}_{e^-}{\rm P}_{e^+})\,\frac{\sigma_{\rm RL}+\sigma_{\rm LR}}{4}\left[1-\frac{{\rm P}_{e^-}-{\rm P}_{e^+}}{1-{\rm P}_{e^+}{\rm P}_{e^-}}\,\frac{\sigma_{\rm LR}-\sigma_{\rm RL}}{\sigma_{\rm LR}+\sigma_{\rm RL}}\right] \\ &= (1-{\rm P}_{e^+}{\rm P}_{e^-})\;\sigma_0\;[1-{\rm P}_{\rm eff}\,{\rm A}_{\rm LR}] \end{aligned} \quad (2)$$

$$\text{with the unpolarized cross section} \qquad \sigma_0 = \frac{\sigma_{\rm RL}+\sigma_{\rm LR}}{4} \quad (3)$$

$$\text{the left-right asymmetry} \qquad {\rm A}_{\rm LR} = \frac{\sigma_{\rm LR}-\sigma_{\rm RL}}{\sigma_{\rm LR}+\sigma_{\rm RL}} \quad (4)$$

$$\text{and the effective polarization} \qquad {\rm P}_{\rm eff} = \frac{{\rm P}_{e^-}-{\rm P}_{e^+}}{1-{\rm P}_{e^+}{\rm P}_{e^-}} \quad (5)$$

Introducing the effective luminosity

$$\mathcal{L}_{eff}/\mathcal{L} = \frac{1}{2}(1-P_{e^-}P_{e^+}), \quad (6)$$

which gives the fraction of colliding particles, eq. (2) can be written as:

$$\sigma_{P_{e^-}P_{e^+}} = 2\,\sigma_0\,\mathcal{L}_{]\{\{}\;[1-{\rm P}_{\rm eff}\,{\rm A}_{\rm LR}]\,. \quad (7)$$

Some values for the effect. polarisation as well as for the effective luminosity are given in Table 1.3, which shows that the fraction of colliding particles can only be enhanced if both beams are polarised. The values of the effective polarization can be read from fig. 4. Notice that the effective polarization is closer to $100\ \%$ than any of the two beam polarizations. Further excellent reference see also [15].

In the experiment one would like to extract the two quantities σ_0 and $\mathrm{A_{LR}}$. This can be done by running the experiment with two different polarizations. One would choose one setup with the electron beam predominantly left-handed and the positron beam right-handed and in the second setup one would reverse both spin directions. The cross sections measured with the two setups are denoted as σ_{-+} and σ_{+-} and are given by:

$$\sigma_{-+} = \frac{1}{4}\left\{(1+|P_{e^-}||P_{e^+}|)(\sigma_{\mathrm{LR}}+\sigma_{\mathrm{RL}}) + (|P_{e^-}|+|P_{e^+}|)(\sigma_{\mathrm{LR}}-\sigma_{\mathrm{RL}})\right\} \tag{8}$$

$$\sigma_{+-} = \frac{1}{4}\left\{(1+|P_{e^-}||P_{e^+}|)(\sigma_{\mathrm{LR}}+\sigma_{\mathrm{RL}}) - (|P_{e^-}|+|P_{e^+}|)(\sigma_{\mathrm{LR}}-\sigma_{\mathrm{RL}})\right\}. \tag{9}$$

It is then

$$\begin{aligned}
\sigma_0 &= \frac{\sigma_{-+}+\sigma_{+-}}{2\,(1+|\mathrm{P}_{e^+}||\mathrm{P}_{e^-}|)} \\
\mathrm{A_{LR}} &= \frac{1}{|\mathrm{P_{eff}}|}\,A_{\mathrm{obs}} = \frac{1}{|\mathrm{P_{eff}}|}\,\frac{\sigma_{-+}-\sigma_{+-}}{\sigma_{-+}+\sigma_{+-}},
\end{aligned} \tag{10}$$

where A_{obs} is the measured left-right asymmetry of processes with partially polarised beams.

Both quantities A_{LR} and σ_0 depend on the beam polarisations. The contribution of the uncertainty of the polarisation measurement to the error is – under the assumption that the errors are completely independent:

$$\frac{\Delta \mathrm{A_{LR}}}{\mathrm{A_{LR}}} = -\frac{\Delta \mathrm{P_{eff}}}{|\mathrm{P_{eff}}|} \tag{11}$$

$$\frac{\Delta \mathrm{P_{eff}}}{|\mathrm{P_{eff}}|} = \frac{x}{(|\mathrm{P}_{e^+}|+|\mathrm{P}_{e^-}|)\ (1+|\mathrm{P}_{e^+}||\mathrm{P}_{e^-}|)}\sqrt{(1-|\mathrm{P}_{e^-}|^2)^2\,P_{e^-}^2+(1-|\mathrm{P}_{e^+}|^2)^2\,P_{e^+}^2} \tag{12}$$

$$\frac{\Delta\sigma_0}{\sigma_0} = \frac{\sqrt{2}\,x}{1+|\mathrm{P}_{e^+}||\mathrm{P}_{e^-}|}\,(|\mathrm{P}_{e^+}|+|\mathrm{P}_{e^-}|) \tag{13}$$

(14)

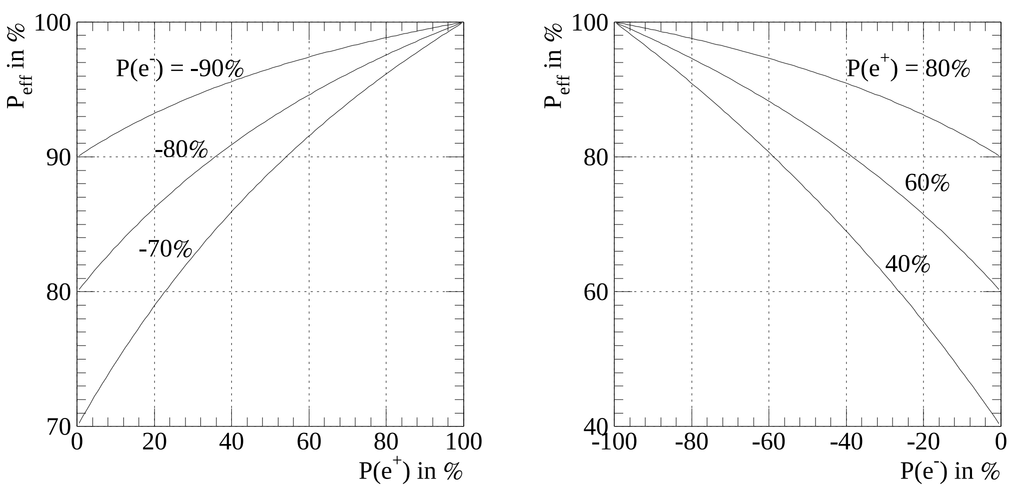

Figure 4: Effective polarization as a function of the beam polarization.

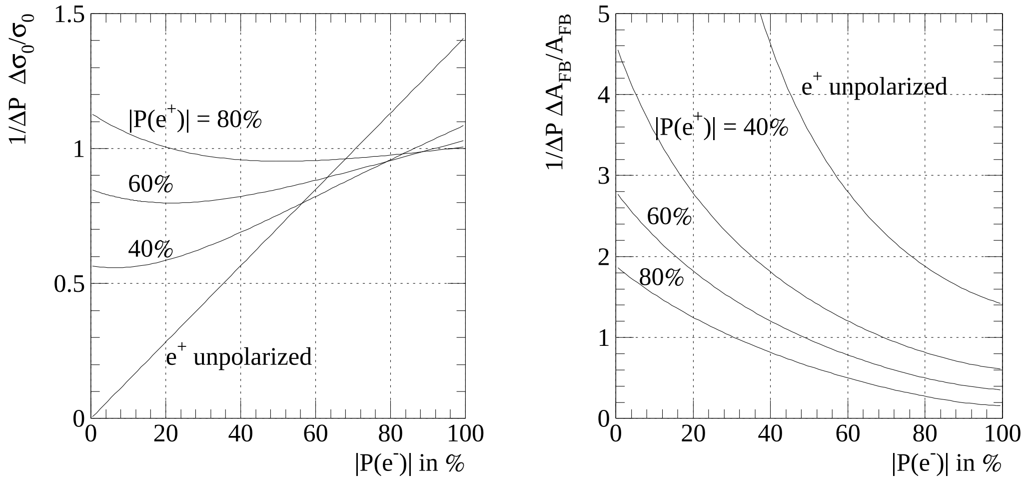

Figure 5: Left: Contribution of the uncertainty on beam polarization on the measurement of the unpolarized cross section. Right: Same for the left-right asymmetry. Both plots are normalized to the polarimeter resolution ΔP which is assumed to be identical for both beams.

Equal relative precision $x := \Delta P_{e^-}/P_{e^-} \sim \Delta P_{e^+}/P_{e^+}$ for the measurement of the two beam polarizations is assumed.

In case that the relative errors of e^- and e^+ are fully correlated, like depolarisation effects from Bremsstrahlung, the errors are given by the linear sum:

$$\frac{\Delta \mathrm{P_{eff}}}{\mathrm{P_{eff}}} = \frac{1 + P_{e^+}P_{e^-}}{1 - P_{e^+}P_{e^-}}\, x \tag{15}$$

$$\frac{\Delta\sigma_0}{\sigma_0} = \frac{2\,x}{1 + |\mathrm{P}_{e^+}||\mathrm{P}_{e^-}|}\,(|\mathrm{P}_{e^+}| + |\mathrm{P}_{e^-}|) \tag{16}$$

The resulting uncertainties are shown in fig. 5. The error contribution from the polarimeter to the unpolarized cross section is rather small. For a polarimeter precision of $0.05\,\%$, it only becomes relevant for data samples with more than $4 \cdot 10^6$ signal events. For an electron beam polarization of $80\,\%$ there is a small improvement in the extraction of the unpolarized cross section due to positron beam polarization. The error introduced in $\mathrm{A_{LR}}$ by the polarization measurement is larger. Without positron beam polarization one is limited by the polarimeter ($0.05\,\%$ precision) for samples with more than 10^6 events. The improvement due to positron beam polarization is substantial. For a positron polarization of $60\,\%$ the error on $\mathrm{A_{LR}}$ is reduced by a factor of 3.8.

1.2 Longitudinally polarised Electrons – Examples from SLD

1.3 Improvement of effective Polarisation – Example: top threshold

J. Kuehn, LC-TH-2001-04

Chapter 2

Physics with Polarisation of e^- and e^+ beam

2.1 Determination of chiral quantum numbers of new physics particles

We demonstrate the importance of having both beams polarised at one example of physics beyond the SM: Supersymmetry is one of the most motivated possibilities for NP. However, even its minimal version, the MSSM, leads to about 105 new free parameters. At future experiments, the LHC and the LC, one has - after detecting signals expected by susy – to determine the Susy parameters as model independent as possible, as well as to prove the underlying Susy assumptions, e.g. that the Susy particles have to carry the same quantum numbers (with the exception of the spin) as their SM partners.

E.g. Susy transformations associate chiral (anti)fermions to scalars $e^-_{L,R} \leftrightarrow \tilde{e}^-_{L,R}$ but $e^+_{L,R} \leftrightarrow \tilde{e}^+_{R,L}$. In order to prove this association the use of both beam polarised is necessary [2]. The process $e^+e^- \to \tilde{e}^+\tilde{e}^-$ occurs via γ and Z exchange in the s–channel and via neutralino $\tilde{\chi}^0_i$ exchange in the t–channel. The association can be directly tested only in the t–channel and the use of polarised beams serves to separate this channel. We demonstrate this by isolation of the pair $\tilde{e}^+_R\tilde{e}^-_L$ by the LL configuration of the initial beams in an example where the selectron masses are close together, $m_{\tilde{e}_L} = 200$ GeV, $m_{\tilde{e}_R} = 195$ GeV so that $\tilde{e}_L$, $\tilde{e}_R$ decay via the same decay channels, directly into $\tilde{e}_{L,R} \to \tilde{\chi}^0_1 e$. At a LC it is possible to measure the selectron masses with an accuracy of about 1 GeV [34], e.g. via invariant mass spectra of the decay products. The other Susy parameters are taken as $M_1 = 100$ GeV, $M_2 = 210$ GeV, $\mu = 400$ GeV, $\tan\beta = 20$. As can be seen from Fig. 1, even extremely high electron polarisation $P(e-) \geq -90\%$ may not be sufficient to disentangle the pairs $\tilde{e}^+_R\tilde{e}^-_L$ and $\tilde{e}^+_L\tilde{e}^-_L$, their cross sections are too close together, $\sigma(e^+e^- \to \tilde{e}^+_R\tilde{e}^-_L) \times BR^2(\tilde{e}^\pm \to \tilde{\chi}^0_1 e^\pm) = 102$ fb, $\sigma(e^+e^- \to \tilde{e}^+_L\tilde{e}^-_L) \times BR^2(\tilde{e}^\pm \to \tilde{\chi}^0_1 e^\pm) = 94$ fb. Even 100% left-handed polarised electron beams may not change this feature.

With $P_{e^-} = -80\%$, $P_{e^+} = -60\%$ ($P(e^+) = -40\%$), however, the pairs are clearly separated and the association to the chiral quantum number may be tested, see Fig. 2: $\sigma(e^+e^- \to \tilde{e}^+_R\tilde{e}^-_L) \times BR^2(\tilde{e}^\pm \to \tilde{\chi}^0_1 e^\pm) = 164$ fb (143 fb), $\sigma(e^+e^- \to \tilde{e}^+_L\tilde{e}^-_L) \times BR^2(\tilde{e}^\pm \to \tilde{\chi}^0_1 e^\pm) = 38$ fb (57 fb). In addition all SM background events, e.g. from W^+W^- are strongly suppressed within this LL polarisation configuration.

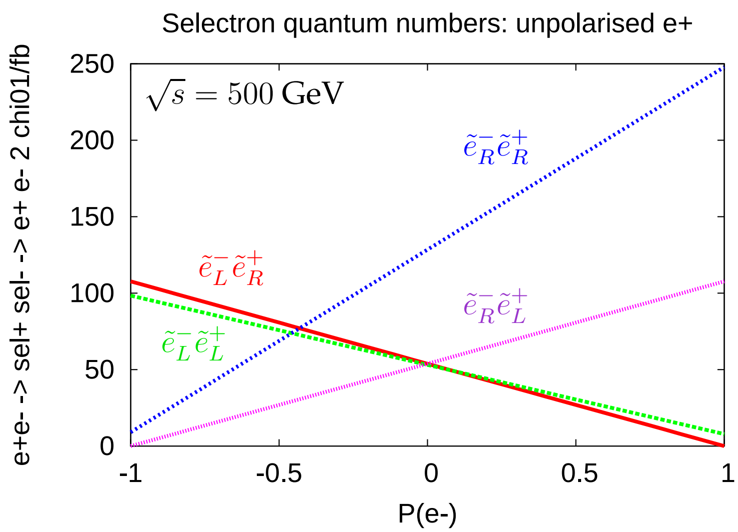

Figure 1: Separation of the selectron pair $\tilde{e}_L^- \tilde{e}_R^+$ in $e^+e^- \rightarrow \tilde{e}^+_{L,R}\tilde{e}^-_{L,R}$ may not be possible, even with extremely high left-handed electron polarisation.

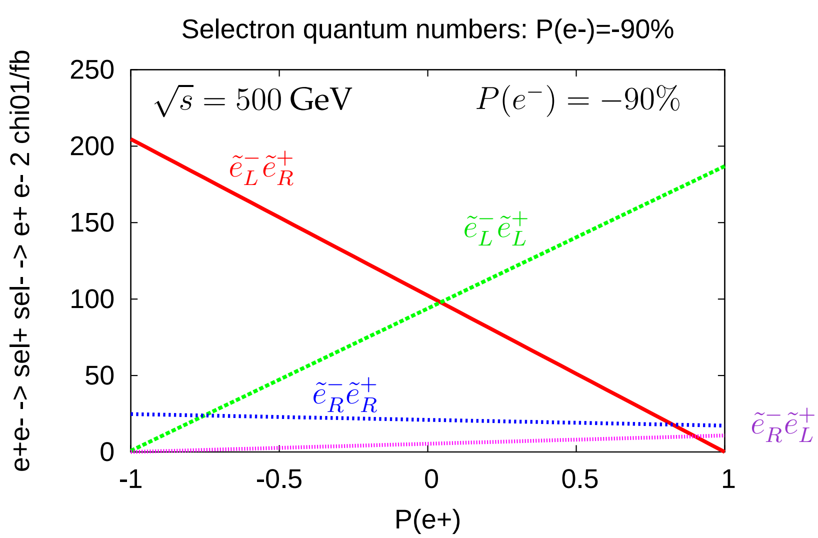

Figure 2: Separation of the selectron pair $\tilde{e}_L^- \tilde{e}_R^+$ in $e^+e^- \rightarrow \tilde{e}^+_{L,R}\tilde{e}^-_{L,R} \rightarrow e^+e^-2c\tilde{hi}_1^0$ with both beams polarized in order to test the association of chiral lepton quantum numbers to the scalar fermions in Susy transformations. In addition all SM background is strongly supressed.

2.2 Suppression of SM Background in new physics searches

2.2.1 Susy example: Smuon production

It is well known that beam polarisation is suitable to suppress SM background processe in new physics searches. E.g. W^+W^- presents one of the worst backgrounds, however, it can be easily suppressed with right-handed electron/left-handed positron beams. The scaling factors are listed in Table 2.1, [3].

It was already shown in sect. 2.1 that for the experimental proof of selectron chiral quantum numbers it is crucial to have both beam polarised.

In the case of $\tilde{\mu}^+\tilde{\mu}^-$ production we have only poduction via γ and Z^0 exchange, therefore only the beam configurations LR and RL are allowed. The predominant background for this signal is that due to W^+W^- process. In [51] an example is given for the reference point SPS3 [1], where the masses are given by

$$\tilde{\mu}_R = 178.3 \text{ GeV}, \quad \tilde{\mu}_L = 287.1 \text{ GeV}. \tag{1}$$

The cross sections are shown in Table 2.2 and one notes the considerable reduction in the production cross section fort right-handed electrons and left-handed positrons. In Fig. 3 the expected muon energy distributions for an integrated luminosity of 500 fb^{-1} at $\sqrt{s} = 750$ GeV are shown. On the left (right) side the spectrum for $P_{e^-} = -80\%$ (+80%), $P_{e^+} = +80$ (-80%)% is given. The background from W^+W^- decaying into $\mu\nu$ final state is included. This shows the importance of positron polarisation for a clear observation of the low energy edge of the $\tilde{mu}_L$, which cannot be clearly seen when the positron is unpolarised.

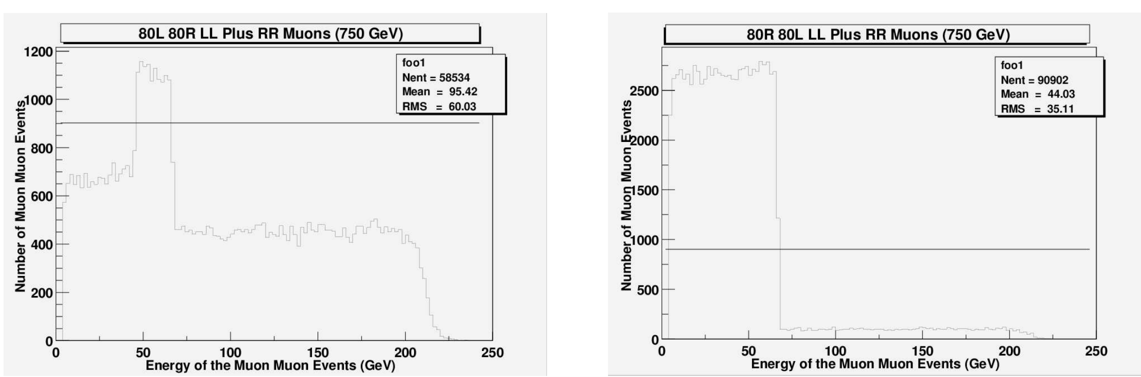

Figure 3: The muons energy spectrum from smuon decays including the properly normalized background from W^+W^- production when they decay into a $\mu\nu$ final state. On the left we show the case where the positron is 80% polarized right handed and the electrons is 80% polarized ledt handed. On the right we show the case in which the positron is 80% polarized left handed and the electron is 80% polarized right handed. These plots are for $\sqrt{s} = 750$ GeV [51].

Beam polarisation	$e^+e^- \to W^+W^-$	$e^+e^- \to ZZ$
$P_{e^-} = +80\%$, unpol. e^+	0.20	0.76
$P_{e^-} = -80\%$, unpol. e^+	1.80	1.25
$P_{e^-} = +80\%$, $P_{e^+} = -60\%$	0.10	1.05
$P_{e^-} = -80\%$, $P_{e^+} = +60\%$	2.85	1.91

Table 2.1: Scaling factors, i.e. ratios of polarised and unpolarised cross section $\sigma^{pol}/\sigma^{unpol}$, for WW and ZZ production.

Polarisation	$\sigma(\tilde{\mu}_R^+\tilde{\mu}_R^-)$/fb	$\sigma(\tilde{\mu}_L^+\tilde{\mu}_L^-)$/fb	$\sigma(W^+W^-)$/fb
$P_{e^-} = -80\%$, $P_{e^+} = -80\%$	11.44	5.06	1448.
$P_{e^-} = -80\%$, $P_{e^+} = +80\%$	21.23	37.74	12995.
$P_{e^-} = +80\%$, $P_{e^+} = -80\%$	82.99	8.37	198
$P_{e^-} = +80\%$, $P_{e^+} = +80\%$	11.44	5.06	1448
$P_{e^-} = -80\%$, e^+ unpol.	16.34	21.40	7241
$P_{e^-} = +80\%$, e^+ unpol.	47.21	6.72	824

Table 2.2: The cross sections for $e^+e^- \to \tilde{\mu}^+\tilde{\mu}^-$ in fb. Beamstrahlung is neglected in these studu [51]. One observes a large reduction of the W^+W^- cross section when the electron is right handed and the positron is left handed. It helps significantly in observing $\tilde{\mu}_L$.

δ	M_D ($P_{e^-,e^+}=0$)	M_D ($P_{e^-}=80\%$)	M_D ($P_{e^-}=80\%$, $P_{e^+}=-60\%$	M_D@LHC
2	4.48	6.27	7.86	4-7.5
3	3.54	4.63	5.55	4.5-5.9
4	2.91	3.64	4.23	5.0-5.3

Table 2.3: Discovery (5σ) reach in mass scale M_D in TeV for direct graviton production in the process $e^+e^- \to \gamma G$ at the LC for various numbers of extra dimensions δ [52]; the major background is $e^+e^- \to \nu\bar{\nu}\gamma$ which can be efficiently suppressed with beam polarisation. In the right column the discovery reach for M_D at the LhC is given for the process $pp \to$jet+G with 100 fb^{-1} [53].

2.2.2 Large extra dimensions example: graviton production

The signature for direct graviton production in $e^+e^- \to \gamma G$is a relatively soft photon and missing energy. The major background is $e^+e^- \to \gamma\nu\bar{\nu}$ and is largely irreducible. The study [52] is done for an integrated luminosity of 1000 fb^{-1} and 800 GeV with polarised beams. The background process shows nearly maximal asymmetry, therefore polarised beams are extremely effective in suppressing the background since ν couples only left-handed.

After applying effective cuts and background simulations the reach for the Mass scale M_D of extra dimensions is given Table. 2.3. It is obvious that polarising both beams to a high degree maximises the LC potential for exploring this physics. For regions wich can be compared at te LC and the LHC, the discovery reach in M_D is similar for both machines. However, the LC offers a more model-independent test of the theory.

If extra dimensions are the cause of anomalous single photon rate, the $\sqrt{s}$ dependence of the cross section should follow $\sigma \sim s^{\delta/2}$. Measuring excess cross sections with polarised beams at two different energies, e.g. $\sqrt{s} = 500$ GeV and 800 GeV allows to determine the number of extra dimensions with rather high accuracy [52]. This can be seen from Fig. 4, where the cross section for $e^+e^- \to \gamma G$ as a function of the scale M_D for different numbers δ of extra dimensions is shown. Obviously the reduction of the background process via the use of polarised beams, in particular both beams polarised, may be crucial for the determination of the numbers of extra dimensions.

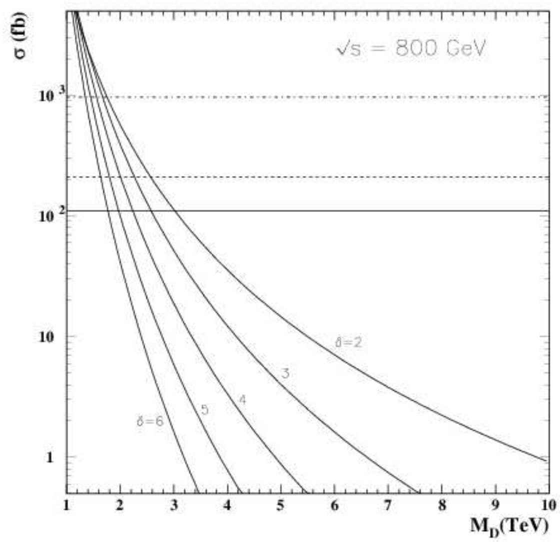

Figure 4: Total cross sections for $e^+e^- \to \gamma G$ at $\sqrt{s} = 800$ GeV as a function of the scale M_D for different numbers δ of extra dimensions. The cross section takes into account 80% electron and 60% positron polarisation. The three horizontal lines indicate the background cross sections from $e^+e^- \to \nu\bar{\nu}\gamma$ for both beams polarised (solid), only electron beam polarisation (dashed) and no polarisation (dot-dashed). The signal cross sections are reduced by a factor of 1.48 for the latter two scenarios [52].

2.3 Search for Supersymmetry

2.3.1 Determination of sfermion parameters

In this section phenomenological studies on the production of third generation sfermions in e^+e^- annihilation at $\sqrt{s} = 500$ GeV are summarised [48]. We take into account the effects of both e^- and e^+ beam polarizations. The main advantages of using polarized beams are: (i) larger cross sections can be obtained, (ii) background reactions can be suppressed, (iii) measurements of appropriate observables lead to additional information on the SUSY parameters. All calculations are performed within the Minimal Supersymmetric Standard Model (MSSM) with real parameters.

Sfermion Production

In the third generation, Yukawa terms give rise to mixing between the 'left' and 'right' states $\tilde{f}_L$ and $\tilde{f}_R$ ($\tilde{f} = \tilde{t}, \tilde{b}, \tilde{\tau}$). Neglecting the mixing between generations this mixing is described by a hermitian 2×2 mass matrix which depends on the soft SUSY–breaking mass parameters $M_{\tilde{Q}}$, $M_{\tilde{U}}$ etc., and the trilinear scalar coupling parameters A_t, A_b, A_τ. The mass eigenstates are $\tilde{f}_1 = \tilde{f}_L \cos\theta_{\tilde{f}} + \tilde{f}_R \sin\theta_{\tilde{f}}$, and $\tilde{f}_2 = \tilde{f}_R \cos\theta_{\tilde{f}} - \tilde{f}_L \sin\theta_{\tilde{f}}$, with $\theta_{\tilde{f}}$ the sfermion mixing angle.

Information on the sfermion mixing angle can be obtained from measuring production cross sections using different combinations of beam polarizations. It has be shown in [47–49] that beam polarisation may be crucial to resolve ambiguities, see as an example Fig. 5, where for the unpolarised case still two mixing angles $\cos 2\theta_{\tilde{\tau}}$ were consistent with the measured cross sections (red lines). However, using polarised beams projects out a single solution (green and blue line). In that case the simultaneous polarisation of both beams is interesting for enhancing the P_{eff}, enhancing the signal and reducing systematics which might be quite decisive for τ analyses [47].

In the following we discuss in detail the production of light stops. The reaction $e^+e^- \to \tilde{f}_i\bar{\tilde{f}}_j$ proceeds via γ and Z exchange in the s–channel. The $\tilde{f}_i$ couplings depend on the sfermion mixing angle $\theta_{\tilde{f}}$. In Figs. 6 a, b we show contour lines of the cross section $\sigma(e^+e^- \to \tilde{t}_1\bar{\tilde{t}}_1)$ as a function of the e^- and e^+ beam polarizations $\mathcal{P}_-$ and $\mathcal{P}_+$ at $\sqrt{s} = 500$ GeV for $m_{\tilde{t}_1} = 200$ GeV and (a) $\cos\theta_{\tilde{t}} = 0.4$ and (b) $\cos\theta_{\tilde{t}} = 0.66$. We have included initial–state radiation (ISR) and SUSY–QCD corrections (for details see [48,49]). The white windows show the range of polarizations $|\mathcal{P}_-| < 0.9$ and $|\mathcal{P}_+| < 0.6$. As can be seen, one can significantly increase the cross section by using the highest possible e^- and e^+ polarization available. Moreover, beam polarization strengthens the $\cos\theta_{\tilde{t}}$ dependence and can thus be essential for determining the mixing angle. Corresponding cross sections for the production of sbottoms, staus and τ–sneutrinos are presented in [48].

Parameter Determination

We estimate the precision one may obtain for the parameters of the $\tilde{t}$ sector from cross section measurements using the parameter point $m_{\tilde{t}_1} = 200$ GeV, $\cos\theta_{\tilde{t}} = -0.66$ as an illustrative example: For $\mathcal{P}_- = -0.9$ we find $\sigma_L(\tilde{t}_1\bar{\tilde{t}}_1) = 44.88$ fb and for $\mathcal{P}_- = 0.9$

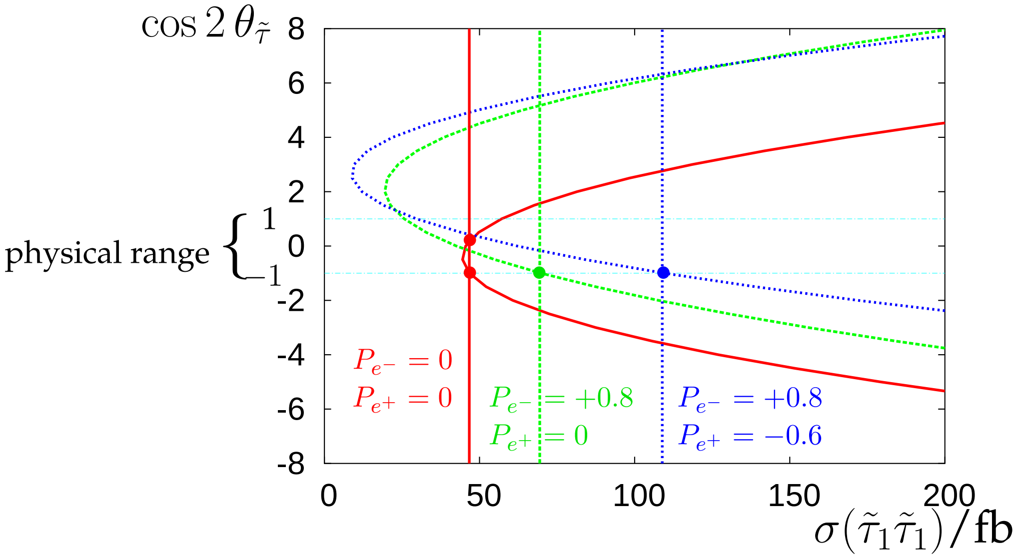

Figure 5: Mixing angle $\cos 2\theta_{\tilde\tau}$ versus cross section $\sigma(e^+e^- \to \tilde\tau_1\tilde\tau_1)$ at $\sqrt{s} = 500$ GeV for beam polarisations $P_{e^-} = +0.8$ and unpolarised positrons (green), $P_{e^-} = +0.8$ and $P_{e^+} = -0.6$ (blue) and the unpolarised case (red) in the scenario RP. The vertical lines indicate the predicted cross sections. For unpolarised beams one observes a two-fold ambiguity in $\cos 2\theta_{\tilde\tau}$ (red dots); for polarised beams, however, only one solution lies in the allowed range (green and blue dot) [47].

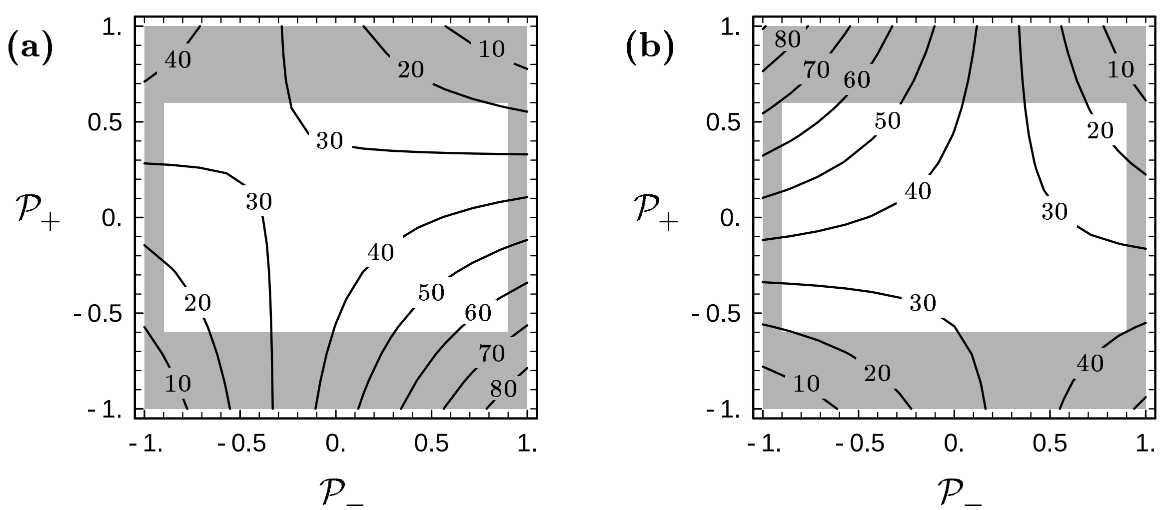

Figure 6: Dependence of $\sigma(e^+e^- \to \tilde t_1 \bar{\tilde t}_1)$ on degree of electron and positron polarization at $\sqrt{s} = 500$ GeV, for $m_{\tilde t_1} = 200$ GeV, $\cos\theta_{\tilde t} = 0.4$ in (a) and $\cos\theta_{\tilde t} = 0.66$ in (b).

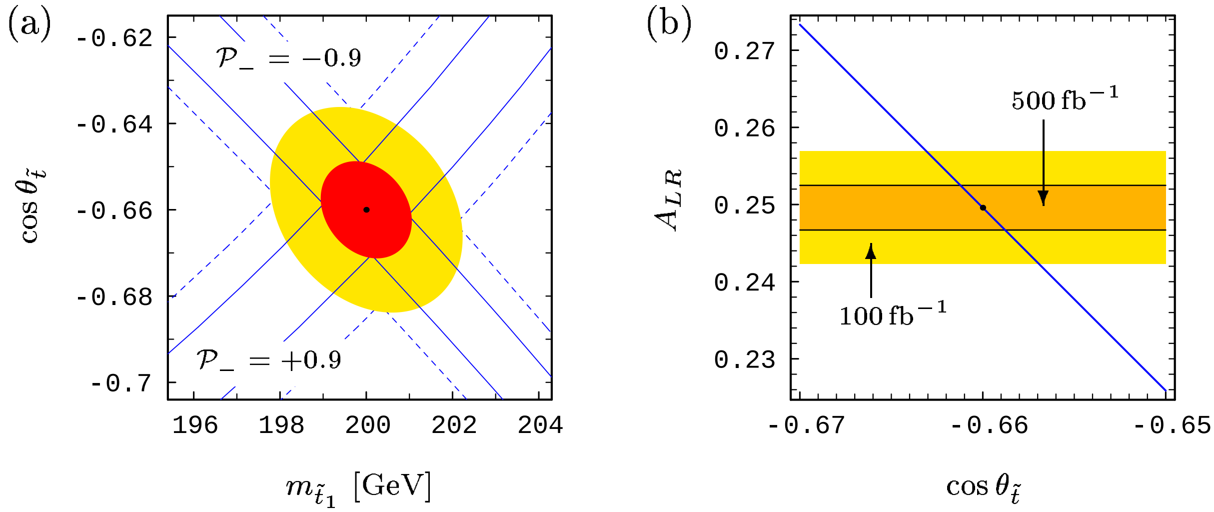

Figure 7: (a) Error bands and 68% CL error ellipse for determining $m_{\tilde{t}_1}$ and $\cos\theta_{\tilde{t}}$ from cross section measurements; the dashed lines are for $\mathcal{L} = 100$ fb^{-1} and the full lines for $\mathcal{L} = 500$ fb^{-1}. (b) Error bands for the determination of $\cos\theta_{\tilde{t}}$ from A_{LR}. In both plots $m_{\tilde{t}_1} = 200$ GeV, $\cos\theta_{\tilde{t}} = -0.66$, $\sqrt{s} = 500$ GeV, $\mathcal{P}_- = \pm 0.9$, $\mathcal{P}_+ = 0$.

$\sigma_R(\tilde{t}_1\bar{\tilde{t}}_1) = 26.95$ fb (with $\mathcal{P}_+ = 0$) including SUSY–QCD, Yukawa coupling, and ISR corrections. According to the Monte Carlo study of [50] one can expect to measure the $\tilde{t}_1\bar{\tilde{t}}_1$ production cross sections with a statistical error of $\Delta\sigma_L/\sigma_L = 2.1\,\%$ and $\Delta\sigma_R/\sigma_R = 2.8\,\%$ in case of an integrated luminosity of $\mathcal{L} = 500$ fb^{-1} (i.e. $\mathcal{L} = 250$ fb^{-1} for each polarization). Scaling these values to $\mathcal{L} = 100$ fb^{-1} leads to $\Delta\sigma_L/\sigma_L = 4.7\,\%$ and $\Delta\sigma_R/\sigma_R = 6.3\,\%$. Figure 7 a shows the corresponding error bands and error ellipses in the $m_{\tilde{t}_1}-\cos\theta_{\tilde{t}}$ plane. The resulting errors on the stop mass and mixing angle are: $\Delta m_{\tilde{t}_1} = 2.2$ GeV, $\Delta\cos\theta_{\tilde{t}} = 0.02$ ($\Delta m_{\tilde{t}_1} = 1.1$ GeV, $\Delta\cos\theta_{\tilde{t}} = 0.01$) for $\mathcal{L} = 100$ fb^{-1} ($\mathcal{L} = 500$ fb^{-1}). If in addition the e^+ beam is 60% polarized these values can be improved by $\sim 25\%$.

For the determination of the mixing angle, one can also make use of the left–right asymmetry $A_{LR} \equiv [\sigma(-|\mathcal{P}_-|, |\mathcal{P}_+|) - \sigma(|\mathcal{P}_-|, -|\mathcal{P}_+|)]/[\sigma(-|\mathcal{P}_-|, |\mathcal{P}_+|) + \sigma(|\mathcal{P}_-|, -|\mathcal{P}_+|)]$. We get $A_{LR}(e^+e^- \to \tilde{t}_1\bar{\tilde{t}}_1) = 0.2496$ for $m_{\tilde{t}_1} = 200$ GeV, $\cos\theta_{\tilde{t}} = -0.66$, $\sqrt{s} = 500$ GeV, $\mathcal{P}_- = 0.9$, and $\mathcal{P}_+ = 0$. Taking into account experimental errors as determined in [50], a theoretical uncertainty of 1%, and $\Delta P/P = 10^{-2}$ we get $\Delta A_{LR} = 2.92\%$ (1.16%) for $\mathcal{L} = 100\,\text{fb}^{-1}$ ($500\,\text{fb}^{-1}$). This corresponds to $\Delta\cos\theta_{\tilde{t}} = 0.0031$ (0.0012). This is most likely the most precise method to determine the stop mixing angle. The corresponding error bands are shown in Fig. 7 b.

2.3.2 Polarisation effects in the gaugino/higgsino sector

still under work

2.3.3 CP asymmetries in neutralino production and decay

Particularly interesting in supersymmetry is the study of new additional CP violating sources. In the following we show a suitable observable for verifying CP violation in the gaugino/higgsino sector.

In the neutralino sector of the Minimal Supersymmetric Standard Model (MSSM) [33], the gaugino mass parameter M_1, the higgsino mass parameter μ, and the trilinear coupling parameter A_τ in the stau sector, can be complex. The physical phases φ_{M_1}, φ_μ and φ_{A_τ} of these parameters can cause large CP-violating effects already at tree level. In the following we focus on the effects of a complex $U(1)$ gaugino mass parameter M_1 and higgsino mass parameter μ in neutralino production and decay.

In neutralino production

$$e^- + e^+ \quad\rightarrow\quad \tilde{\chi}^0_i + \tilde{\chi}^0_j \tag{2}$$

and the subsequent leptonic two-body decays

$$\tilde{\chi}^0_i \quad\rightarrow\quad \tilde{\ell} + \ell_1, \quad \text{and} \quad \tilde{\ell} \rightarrow \tilde{\chi}^0_1 + \ell_2; \quad \ell_{1,2} = e, \mu, \tau, \tag{3}$$

as well as the subsequent leptonic three-body decays

$$\tilde{\chi}^0_2 \longrightarrow \tilde{\chi}^0_1 + l^- + l^+, \quad \text{where} \quad l = e, \mu, \tag{4}$$

the neutralino spin correlations lead to several CP-odd asymmetries.

With the triple product $\mathcal{T} = (\vec{p}_{e^-} \times \vec{p}_{\ell_2}) \cdot \vec{p}_{\ell_1}$, we define the *T-odd* asymmetry of the cross section σ for the processes (2)-(4):

$$\mathcal{A}_{\rm T} = \frac{\sigma(\mathcal{T} > 0) - \sigma(\mathcal{T} < 0)}{\sigma(\mathcal{T} > 0) + \sigma(\mathcal{T} < 0)}. \tag{5}$$

If absorbtive phases are neglected, $\mathcal{A}_{\rm T}$ is CP-odd due to CPT invariance. The dependence of $\mathcal{A}_{\rm T}$ on φ_{M_1} and φ_μ was analyzed in [35–37].

In case the neutralino decays into a τ-lepton, $\tilde{\chi}^0_i \rightarrow \tilde{\tau}^\pm_k \tau^\mp$, $k = 1, 2$, the T-odd transverse τ^- and τ^+ polarizations P_2 and $\bar{P}_2$, respectively, give rise to the *CP-odd* observable

$$\mathcal{A}_{\rm CP} = \frac{1}{2}(P_2 - \bar{P}_2), \tag{6}$$

which is also sensitive to φ_{A_τ}. For various MSSM scenarios, $\mathcal{A}_{\rm CP}$ was discussed in [38]. For measuring the asymmetries, it is crucial to have both large asymmetries and large cross sections. In this note we study the impact of longitudinally polarized e^+ and e^- beams of a future linear collider in the 500 GeV range on the asymmetries $\mathcal{A}_{\rm T}$, $\mathcal{A}_{\rm CP}$ and on the cross sections σ.

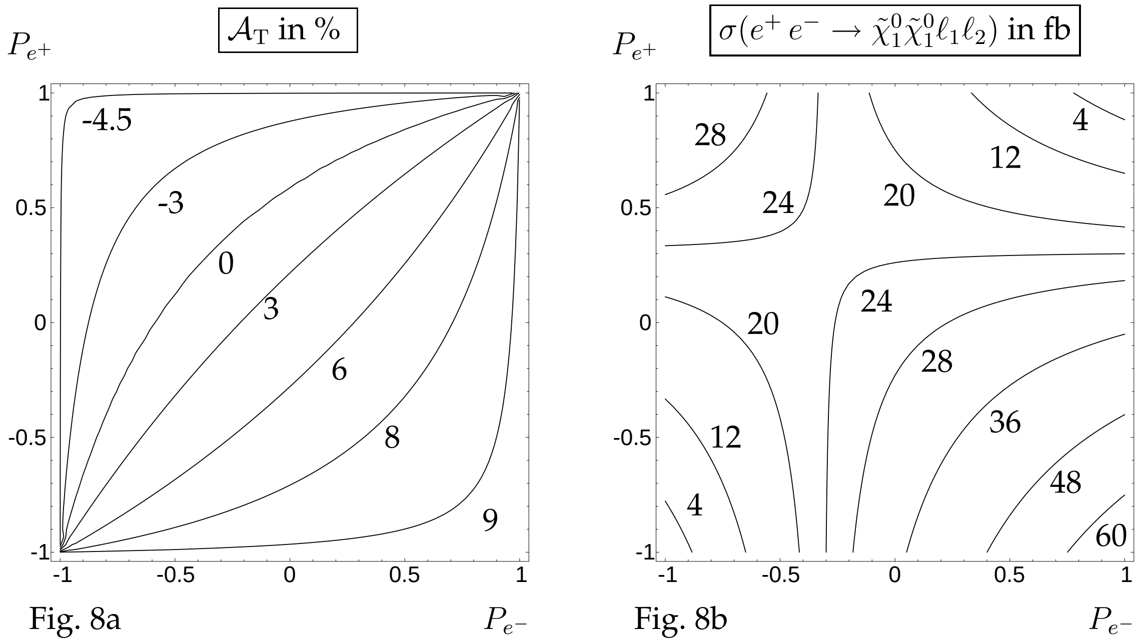

Fig. 8a

Fig. 8b

Figure 8: Contour lines of $\mathcal{A}_{\rm T}$ and σ for $\varphi_{M_1} = 0.2\pi$, $\varphi_\mu = 0$, $|\mu| = 240$ GeV, $M_2 = 400$ GeV, $\tan\beta = 10$ and $m_0 = 100$ GeV.

Numerical results for the two-body decay

We present numerical results for $e^+e^- \to \tilde{\chi}^0_1\tilde{\chi}^0_2$ with the subsequent leptonic decay of $\tilde{\chi}^0_2$ for a linear collider with $\sqrt{s} = 500$ GeV. For $\mathcal{A}_{\rm T}$, Eq. (5), we study the neutralino decay into the right selectron and right smuon, $\tilde{\chi}^0_2 \to \tilde{\ell}_R \ell_1$, $\ell = e, \mu$ and for $\mathcal{A}_{\rm CP}$, Eq. (6), that into the lightest scalar tau, $\tilde{\chi}^0_2 \to \tilde{\tau}_1 \tau$. We study the dependence of the asymmetries and the cross sections on the beam polarizations P_{e^-} and P_{e^+} for fixed parameters $\mu = |\mu|\, e^{i\varphi_\mu}$, $M_1 = |M_1|\, e^{i\varphi_{M_1}}$, $A_\tau = |A_\tau|\, e^{i\varphi_{A_\tau}}$, M_2 and $\tan\beta$. We assume $|M_1| = 5/3 M_2 \tan^2\theta_W$ and use the renormalization group equations [39] for the selectron and smuon masses, $m^2_{\tilde{\ell}_R} = m_0^2 + 0.23 M_2^2 - m_Z^2 \cos 2\beta \sin^2\theta_W$ with $m_0 = 100$ GeV. The interaction Lagrangians and details on stau mixing can be found in [37].

In Fig. 8a we show the dependence of $\mathcal{A}_{\rm T}$ on the beam polarization for $\varphi_{M_1} = 0.2\,\pi$ and $\varphi_{A_\tau} = \varphi_\mu = 0$. A small value of φ_μ is suggested by constraints on electron and neutron electric dipole moments (EDMs) [40] for a typical SUSY scale of the order of a few 100 GeV. It is remarkable that in our scenario the asymmetry can be close to 10% even for the small value of $\varphi_{M_1} = 0.2\,\pi$ and for $\varphi_\mu = 0$. The cross section $\sigma = \sigma(e^+e^- \to \tilde{\chi}^0_1\tilde{\chi}^0_2) \times {\rm BR}(\tilde{\chi}^0_2 \to \tilde{\ell}_R \ell_1) \times {\rm BR}(\tilde{\ell}_R \to \tilde{\chi}^0_1 \ell_2)$ is shown in Fig. 8b. For our scenario with $|A_\tau| = 250$ GeV and $\varphi_{A_\tau} = 0$, the neutralino branching ratio is BR($\tilde{\chi}^0_2 \to \tilde{\ell}_R \ell_1$) = 0.63 (summed over both signs of charge) and BR($\tilde{\ell}_R \to \tilde{\chi}^0_1 \ell_2$) = 1. Note that the asymmetry $\mathcal{A}_{\rm T}$ and the cross section σ are both considerably enhanced for negative positron and positive electron beam polarization. This choice of polarization enhances the contributions of the right slepton exchange in the neutralino production, Eq. (2), and reduces that of left slepton exchange [41,42]. While the contributions of right and left slepton exchange enter σ with the same sign, they enter $\mathcal{A}_{\rm T}$ with opposite sign, which accounts for the sign change of $\mathcal{A}_{\rm T}$.

In Fig. 9a we show the contour lines of the τ polarization asymmetry $\mathcal{A}_{\rm CP}$, Eq. (6), for

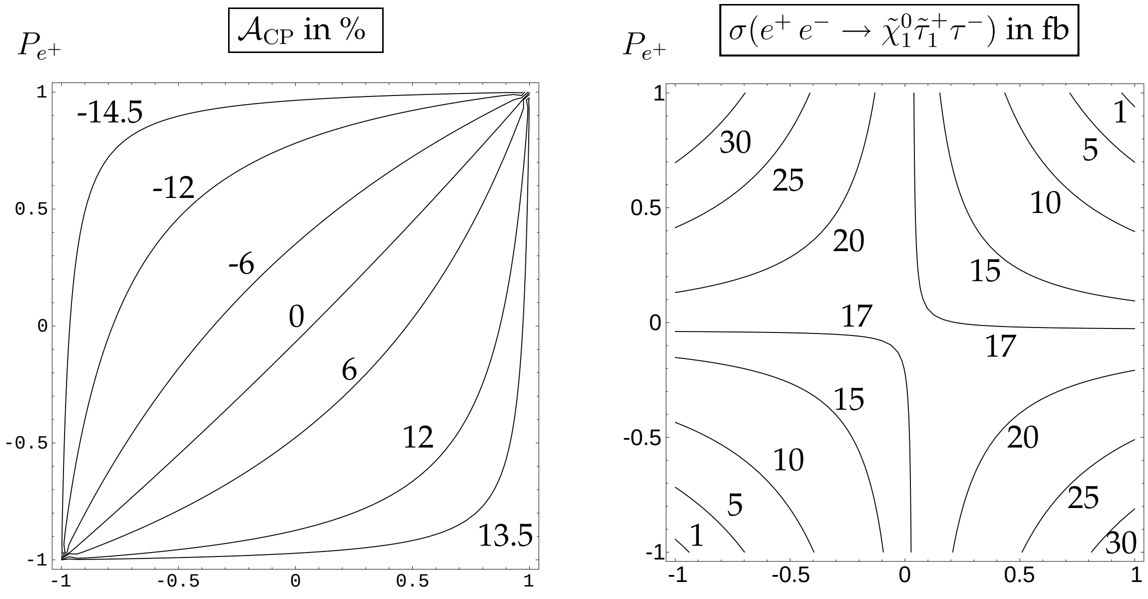

Fig. 9a Fig. 9b

Figure 9: Contour lines of $\mathcal{A}_{\rm CP}$ and σ for $\varphi_{A_\tau} = 0.5\pi$, $|A_\tau| = 1500$ GeV, $\varphi_{M_1} = \varphi_\mu = 0$, $|\mu| = 250$ GeV, $M_2 = 200$ GeV, $\tan\beta = 5$ and $m_0 = 100$ GeV.

$\varphi_{A_\tau} = 0.5\pi$ and $\varphi_{M_1} = \varphi_\mu = 0$ in the P_{e^-}-P_{e^+} plane. We have chosen a large value of $|A_\tau| = 1500$ GeV because $\mathcal{A}_{\rm CP}$ increases with increasing $|A_\tau| \gg |\mu|\tan\beta$ [38]. For unpolarized beams the asymmetry is 1%. However, it reaches values of more than $\pm 13\%$ if the e^+ and e^- beams are polarized with the opposite sign. If at least one of the beams is polarized (e.g. $P_{e^-} = 0.8$, $P_{e^+} = 0.6$), the asymmetries are somewhat smaller ($\sim 10\%$). The reason for this dependence is again the enhancement of either the right or the left selectron exchange contributions in the production process. The cross section $\sigma = \sigma(e^+e^- \to \tilde{\chi}^0_1\tilde{\chi}^0_2) \times {\rm BR}(\tilde{\chi}^0_2 \to \tilde{\tau}^+_1\tau^-)$ is shown in Fig. 9b with ${\rm BR}(\tilde{\chi}^0_2 \to \tilde{\tau}^+_1\tau^-) = 0.22$. Also σ is very sensitive to variations of the beam polarization and varies between 1 fb and 30 fb.

Since the asymmetry $\mathcal{A}_{\rm CP}$ is also very sensitive to the phases φ_{M_1} and φ_μ we show for $\varphi_{M_1} = 0.2\pi$ and $\varphi_\mu = \varphi_{A_\tau} = 0$, the dependence of $\mathcal{A}_{\rm CP}$ and $\sigma = \sigma(e^+e^- \to \tilde{\chi}^0_1\tilde{\chi}^0_2) \times {\rm BR}(\tilde{\chi}^0_2 \to \tilde{\tau}^+_1\tau^-)$ on the beam polarization in Figs. 10a, b, respectively. The neutralino branching ratio is ${\rm BR}(\tilde{\chi}^0_2 \to \tilde{\tau}^+_1\tau^-) = 0.19$ for our scenario. Despite the small phases, $\mathcal{A}_{\rm CP}$ reaches values up to -12% for negative e^- and positive e^+ beam polarizations.

Analytical and numerical results for the three-body decay

The amplitude squared of the combined processes of production, eq. (2), and decay, eq. (4), can be written as

$$|T|^2 = PD + \Sigma^a_P \Sigma^a_D, \tag{7}$$

where P and D describe production and decay without spin correlation and Σ^a_P and Σ^a_D ($a = 1, 2, 3$) are the terms with spin correlation [45]. In Σ^a_P and Σ^a_D products like $i\epsilon_{\mu\nu\rho\sigma}p^\mu_i p^\nu_j p^\rho_k p^\sigma_l$ appear. This leads to CP-violating effects already at tree level.

We introduce the triple product $\vec{p}_{l^+}(\vec{p}_{e^-} \times \vec{p}_{l^-})$, where $\vec{p}_{e^-}, \vec{p}_{l^-}$ and $\vec{p}_{l^+}$ are the momenta of initial e^- beam and the two final leptons l^- and l^+, respectively. We define a CP asym-

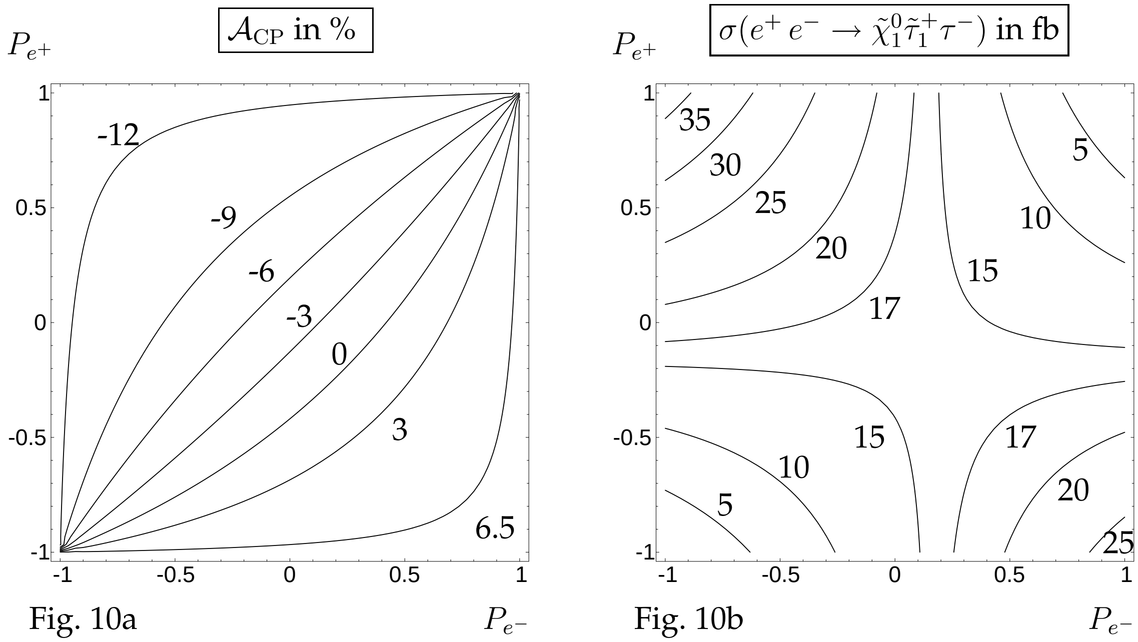

Figure 10: Contour lines of $\mathcal{A}_{\rm CP}$ and σ for $\varphi_{M_1} = 0.2\pi$, $\varphi_\mu = 0$, $|\mu| = 250$ GeV, $M_2 = 200$ GeV, $\varphi_{A_\tau} = 0$, $|A_\tau| = 250$ GeV, $\tan\beta = 5$ and $m_0 = 100$ GeV.

	$\lvert M_1\rvert$	M_2	$\lvert\mu\rvert$	$\tan\beta$	$m_{\tilde{e}_L}$	$m_{\tilde{e}_R}$	$m_{\tilde{\chi}^0_1}$	$m_{\tilde{\chi}^0_2}$
A	99.1	192.7	352.4	10	267.6	224.4	97.4	176.3
B	100.1	210	250	5	277.4	227.7	96	166.7

Table 2.4: Parameters $|M_1|$, M_2, $|\mu|$, $\tan\beta$, $m_{\tilde{e}_L}$ and $m_{\tilde{e}_R}$ in the scenarios A and B and the corresponding masses of $m_{\tilde{\chi}^0_{1,2}}$. All masses are given in [GeV].

metry as

$$A_T = \frac{\int sign\{(\vec{p}_{l^+}(\vec{p}_{e^-} \times \vec{p}_{l^-})\}|T|^2 dlips}{\int |T|^2 dlips}, \tag{8}$$

assuming that final state interactions and finite-widths effects can be neglected. A_T is proportional to the difference of the number of events with the final lepton l^+ above and below the plane spanned by $\vec{p}_{e^-}$ and $\vec{p}_{l^-}$. The analogous asymmetry for neutralino two-body decays has been studied in [46].

We analyse numerically the influence of longitudinal beam polarization on the CP asymmetry A_T in the scenarios defined in Tab.1. Scenario A is inspired by the SPS1a scenario [29], whereas in scenario B the mixing between gaugino and higgsino components is larger. We fix the center of mass energy $\sqrt{s} = 500$ GeV and take the phases of the complex parameters $M_1 = |M_1|e^{i\phi_{M_1}}$ and $\mu = |\mu|e^{i\phi_\mu}$ as $\phi_{M_1} = \frac{\pi}{2}$ and $\phi_\mu = 0$. In Fig.11a and b we show the CP asymmetry A_T, eq.(8), as a function of the e^- beam polarization P_{e^-} for different e^+ beam polarizations P_{e^+}, in the ranges $-0.9 \le P_{e^-} \le +0.9$ and $-0.6 \le P_{e^+} \le +0.6$, for the scenarios A and B . In both scenarios the highest CP asymmetry is reached for $P_{e^-} = -0.9$ and $P_{e^+} = +0.6$. For these polarizations the $\tilde{e}_L$ contributions to the spin density matrix dominate. With opposite signs of the beam polarizations the $\tilde{e}_R$ contributions are dominating. For scenario A (Fig.11a) one gets a CP asymmetry of about

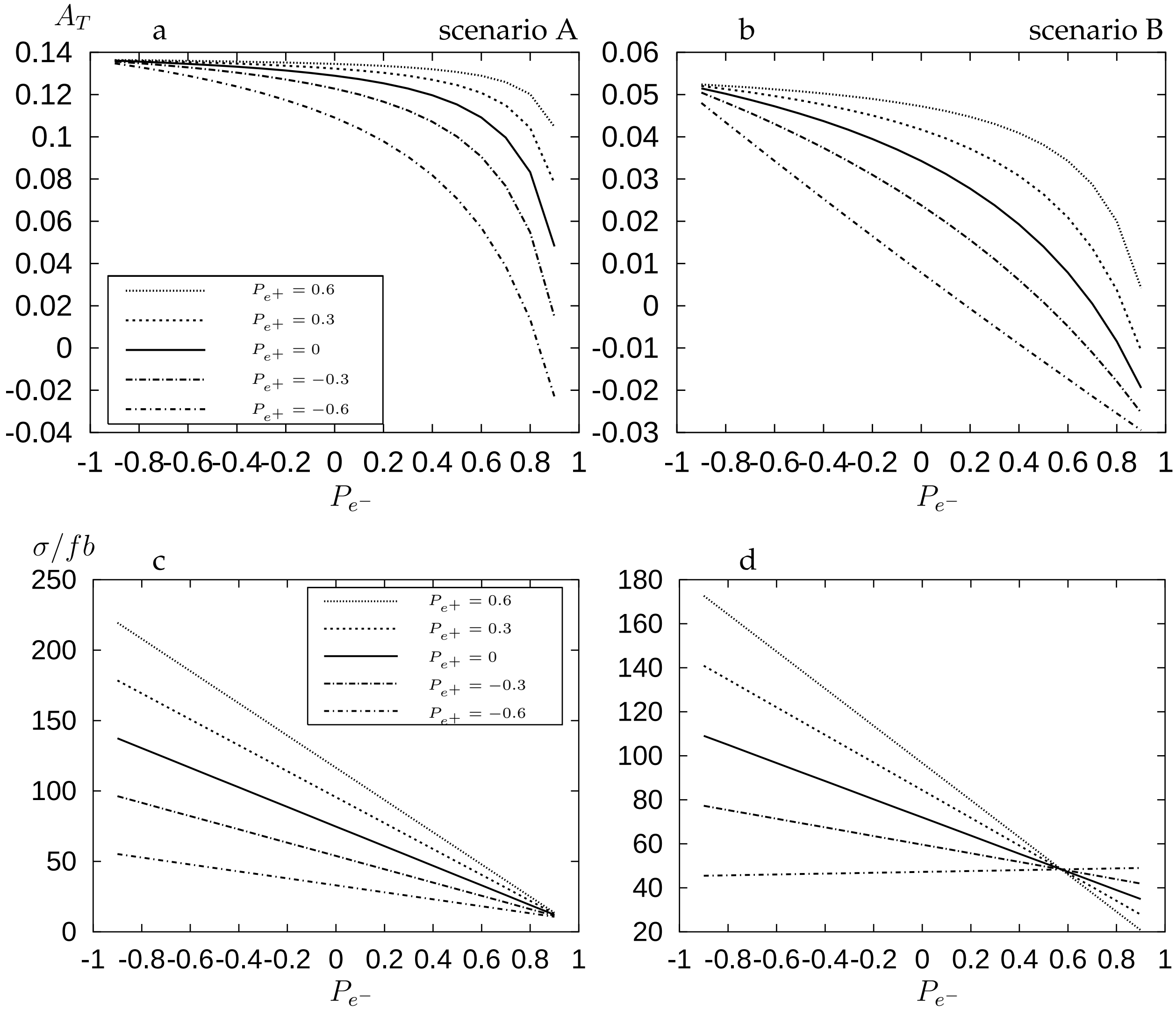

Figure 11: a,b CP asymmetry A_T, eq.(4), for $e^+e^- \longrightarrow \tilde{\chi}^0_1\tilde{\chi}^0_2$ with subsequent leptonic three-body decay $\tilde{\chi}^0_2 \to \tilde{\chi}^0_1 l^+ l^-$, and c,d production cross section $\sigma(e^+e^- \longrightarrow \tilde{\chi}^0_1\tilde{\chi}^0_2)$, as a function of the e^- beam polarization P_{e^-} for different e^+ beam polarizations P_{e^+}, for $\sqrt{s} = 500$ GeV, $\phi_{M_1} = \frac{\pi}{2}$ and $\phi_\mu = 0$ for the scenarios A and B defined in Tab.1.

$14\%(-2\%)$ for the polarizations $P_{e^-} = -0.9(+0.9)$ and $P_{e^+} = +0.6(-0.6)$. In scenario B (Fig.11b) the CP asymmetry is about 3% in the unpolarized case whereas it is $5\%(-3\%)$ with polarizations $P_{e^-} = -0.9(+0.9)$ and $P_{e^+} = +0.6(-0.6)$. Fig.11c and d show the corresponding production cross sections σ as a function of the beam polarizations for the same parameters as in Fig.11a and b. In scenario A(B) the cross section and hence the expected rate necessary to measure A_T is enhanced by e^- beam polarization $P_{e^-} = -0.9$ by a factor $1.8(1.6)$ compared to the unpolarized case. In addition, a polarized e^+ beam with $P_{e^+} = +0.6$ would further enhance the cross section by a factor $1.5(1.6)$.

Summary and conclusion

Within the MSSM we have analyzed the dependence on the beam polarization of CP-odd asymmetries in $e^+e^- \to \tilde{\chi}^0_1\tilde{\chi}^0_2$ and the subsequent leptonic two-body decay and three-body decay of $\tilde{\chi}^0_2$. For the decay process $\tilde{\chi}^0_2 \to \tilde{\ell}_R \ell_1$, $\tilde{\ell}_R \to \tilde{\chi}^0_1 \ell_2$ with $\ell_{1,2} = e, \mu$, we have found that the asymmetry $\mathcal{A}_{\rm T}$ of the triple product $(\vec{p}_{e^-} \times \vec{p}_{\ell_2}) \cdot \vec{p}_{\ell_1}$, which is sensitive to φ_{M_1} and φ_μ, can be twice as large if polarized beams are used, with e.g. $P_{e^-} = 0.8$ and $P_{e^+} = -0.6$. Also for these polarizations the cross section can be enhanced up to a factor of 2. For the neutralino decay, $\tilde{\chi}^0_2 \to \tilde{\tau}^{\mp}_1 \tau^{\pm}$, we have given numerical examples for the beam polarization dependence of the CP-odd τ polarization asymmetry $\mathcal{A}_{\rm CP}$, which is also sensitive to φ_{A_τ}. Both $\mathcal{A}_{\rm CP}$ and the cross section depend sensitively on the beam polarizations and can be enhanced by a factor between 2 and 3. We have also analysed the dependence on longitudinal beam polarizations of the CP asymmetry A_T in neutralino production with subsequent leptonic three-body decay. We obtain the highest cross section and CP asymmetry with beam polarizations $P_{e^-} = -0.9$ and $P_{e^+} = +0.6$. Then in scenario A(B) the CP asymmetry is enhanced by a factor $1.1(1.5)$ and the cross section is enhanced by a factor $2.9(2.4)$ compared to the unpolarized case.

2.3.4 Polarisation Effects in extended MSSM models

Production of Singlino-dominated Neutralinos

Nonminimal extensions of the Minimal Supersymmetric Standard Model (MSSM) are characterized by an additional singlet superfield with vacuum expectation value x. The singlino character of these singlino-dominated neutralinos crucially depend on the parameter x. In the Next-to-Minimal Supersymmetric Standard Model (NMSSM) [19–22] or an E_6 inspired model with one extra neutral gauge boson Z' and one additional singlet superfield [23] neutralinos with a dominant singlet higgsino (singlino) component exist for large values $x \gtrsim 1$ TeV. Beam polarisation may be crucial either for a) observing singlino dominated neutralino poduction and b) for distinguishing between the MSSM and the extended model.

a) Production of singlino-dominated neutralinos

Since the singlino component does not couple to gauge bosons, gauginos, (scalar) leptons and (scalar) quarks, cross sections for the production of the exotic neutralinos are generally small [24–27]. However, they may be produced at a high luminosity e^+e^- linear collider with cross sections sufficient for detection, which can even be enhanced by the use of one or both beams polarized. We analyze the regions of x where the associated production of the singlino-dominated neutralino yields detectable cross sections for different beam polarisations in scenarios where the MSSM-like neutralinos have similar masses and mixing character as in the 'typical mSUGRA' SPS 1a scenario for the MSSM [28,29].

In the NMSSM the parameters (for details see [19]) $M_1 = 99$ GeV, $M_2 = 193$ GeV, $\tan\beta = 10$, the effective μ parameter $\mu_{\mathrm{eff}} = \lambda x = 352$ GeV and the selectron masses $m_{\tilde{e}_R} = 143$ GeV and $m_{\tilde{e}_L} = 202$ GeV are chosen according to the scenario SPS 1a. For large $x \gg |M_2|$ a singlino-dominated neutralino $\tilde{\chi}^0_S$ with mass $\approx 2\kappa x$ in zeroth approximation decouples in the neutralino mixing matrix while the other four neutralinos $\tilde{\chi}^0_{1,\ldots,4}$ have MSSM character as in SPS 1a with masses 96 GeV, 177 GeV, 359 GeV and 378 GeV.

Further we consider an E_6 inspired model with one extra neutral gauge boson Z' and one additional singlet superfield which contains six neutralinos [23]. Again the MSSM parameters and masses of the MSSM-like neutralinos are fixed according to the scenario SPS 1a, while a nearly pure light singlino-like neutralino $\tilde{\chi}^0_S$ with mass $\approx 0.18\, x^2/|M'|$ in zeroth approximation exists for very large values $|M'| \gg x$ [30]. The sign of M' is fixed by requiring relative sign $+1$ between the mass eigenvalues of $\tilde{\chi}^0_S$ and $\tilde{\chi}^0_1$ [24].

In Fig. 12 we show the associated production of the singlino-dominated $\tilde{\chi}^0_S$ together with the lightest MSSM-like neutralino $\tilde{\chi}^0_1$ for unpolarized beams and beam polarizations $P_- = +0.8$, $P_+ = 0$ and $P_- = +0.8$, $P_+ = -0.6$ for two masses 70 and 120 GeV of $\tilde{\chi}^0_S$, where the singlino-dominated neutralino is the LSP and NLSP, respectively. Electron beam polarisation $P_- = +0.8$ enhances the cross section by a factor 1.5 to 1.8, while additional positron beam polarisation $P_+ = -0.6$ gives a further enhancement factor of about 1.6. The cross sections are decreasing in good approximation as $1/x^2$ governed by the gaugino content of $\tilde{\chi}^0_S$ [24,25]. If we assume a cross section of 1 fb to be sufficient for discovery, the singlino-dominated neutralino can be detected with unpolarized beams for $x < 7.4$ TeV (9.7 TeV) in the NMSSM with $m_{\tilde{\chi}^0_S} = 70$ GeV (120 GeV) and for $x < 8.5$ TeV (6.4 TeV) in the E_6 model. For polarized electron beam the reach in x is enhanced to $x < 10.0$ TeV

x reach ($\sigma \geq 1fb$)	NMSSM $m_{\tilde{S}} = 70$ GeV	NMSSM $m_{\tilde{S}} = 120$ GeV	E6 $m_{\tilde{S}} = 70$ GeV	E6 $m_{\tilde{S}} = 120$ GeV
unpolarised beams	< 7.4 TeV	< 9.7 TeV	< 8.5 TeV	< 6.4 TeV
$P_{e^-} = +80\%$, unpol. e^+	< 10.0 TeV	< 12.3 TeV	< 11.4 TeV	< 7.9 TeV
$P_{e^-} = +80\%$, $P_{e^-} = -60\%$	< 12.6 TeV	< 15.5 TeV	< 14.4 TeV	< 10.0 TeV

Table 2.5: Range of accessible region of the singlet vacuum expectation value x under the discovery assumption of $\sigma(e^+e^- \to \tilde{S}\tilde{\chi}_i^0) \geq 1$ fb.

(12.3 TeV) in the NMSSM and $x < 11.4$ TeV (7.9 TeV) in the E_6 model, whereas for both beams polarized to $x < 12.6$ TeV (15.5 TeV) in the NMSSM and $x < 14.4$ TeV (10.0 TeV) in the E_6 model, see Table 2.5. Direct experimental evidence of a fifth neutralino would be an explicit proof for an extended SUSY model and is also crucial to apply sum rules in order to test the closure of the neutralino system [31].

b) Distinction between MSSM and NMSSM

Sitges/Paris example: under work

Conclusion

We have studied the production of singlino-dominated neutralinos in the NMSSM and an E_6 inspired model at a linear collider with polarized beams. With both beams polarized the cross sections are enhanced by a factor $2.4 - 2.9$ in comparison to unpolarized beams, depending on the scenario. This enhances the reach for the singlino-dominated neutralinos to singlet vevs as large as 15 TeV.

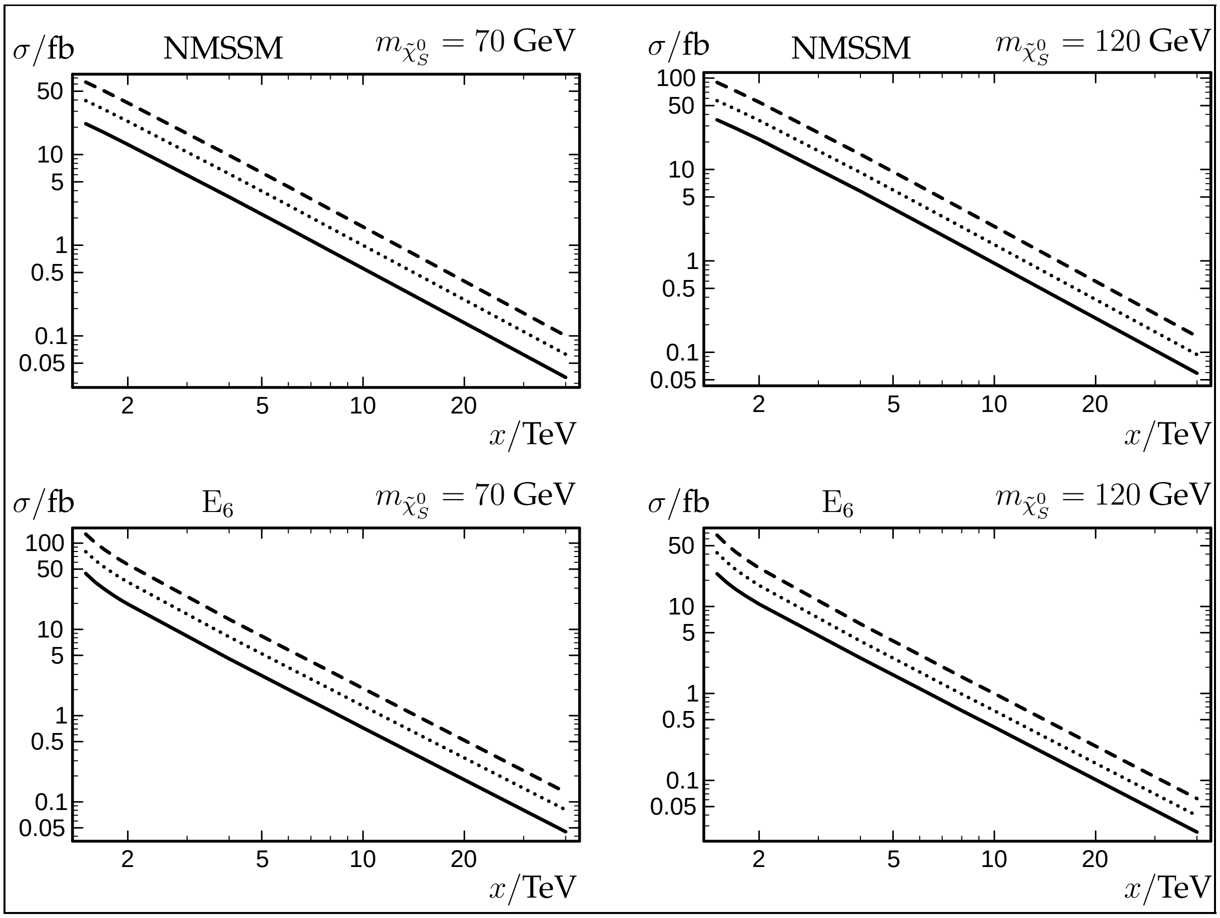

Figure 12: Cross sections for the production of a singlino-dominated neutralino $\tilde{\chi}^0_S$ via $e^+e^- \to \tilde{\chi}^0_S\tilde{\chi}^0_1$ for $\sqrt{s} = 500$ GeV in the SPS 1a inspired scenarios in the NMSSM and E_6 model with $M_1 = 99$ GeV, $M_2 = 193$ GeV, $\tan\beta = 10$ and $\mu_{\mathrm{eff}} = \lambda x = 352$ GeV with unpolarized beams (solid) and beam polarizations $P_- = +0.8$, $P_+ = 0$ (dotted) and $P_- = +0.8$, $P_+ = -0.6$ (dashed). The mass of $\tilde{\chi}^0_S$ is fixed at 70 GeV and 120 GeV by the parameters κ (NMSSM) and M' (E_6 model).

Figure 13: SUSY – Sneutrino production in R–parity violating model: Resonance production of $e^+e^- \to \tilde{\nu}$ interfering with Bhabha scattering for different configurations of beam polarization: unpolarized case (solid), $P_{e^-} = -80\%$ and $P_{e^+} = +60\%$ (hatched), $P_{e^-} = -80\%$ and $P_{e^+} = -60\%$ (dotted) [32].

2.3.5 Polarization effects in R–parity violating SUSY

In R–parity violating SUSY, processes can occur which prefer the extraordinary (LL) or (RR) polarization configurations. An interesting example is $e^+e^- \to \tilde{\nu} \to e^+e^-$. The main background to this process is Bhabha scattering. Polarizing both electrons and positrons can strongly enhance the signal. A study [32] was made for $m_{\tilde{\nu}} = 650$ GeV, $\Gamma_{\tilde{\nu}} = 1$ GeV, with an angle cut of $45^0 \leq \Theta \leq 135^0$ and a lepton–number violating coupling $\lambda_{131} = 0.05$ in the R–parity violating Langrangian $\mathcal{L}_{\not{R}} \sim \sum_{i,j,k} \lambda_{ijk} L_i L_j E_k$. Here $L_{i,j}$ denotes the left–handed lepton and squark superfield and E_k the corresponding right–handed field [32].

The resonance curve for the process, including the complete SM–background is given in Figure 13. The event rates at the peak are given in Table 2.6. Electron polarization with $(-80, 0)$ enhances the signal only slightly by about 2%, whereas the simultaneous polarization of both beams with $(-80, -60)$ produces a further increase by about 20%. The background changes only slightly due to the t–channel (LL) contributions from γ and Z exchange.

This configuration of beam polarizations, which strongly suppresses pure SM processes, allows one to perform fast diagnostics for this R–parity violating process. For example the process $e^+e^- \to Z'$ could lead to a similar resonance peak, but with different polarization dependence. Here only the 'normal' configurations LR and RL play a role and this process will be strongly suppressed by LL. Therefore such a resonance curve, Figure 13, with different beam polarizations would uniquely identify an an R–parity violating SUSY process.

Table 2.6: SUSY – Sneutrino production in R–parity violating SUSY: Cross sections of $e^+e^- \rightarrow \tilde{\nu} \rightarrow e^+e^-$ for unpolarized beams, $P_{e^-} = -80\%$ and unpolarized positrons and $P_{e^-} = -80\%$, $P_{e^+} = -60\%$. The study was made for $m_{\tilde{\nu}} = 650$ GeV, $\Gamma_{\tilde{\nu}} = 1$ GeV, an angle cut of $45^0 \leq \theta \leq 135^0$ and the R–parity violating coupling $\lambda_{131} = 0.05$ [32].

	$\sigma(e^+e^- \rightarrow e^+e^-)$ with $\sigma(e^+e^- \rightarrow \tilde{\nu} \rightarrow e^+e^-)$	Bhabha–background
unpolarized	7.17 pb	4.50 pb
$P_{e^-} = -80\%$	7.32 pb	4.63 pb
$P_{e^-} = -80\%$, $P_{e^+} = -60\%$	8.66 pb	4.69 pb
$P_{e^-} = -80\%$, $P_{e^+} = +60\%$	5.97 pb	4.58 pb

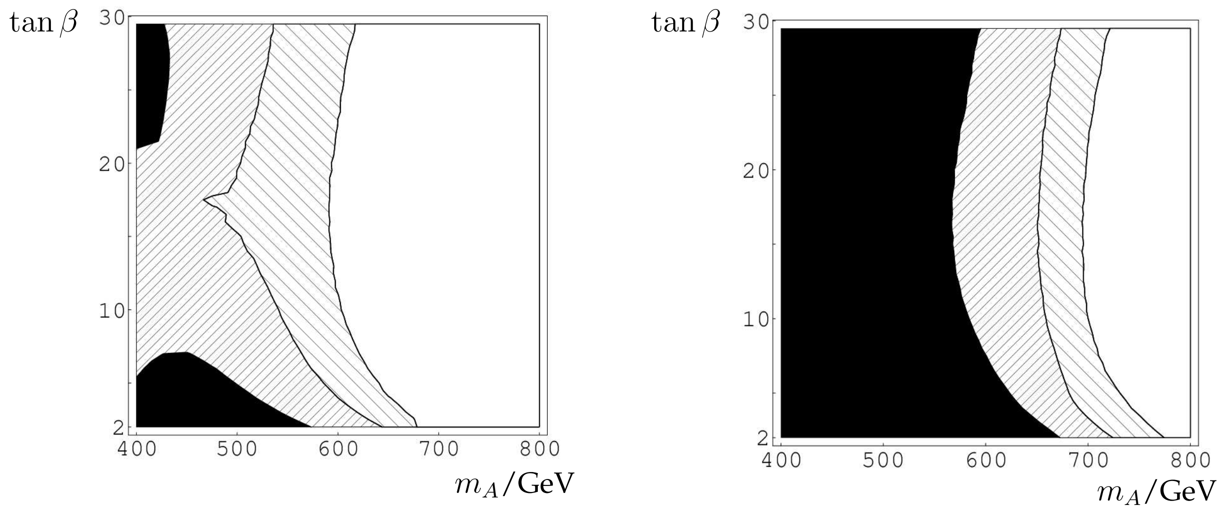

Figure 14: Cross section of heavy Higgs production with $\sigma(e^+e^- \to HA) > 0.5$ fb (black region), > 0.2 fb (right dashed) and > 0.1 fb (left dashed) for unpolarised beams (left) and with both beams polarised, $P_{e^-} = -80\%$, $P_{e^+} = +60\%$ (right) at $\sqrt{s} = 500$ GeV and with an integrated luminosity of $\mathcal{L} = 2$ ab^{-1}.

2.3.6 Production of heavy Higgs bosons in weak boson fusion

The possibility to enhance cross sections by using beam polarization can be very important for detecting processes with a very low rate. In Ref. [18] the production of the heavy neutral $\mathcal{CP}$-even Higgs boson H of the MSSM was studied. Since for large values of the $\mathcal{CP}$-odd Higgs boson mass M_A the heavy Higgs bosons A and H are approximately mass degenerate, $M_A \approx M_H$, the pair production channel $e^+e^- \to HA$ is limited by kinematics to the region $M_H < \sqrt{s}/2$. The kinematic limit of the LC can in principle be extended by single Higgs production in the process $e^+e^- \to \nu\bar{\nu}H$. However, due to the decoupling properties of the heavy Higgs bosons for $M_A \gg M_Z$ the VVH coupling ($V = W^\pm, Z$) is very small, so that the process $e^+e^- \to \nu\bar{\nu}H$ has only a very low rate.

In Ref. [18] it was shown that higher-order contributions to this Higgs-boson production process can remedy this situation, making the process potentially accessible at the LC. This requires a high integrated luminosity and polarized beams. The cross section becomes enhanced for left-handedly polarized electrons and right-handedly polarized positrons. While an 80% polarization of the electron beam alone results in a cross section that is enhanced by a factor 1.8, the polarization of both beams, i.e. 80% polarization for electrons and 60% polarization for positrons, would yield roughly an enhancement by a factor of 2.9. With an anticipated integrated luminosity of the LC running at its highest energy of $\mathcal{O}(2\mathrm{ab}^{-1})$ the enhancement in the cross section due to the beam polarization can extend the kinematic reach of the LC by roughly 100 GeV, see Fig. 14 (right) compared to the case of unpolarized beams, Fig. 14 (left).

2.4 New physics searches in fermion pair production

2.4.1 Model-independent contact-interaction analysis

Although the production of SM fermion-pairs is not primarily devoted to the search for new phenomena, it guarantees – due to its clear signature of the final states in the detector and high statistics – a good sensitivity to deviations from the SM expectations. Physics beyond the SM could so be found at a LC operating far below the production threshold of new particles.

Generally, contact interactions (CI) represent an effective expression of a non-standard dynamics characterized by one (or more) new and very large mass scale exchanges, valid in quark and lepton reactions at the "low" energies $\sqrt{s} \ll \Lambda$ attainable by current and future accelerators. In this case, the new interactions and dynamical mass scales can manifest themselves only indirectly, through deviations of the measured cross sections from the Standard Model (SM) predictions that, being dimensionally suppressed by some power of $\sqrt{s}/\Lambda$, are expected to be quite small.

We study fermion pair production proces

$$e^+ + e^- \to f + \bar{f}, \tag{9}$$

with $f \neq t$, at an electron-positron Linear Collider (LC) with c.m. energy $\sqrt{s} = 0.5\,\mathrm{TeV}$ and polarized electron and positron beams, and to the general, $SU(3)\times SU(2)\times U(1)$ symmetric $eeff$ dimension $D = 6$ contact-interaction Lagrangian, with helicity-conserving and flavor-diagonal fermion currents [54]:

$$\mathcal{L}_{\mathrm{CI}} = \frac{1}{1+\delta_{ef}} \sum_{i,j} g^2_{\mathrm{eff}}\, \epsilon_{ij} \left(\bar{e}_i \gamma_\mu e_i\right) \left(\bar{f}_j \gamma^\mu f_j\right). \tag{10}$$

In Eq. (10): $i, j = \mathrm{L}, \mathrm{R}$ denote left- or right-handed helicities, generation and color indices have been suppressed, and the CI coupling constants are parameterized in terms of corresponding mass scales as $\epsilon_{ij} = \eta_{ij}/\Lambda^2_{ij}$ with $\eta_{ij} = \pm 1, 0$ depending on the chiral structure of the individual interactions. Also, conventionally $g^2_{\mathrm{eff}} = 4\pi$, as a reminder that, in the case of compositeness, the new interaction would become strong at $\sqrt{s}$ of the order of Λ_{ij}. Obviously, deviations from the SM and upper bounds or exclusion ranges for the CI couplings can be equivalently expressed as lower bounds and exclusion ranges for the corresponding mass scales Λ_{ij}.

For a given final fermion flavor, apart from the $\pm$ signs, Eq. (10) envisages four individual, and independent, CI couplings in the case $f \neq e$ and three couplings in the elastic $f = e$ case. Correspondingly, the most general (and model-independent) analysis of the process (9) must account for the complicated situation where the full Eq. (10) is included in the expression for the cross section, and all CI couplings can appear there simultaneously as free, non-vanishing, parameters.

A simplifying procedure is to assume non-zero values for only one of the couplings (or one specific combination of them) at a time with all others set to zero, which would avoid problems associated with negative interference, and leads to tests of *specific* CI models only.

On the other hand, it should be highly desirable to apply a more general kind of experimental data analysis that simultaneously includes all terms of Eq. (10) as independent free parameters and, at the same time, allows the derivation of separate constraints (or exclusion regions) on the individual coupling constants. A strong possibility in this regard is offered by the availability of initial electron and positron longitudinal beam polarizations, that enable to extract from the measured data the individual helicity cross sections σ_{ij} through the definition of particular, and optimal, polarized integrated cross sections and, consequently, to disentangle the constraints on the corresponding CI coupling constants ϵ_{ij} [55–57]. Accordingly, a model-independent approach, in the sense stated above, is obtained. Also, it is a well-known fact that, when both the electron and positron beams are polarized, the total annihilation cross section into fermion-antifermion pairs will be increased by a factor [58,59] and, in principle, one could expect a corresponding increase in sensitivity to the new parameters. Taking into account only the statistical errors the sensitivity for these dimension d=6 operators scales with

$$\frac{m_X}{g_X} \sim \sqrt{\Delta_{stat}\sigma} \sim (\mathcal{L}_{int} \cdot s)^{1/4} \tag{11}$$

Polarized observables for contact interactions

The analysis of contact-interactions of Ref. [55], that we are briefly summarizing here, is limited to the cases $f \neq e, t$ where the SM is determined by only s-channel γ and Z exchanges and external fermion masses are negligible, and uses as basic observables, to be determined from angular integration of differential rates of events observed with longitudinally polarized beams, the (unpolarized) total cross section $\sigma_{\rm unpol}$ and forward-backward asymmetry $A_{\rm FB}$, the left-right asymmetry $A_{\rm LR}$ and left-right forward-backward asymmetry $A_{\rm LR,FB}$. These are defined, in the notation of Ref. [60], as:

$$\sigma_{\rm unpol} = \frac{1}{4}\left[\sigma_{\rm LL} + \sigma_{\rm LR} + \sigma_{\rm RR} + \sigma_{\rm RL}\right], \tag{12}$$

$$A_{\rm FB} = \frac{3}{4}\,\frac{\sigma_{\rm LL} - \sigma_{\rm LR} + \sigma_{\rm RR} - \sigma_{\rm RL}}{\sigma_{\rm LL} + \sigma_{\rm LR} + \sigma_{\rm RR} + \sigma_{\rm RL}}, \tag{13}$$

$$A_{\rm LR} = \frac{\sigma_{\rm LL} + \sigma_{\rm LR} - \sigma_{\rm RR} - \sigma_{\rm RL}}{\sigma_{\rm LL} + \sigma_{\rm LR} + \sigma_{\rm RR} + \sigma_{\rm RL}}, \tag{14}$$

and

$$A_{\rm LR,FB} = \frac{3}{4}\,\frac{\sigma_{\rm LL} - \sigma_{\rm RR} + \sigma_{\rm RL} - \sigma_{\rm LR}}{\sigma_{\rm LL} + \sigma_{\rm RR} + \sigma_{\rm RL} + \sigma_{\rm LR}}. \tag{15}$$

The deviations of these observables from the SM predictions are easily expressed in terms of SM couplings and the CI ones, ϵ_{ij}, of Eq. (10).

The correlation among uncertainties on the four basic observables can be taken into account *via* the method of the covariance matrix [61,62].

As numerical inputs, we assume as reference values the identification efficiencies [63]: 60% and 35% for the channels for $b\bar{b}$ and $c\bar{c}$, respectively. To assess the relative roles of statistical and systematic uncertainties, we vary the time-integrated luminosity $\mathcal{L}_{\rm int}$ from 50 to 500 fb^{-1} with uncertainty $\delta\mathcal{L}_{\rm int}/\mathcal{L}_{\rm int} = 0.5\%$, and a fiducial experimental angular range $|\cos\theta| \leq 0.99$. Regarding electron and positron degrees of polarization, we consider the values: $|P_e| = 0.8$; $|P_{\bar{e}}| = 0.0$, and 0.6, with the uncertainties $\delta P_e/P_e = \delta P_{\bar{e}}/P_{\bar{e}} = 0.5\ \%$.

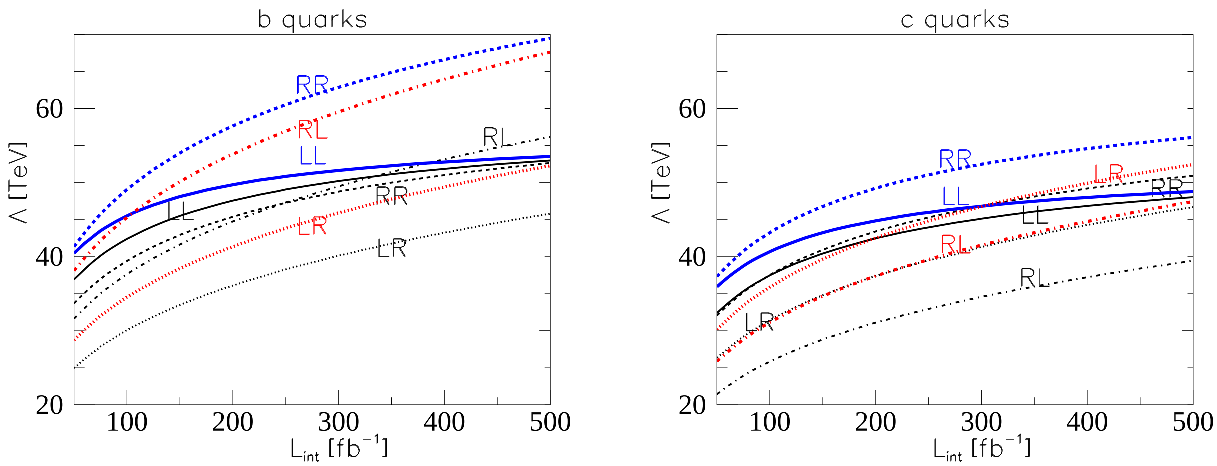

Figure 15: Contact-interaction scale Λ vs. integrated luminosity, $\mathcal{L}_{\rm int}$, for b and c quarks, and for the four helicity combinations. Thin curves: $P_e = 0.8$, $P_{\bar{e}} = 0$, heavy curves: $P_e = 0.8$, $P_{\bar{e}} = 0.6$.

The model-independent bounds on the mass scales Λ_{ij} at the 95% C.L. allowed by the experimental uncertainties reported above are shown in Fig. 15 for the considered annihilation channels, respectively. In the figure, heavy curves correspond to $|P_e| = 0.8, |P_{\bar{e}}| = 0.6$ while thin curves correspond to $|P_e| = 0.8, |P_{\bar{e}}| = 0.0$.

As one can see from Eqs. (12) and (13), without simplifying assumptions in the unpolarized case the CI couplings could not be individually constrained within finite ranges, but only mutual correlations could be derived. With initial longitudinal beam polarization, the two additional available physical observables (14) and (15) are essential to obtain finite, model-independent, bounds. In principle, electron beam polarization would be sufficient to achieve this result but, depending on the luminosity and the final $f\bar{f}$ channel, a significant increase on the sensitivity to CI couplings can arise from the additional availability of positron polarization. This increase is due to two effects of having both beams simultaneously polarised:

a) increase of the effective polarisation from e.g. 80% ($P_{e^-} = 80\%$) to $P_{eff} = 95\%$ ($P_{e^-} = \pm 80\%$, $P_{e^+} = \mp 60\%$), cf. section 1.3;

b) error reduction of P_{eff} (cf. also section 1.3) followed by the higher accuracy of the A_{LR} measurement:

$$\Delta A_{LR} = \sqrt{(\Delta_{stat} A_{LR})^2 + (\Delta_{sys} A_{LR})^2} = \sqrt{\frac{1 - P_{eff}^2 A_{LR}^2}{N P_{eff}^2} + A_{LR}^2 (\frac{\Delta P_{eff}}{P_{eff}})^2} \qquad (16)$$

As one can see from eq. (16) the systematic error can be substantially reduced with positron polarisation. We show in Figs. 16 the expected sensitivity for different contact interactions in $e^+e^- \rightarrow b\bar{b}$, $c\bar{c}$ including systematic ($\Delta sys = 0\%$, 0.5%, 1.0%), luminosity ($\Delta L = 0.2\%, 0.5\%$) and polarisation uncertainties ($\Delta P/P = 0\%, 0.5\%$) and it can clearly be seen that the reduction of systematic errors will be decisive. The study was done for $\sqrt{s} = 800$ GeV [16].

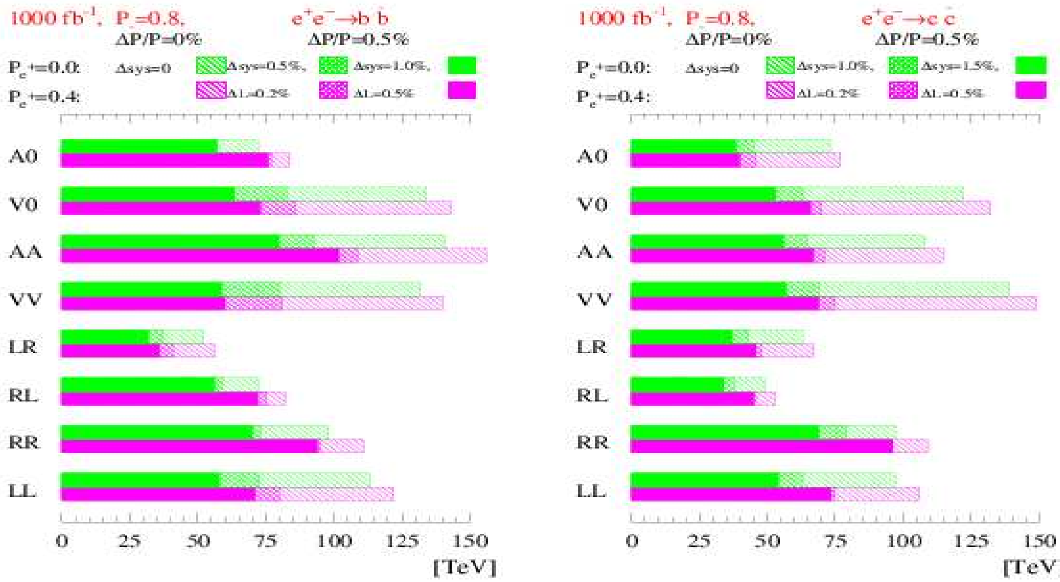

Figure 16: Left: Limits on contact interactions from $\mathrm{e^+e^-} \to \mathrm{b\bar{b}}$ and $e^+e^- \to c\bar{c}$ without positron polarization and with 40% polarization including different uncertainty scenarios [16].

2.4.2 Sensitivity to neutral extra gauge bosons

Extra neutral gauge bosons Z′ can also be probed by its virtual effects on cross sections and asymmetries. Below a Z′ resonance measurements of fermion-pair production are sensitive only to the ratio of Z′ couplings and Z′ mass. Therefore, limits on the Z′ mass can be obtained only in dependence on a model with given Z′ couplings. For the well-known E6 and LR models, e.g., mass sensitivities between $4 \cdot \sqrt{s}$ and $14 \cdot \sqrt{s}$ are reached. Thus, a LC operating at $\sqrt{s} = 800$ GeV may exceed the sensitivity of the LHC (which is about 4-5 TeV) to a potential Z′ in some models. If a Z′ will be detected at LHC its origin can be found by determining the Z′ couplings, see Fig. 17a [17]. Positron beam polarisation improves only slightly the resolution power for Z′ models in case of leptonic final states, but it will be quite important for the measurement of the Z′ couplings to fermions. The crucial point in the analyses are the systematic errors, which can be significantly reduced with the use of both beams polarised [16, 17].

2.4.3 CI analysis in Bhabha scattering

With $\delta_{ef} = 1$ the four-fermion contact interaction Lagrangian of Eq. (10) is relevant to the Bhabha scattering process

$$e^+ + e^- \to e^+ + e^-. \tag{17}$$

Different from the annihilation processes considered in Sect. 2.4.1, in the case of processes (17), apart from the $\pm$ signs, there are only three (not four) independent CI couplings: $\epsilon_{\rm LL}$, $\epsilon_{\rm RR}$ and $\epsilon_{\rm LR} = \epsilon_{\rm RL}$ (same ϵ's for the two processes). The other principal difference, that complicates the procedure to disentangle the constraints on individual couplings, is that Bhabha scattering is determined, in the SM, by γ and Z exchanges in both the s- and t-channels. We assume that the polarization of each beam can be changed on a pulse by pulse basis, which allows the separate measurements of the polarized differ-

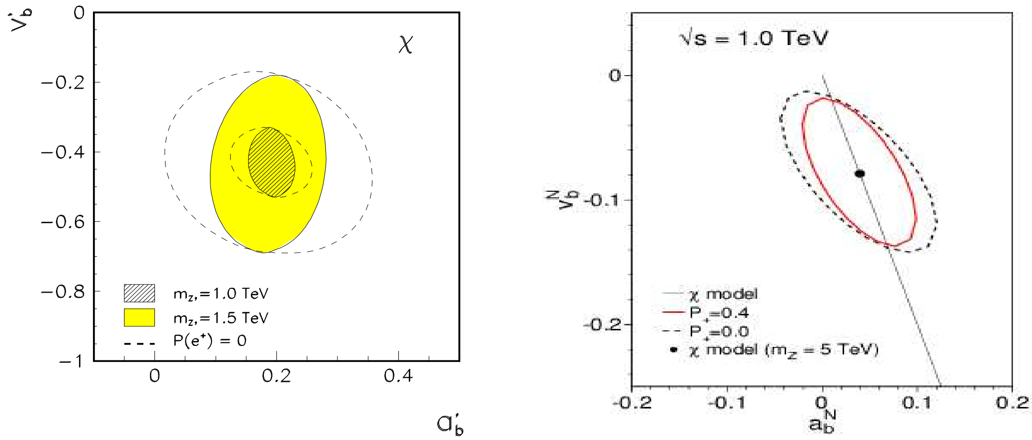

Figure 17: Left: 95% CL contours for ($a_b^{'}$, $v_b^{'}$) for $M_{Z'} = 1$, 1.5 TeV in the χ model and $\sqrt{s} = 500$ GeV and $\mathcal{L} = 500$ fb^{-1}. The dash lines correspond to $P_{e^+} = 0$ [17]; Right: Expected resolution power (95% CL) to reconstruct a Z′ ($m_{Z'} = 5$ TeV) realised in the χ model without positron polarisation and with 40% polarisation based on the measurement of $b\bar{b}$ final states. The Z′ mass is assumed to be unknown in this case [16].

ential cross sections dσ_{++}, dσ_{+-} and dσ_{-+}, corresponding to the configurations of beam polarizations $(P_e, P_{\bar{e}}) = (P_1, P_2)$, $(P_1, -P_2)$ and $(-P_1, P_2)$, respectively, with $P_{1,2} > 0$ [64]. They are related to combinations of helicity cross sections dσ_{R}, dσ_{L} and d$\sigma_{\mathrm{LR},t}$ containing the CI couplings and therefore representing the basic observables for the analysis, by a system of linear equations [64]. It turns out that, while $\sigma_{\mathrm{LR},t}$ (that is pure t-pole) depends on a single contact interaction parameter (ϵ_{LR}), which therefore can be *directly* disentangled from the other couplings, σ_{R} and σ_{L} simultaneously depend on *pairs* of parameters, (ϵ_{RR},ϵ_{LR}) and (ϵ_{RR},ϵ_{LR}), respectively, and in this case (ellipsoidal) allowed areas in the relevant planes can be obtained. This clearly shows that *both* electron *and* positron polarization are needed to perform a *model-independent* analysis of CI couplings in Bhabha scattering. One can easily see that, without polarization ($P_1 = P_2 = 0$), in the general case only correlations among couplings can be derived and, in particular, the contribution of ϵ_{LR} is subject to partial cancellations.

To assess the sensitivity of Bhabha scattering to the compositeness scale, in Fig. 18 we depict as an example the 95% C.L. contours around $\epsilon_{\mathrm{LL}} = \epsilon_{\mathrm{RR}} = \epsilon_{\mathrm{LR}}$ in the two-dimensional planes (ϵ_{RR},ϵ_{LR}) and (ϵ_{RR},ϵ_{LR}), derived from a χ^2 analysis of differential cross sections, assuming that no deviation from the SM within the experimental uncertainty (statistical and systematic) is measured in dσ_{L}, dσ_{R} and d$\sigma_{\mathrm{LR},t}$ ($\mathcal{L}_{\mathrm{int}}(e^+e^-) = 50$ fb^{-1}, $P_1 = 0.8$, $P_2 = 0.6$, $\delta\mathcal{L}_{\mathrm{int}}/\mathcal{L}_{\mathrm{int}} = \delta P_1/P_1 = \delta P_2/P_2 = 0.5\%$). The crosses indicate the constraints obtained by taking one non-zero parameter at a time instead of two simultaneously non-zero and independent.

Comparison with Moeller scattering, [55], shows that only in case that $\mathcal{L}_{\mathrm{int}}(e^-e^-)$ is not too low, Bhabha and Moeller scattering are complementary concerning the sensitivity to individual couplings in a model-independent data analysis.

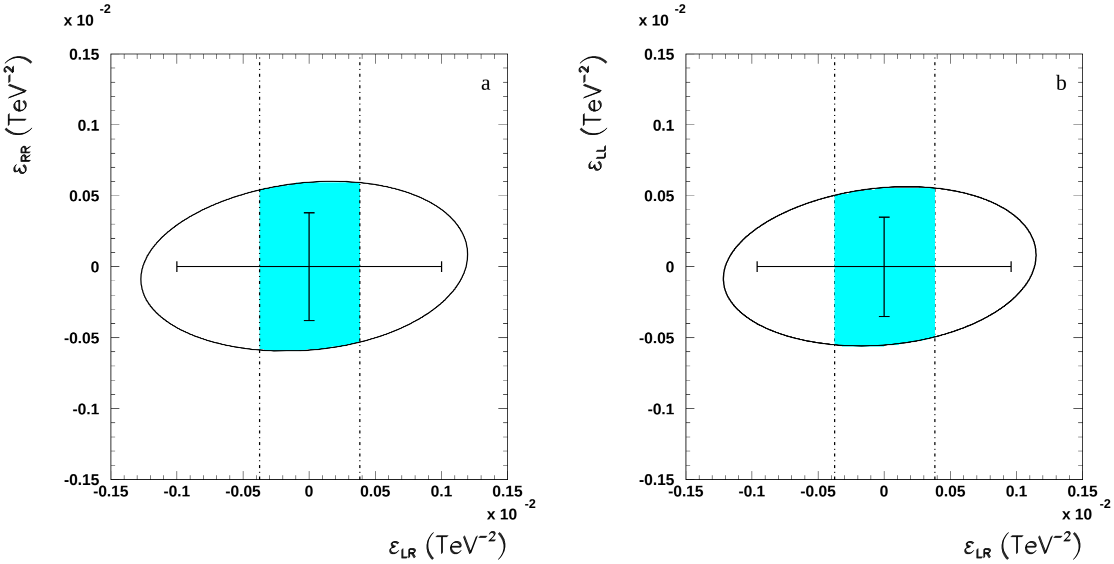

Figure 18: Allowed areas at 95% C.L. in the planes $(\epsilon_{\rm LR},\epsilon_{\rm RR})$ and $(\epsilon_{\rm LR},\epsilon_{\rm LL})$ obtained from $\sigma_{\rm R}$ and $\sigma_{\rm L}$ in $e^+e^- \to e^+e^-$ at $\sqrt{s}=0.5$ TeV, $\mathcal{L}_{\rm int}(e^+e^-)=50\ {\rm fb}^{-1}$, $|P_e|=0.8$, $|P_{\bar{e}}|=0.6$. Vertical dashed lines indicate the range allowed to $\epsilon_{\rm LR}$ by $\sigma_{{\rm LR},t}$.

2.4.4 Identification of graviton exchange effects

Effects from large extra dimensions in the ADD scenario [65] can also be probed by virtual effects in the framework of contact interactions, by the effective Lagrangian [67]

$$\mathcal{L}=i\frac{4\lambda}{M_H^4}T_{\mu\nu}T^{\mu\nu}, \tag{18}$$

where $T_{\mu\nu}$ is the energy-momentum tensor and λ is a sign factor ($\lambda=\pm1$). The only difference that remains would be that, compared to the previous contact-interaction Lagrangian (10), being induced by a dimension $D=8$ operator the KK graviton exchange is suppressed by the much higher power $(\sqrt{s}/M_H)^4$, so that a lower reach on M_H can be expected in comparison to the constraints obtainable, at the same c.m. energy, on the Λ's.

The scaling law for the reach scales correspondingly as

$$m_H\sim[s^{(d-5)}\mathcal{L}_{int}]^{1/(2d-8)}=(s^3\cdot\mathcal{L}_{int})^{1/8}. \tag{19}$$

Due to the different angular dependence [16] of deviations produced by the exchange of the spin-2 particle and those from the interactions represented by (10), a particularly suitable observable is represented by the generalized centre-edge asymmetry among integrated differential distributions [68]:

$$A_{\rm CE}=\frac{\sigma_{\rm CE}}{\sigma},\qquad \sigma_{\rm CE}=\left[\int_{-z^*}^{z^*}-\left(\int_{-1}^{-z^*}+\int_{z^*}^{1}\right)\right]\frac{{\rm d}\sigma}{{\rm d}z}\,{\rm d}z,\qquad \sigma=\int_{-1}^{1}\frac{{\rm d}\sigma}{{\rm d}z}\,{\rm d}z \tag{20}$$

and $0<z^*<1$ ($z=\cos\theta$ with θ the angle between electron and outgoing fermion in the c.m.). The asymmetry (20) projects out the "conventional" contact interactions and provides a clear signature for graviton exchange. In Table 2.7 (left) we list some values for the 5σ identification reach on the mass scale M_H, summing over the channels $f = \mu, \tau, b, c$, that can be obtained at the LC by a χ^2 analysis assuming that no deviation $\Delta A_{\rm CE}$ is seen.

Longitudinal beam polarization appears to increase the sensitivity to graviton exchange, although the impact on M_H is less dramatic in this case due to the suppression $(\sqrt{s}/M_H)^4$ of the graviton coupling. Instead, initial polarization can be seen to play a key role in distinguishing graviton exchange from competing effects, see next section [68,69].

2.4.5 Use of transversely polarized beams

In this section we concentrate on the unique distinction between effects of graviton exchange and 'conventional' contact interaction sources. One elegant tool which becomes only available at the LC provided both the e^- and e^+ beams are transversely polarized beams. As we will see below, transverse polarization (TP) [105,106] allows for new asymmetries to be constructed which are associated with the azimuthal angle formed by the directions of the $e^\pm$ polarization and the plane of the momenta of the outgoing fermions in the $e^+e^- \to f\bar{f}$ process. We are interested in using the associated TP asymmetries to uniquely probe for the s-channel exchange of spin-2 fields in e^+e^- collisions which we normally associate with the Kaluza-Klein graviton towers of the Arkani-Hamed, Dimopoulos and Dvali(ADD) [100] or Randall-Sundrum(RS) [101] scenarios. In what follows we will always assume that we are below the threshold for the production of these resonances otherwise the spin-2 nature of the new exchange would be easily identified through an examination of the resonances themselves.

Transverse Polarization Asymmetries

Consider the process $e^+e^- \to f\bar{f}$ with the both electron and positron beams polarized. We will denote the linear and transverse components of the $e^-(e^+)$ polarizations by $P_{L,T}(P'_{L,T})$ and for simplicity assume that the two transverse polarization vectors are parallel up to a sign. In this case, the spin-averaged matrix element for this process can be written as

$$\begin{aligned} |\bar{\mathcal{M}}|^2 &= \frac{1}{4}(1-P_LP'_L)(|T_+|^2+|T_-|^2)+(P_L-P'_L)(|T_+|^2-|T_-|^2) \\ &+ (2P_TP'_T)[\cos 2\phi\; Re(T_+T_-^*)-\sin 2\phi\; Im(T_+T_-^*)]\,, \end{aligned} \tag{21}$$

where ϕ is the azimuthal angle defined on an event-by-event basis described above. The $\phi-$dependent pieces of $|\bar{\mathcal{M}}|^2$ are sensitive to the relative phases between the two sets of amplitudes. We note from eq. (21) that the ϕ-dependent pieces are *only* accessible if both beams are simultaneously transversely polarized.

Let us first consider the simple case with massless fermions. Without scalar exchange but allowing for the possibility of spin-2 the relevant helicity amplitudes for this process are given by

$$\begin{aligned} T^{+-}_{+-} &= f_{LL}(1+z)-f_g(z+2z^2-1) \\ T^{-+}_{+-} &= f_{LR}(1-z)-f_g(z-2z^2+1) \\ T^{+-}_{-+} &= f_{RL}(1-z)-f_g(z-2z^2+1) \\ T^{-+}_{-+} &= f_{RR}(1+z)-f_g(z+2z^2-1)\,. \end{aligned} \tag{22}$$

where $z=\cos\theta$ and $f_{L,R}$ are combinations of the vector and axial vector couplings of eZ. Note that the spin-2 exchange merely augments the amplitudes which are already present in the SM(though with different $\cos\theta$ dependencies), *i.e.*, no new helicity amplitudes are generated by spin-2. f_g is a model-dependent quantity; in the usual ADD model, employing the convention of Hewett [98], one finds

$$f_g = \frac{\lambda s^2}{4\pi\alpha M_H^4}\,. \tag{23}$$

where M_H represents the cutoff scale in the KK graviton tower sum and $\lambda = \pm 1$. In the RS model the corresponding expression can be obtained through the replacement

$$\frac{\lambda}{M_H^4} \to \frac{-1}{8\Lambda_\pi^2} \sum_n \frac{1}{s - m_n^2 + i m_n \Gamma_n} \,. \tag{24}$$

where Λ_π is of order a few TeV and $m_n(\Gamma_n)$ are the masses(widths) of the TeV scale graviton KK excitations. We will also assume that their widths can be neglected in cross section calculations.

In the case of massive final state fermions, such as tops, the helicity amplitudes given above are slightly altered and new amplitudes $T_{+-}^{\pm\pm}$ and $T_{-+}^{\pm\pm}$ are also present. They will be included in the analysis in the case of top quark pair production.

Both of these ϕ-dependent terms are always proportional to $1-z^2$ in the SM, as shown in [105, 106] and will remain so even if new gauge boson exchanges are present. Due to the more complex z-dependence of the spin-2 contributions to the helicity amplitudes significant modifications occur when gravitons are exchanged: interference between SM and spin-2 exchange amplitudes produce both even and odd$-z$ terms with the latter proportional to $\sim z(1-z^2)$ whereas the smaller pure gravity terms are instead found to be even in z and proportional to $z^2-(2z^2-1)^2$. The general difference in the z-dependence of the of the ϕ sensitive terms and, in particular, the existence of the odd-z contributions is clearly a signal for spin-2 exchange.

We define a differential azimuthal asymmetry distribution by

$$\frac{1}{N}\frac{dA}{dz} = \left[\frac{\int_+ \frac{d\sigma}{dz d\phi} - \int_- \frac{d\sigma}{dz d\phi}}{\int d\sigma} \right], \tag{25}$$

where $\int_\pm$ are integrations over regions where $\cos 2\phi$ takes on $\pm$ values; integration over the full ranges of z and ϕ occurs in the denominator. The differential asymmetry to takes on rather small numerical values since it is normalized to the total cross section and *not* to the differential cross section at the same value of z as is usually done. We show the asymmetry for both the SM and in the ADD scenario in Fig. 19 at a 500 GeV LC for the final states $f = \mu$ or τ, c and b. Note that from here on we will combine results for the $f = \mu$ and τ final states to get added statistics. We have for concreteness assumed that the spin rotators are 100% efficient [107] so that $P_T = 0.8$ and $P_T' = 0.6$. As we can see from Fig. 19 the spin-2 effects cause a strong asymmetric behaviour under $z \to -z$ exchange.

To access the odd-z terms one can take the differential azimuthal asymmetry defined above, separately integrate it over positive and negative values of z, and form a forward-backward asymmetry using $N^{-1}dA/dz$:

$$A_{FB} = \frac{1}{N}\left[\int_{z\geq 0} dz\, \frac{dA}{dz} - \int_{z\leq 0} dz\, \frac{dA}{dz} \right]. \tag{26}$$

In the SM and in any new physics scenario with s-channel Z' exchanges one has $A_{FB} = 0$. This is also true in the usual four-fermion contact interaction scenario [109] which involves only vector and axial-vector couplings. Due to the nature of spin-0 exchange A_{FB} would remain zero in this case as well.

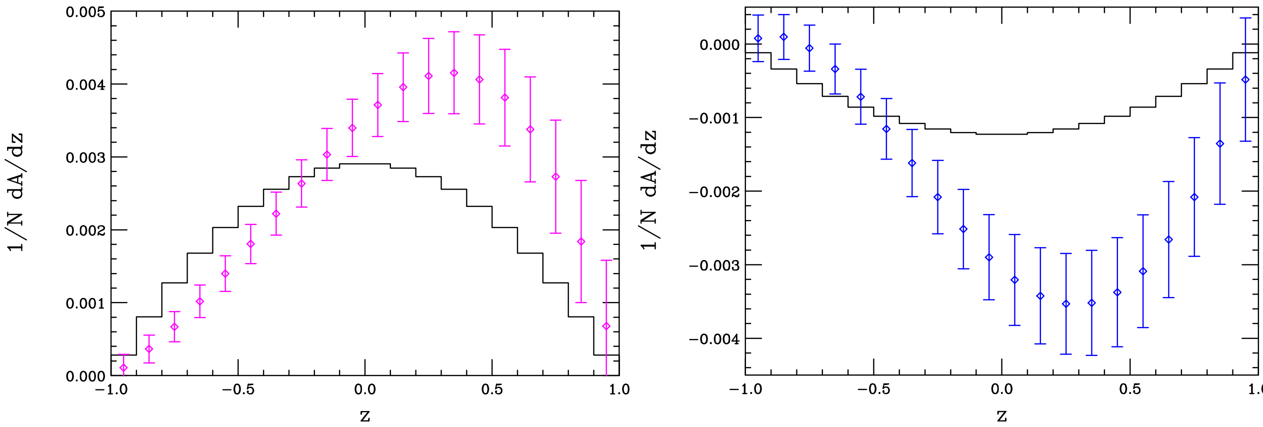

Figure 19: Differential azimuthal asymmetry distribution for $e^+e^- \to f\bar{f}$, i.e. $c\bar{c}$ (left) and $b\bar{b}$ (right), at a 500 GeV LC assuming a luminosity of $500\ fb^{-1}$. The histograms are the SM predictions while the data points assume the ADD model with $M_H = 1.5$ TeV. $P_T = 0.8$ and $P_T' = 0.6$ are assumed.

5 σ reach in M_H/TeV	$\mathcal{L}_{int}$/fb^{-1} 100	300	500
unpolarised beams	2.3	2.6	2.9
$P_{e^-} = +0.8$	2.5	2.8	3.05
$P_{e^-} = +0.8$, $P_{e^+} = -0.6$	2.45	3.0	3.25

5 σ reach in M_H/TeV	$\mathcal{L}_{int}$/fb^{-1} 100	300	500	1000
$\sqrt{s} = 0.5$ TeV	1.6	1.9	2.0	2.2
$\sqrt{s} = 0.8$ TeV	2.4	2.6	2.8	3.1
$\sqrt{s} = 1.0$ TeV	2.8	3.2	3.4	3.8

Table 2.7: Left: 5σ reach on the mass scale M_H *vs.* integrated luminosity from the process $e^+e^- \to f\bar{f}$, with f summed over μ, τ, b, c, and for the energy 0.5 TeV [68] (cf. also [16], where the 95% CL sensitivy for M_H in $e^+e^- \to \mu\bar{\mu}, c\bar{c}, b\bar{b}$ has been simulated); Right: 5σ identification reach in M_H *vs.* integrated luminosity using A_{FB} as a function of the integrated luminosity from the process $e^+e^- \to f\bar{f}$, with f summed over μ, τ, b, c and t. Here $P_T = 0.8$ and $P_T' = 0.6$ are assumed. [113]

Analysis

In what follows we concentrate on the ADD model; (almost) all limits obtained there can be immediately translated to the case of the RS scenario. From Fig.19 it is apparent that modest values of M_H cause quite sizeable distortions in the $N^{-1}dA/dz$ distribution. However, as we will see this sensitivity is somewhat diluted if we are only asking whether or not, *e.g.* A_{FB} is non-zero. To determine the 5σ *identification* reach, given in Table 2.7 (right), we will assume that the individual polarizations are known rather well, $\delta P/P = 0.003$, that the efficiencies of identifying the final state fermions is rather high: 100% for $f = \mu, \tau$, 60% for $f = c, t$, and 80% for $f = b$ with no associated systematic uncertainties and include the effects of initial state radiation. In obtaining these results we have combined all of the various final states above into a single fit. In all cases a small angle cut of 100 mrad around the beam pipe has been employed.

It can be stated that the identification reach in either case alone, $M_H \sim (3.5-4)\sqrt{s}$, is not as good as what can be obtained employing longitudinal polarization [16,68,108].

Since in the SM and all Z' models and in the case of conventional four-fermion contact interactions the azimuthal asymmetry always takes the form $N^{-1}dA/dz \sim (1-z^2)$, we can study up to what value of the cutoff scale, M_H, can we differentiate the effects of gravity

– a change in the *shape* of these distributions – from a simple overall change in the normalization of distributions for the various final states. This allows us to set a limit on the value of M_H below which graviton exchange can be distinguished from Z' exchange or four-fermion contact interactions. We fix M_H and fit the $N^{-1}dA/dz$ distributions for μ, τ, c and b final states assuming a SM shape but allowing the normalization to float independently for each final state. For luminosities above $100-200\ fb^{-1}$ the errors are completely dominated by systematics and we find the results shown in Table 2.8 (left), 2nd column. Here we see that for $M_H \leq (10-11)\sqrt{s}$ the effects of spin-2 graviton exchange can be distinguished from a Z' or any form of the four-fermion contact interactions. This *identification* reach is numerically similar to the 95% CL *discovery* reach for graviton exchange obtained using only singly longitudinally polarized beams [108, 110, 111] for the same process, see Table 2.7.

E_{CM} (GeV)	Id. reach (TeV)	95% CL (TeV)
500	5.4	10.2
800	8.8	17.0
1000	11.1	21.5
1200	13.3	26.0
1500	16.7	32.7

5 σ reach in M_H/TeV	$\mathcal{L}_{int}$/fb^{-1} 100	300	500	1000
$\sqrt{s} = 0.5$ TeV	1.2	1.3	1.4	1.6
$\sqrt{s} = 0.8$ TeV	1.8	2.0	2.2	2.4
$\sqrt{s} = 1.0$ TeV	2.2	2.4	2.6	2.8

Table 2.8: Left: Identification reach for M_H in the ADD model assuming the distribution $N^{-1}dA/dz \sim 1 - z^2$ for fixed M_H and varying the individual normalizations for the final states $f = \mu, \tau$, $f = b$ and $f = c$ for LC of different center of mass energies; the 95% CL discovery reach: varying M_H up to the CL level; Right: 5σ reach for the discovery of a nonzero value of the azimuthal asymmetry $N^{-1}dA_i/dz$ distribution as a function of the integrated luminosity at a LC for $\delta = 3$. $M_H = M_D$ is assumed throughout as is $P_T = 0.8$ and $P'_T = 0.6$.

In order to transform the results above into the 95% CL discovery reach for M_H we assume that the $N^{-1}dA/dz$ distributions for each final state fermion are given by their SM values and evaluate at what value of M_H the corresponding ones with graviton exchange become indistinguishable from these. Since the errors are completely dominated by systematics we expect our results to again be on the high side of what would be obtained in a more detailed detector study. These results are shown in Table 2.8 (left), 3rd column, where we see that the values are even in the range $M_H \geq 20\sqrt{s}$, cf. also [111].

In the following we concentrate on distinguishing the ADD from the RS model scenarios below KK production threshold with TP. In the RS model, if we are away from the Z and graviton KK poles the imaginary part of amplitude which enters the term proportional to $\sin 2\phi$ becomes vanishingly small. However, as was recently pointed out by [112], the exchange of an essentially continuous spectrum of ADD gravitons leads to a finite, cutoff-independent *imaginary* part of the amplitude, which grows rapidly with increasing $\sqrt{s}$ and depends quite sensitively upon the number of extra dimensions, one now finds that f_g has an imaginary part, depending strongly on the number of extra dimensions.

To proceed [113] we can form a new asymmetry in analogy to the above:

$$\frac{1}{N}\frac{dA_i}{dz} = \left[\frac{\int_+ \frac{d\sigma}{dzd\phi} - \int_- \frac{d\sigma}{dzd\phi}}{\int d\sigma}\right], \tag{27}$$

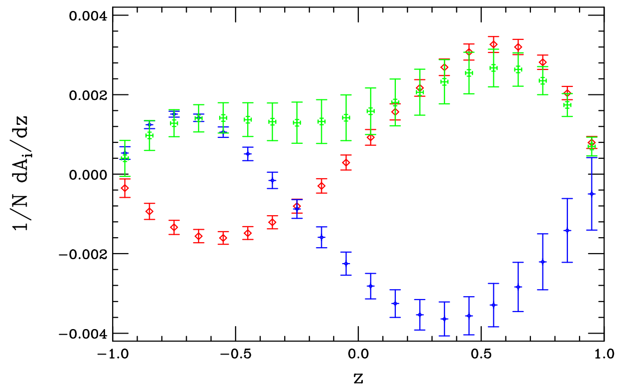

Figure 20: The $N^{-1}dA_i/dz$ distributions at a 500 GeV collider assuming $M_H = M_D = 1.5$ TeV and $\delta = 3$ with an integrated luminosity of 500 fb^{-1}. The plotted points from top to bottom in the center of the plot correspond to $f = b, \mu$ plus τ and c, respectively.

where now the $\int_\pm$ are integrations over regions where $\sin 2\phi$ takes on $\pm$ values and we integrate over all z and ϕ in the denominator as before. All terms proportional to $\cos 2\phi$ are found to cancel implying that there is no cross contamination from this other asymmetry source. Of course this new distribution is identically zero in both the SM as well as the RS model away from the Z and RS KK graviton poles. Thus, observing *any* non-zero value for this quantity is a signal for the ADD model. Table 2.8 (right) shows the 5σ discovery reach for these new asymmetry distributions at a 500 GeV LC assuming as before that $P_T = 0.8$ and $P'_T = 0.6$ and taking $\delta = 3$ for purposes of demonstration. Throughout the analysis we have assumed $M_H = M_D$. In case that $M_H << M_D$ this would lead to a serious modification in the sensitivity to this observable.

We list in Table 2.8 (right) the resulting reaches at the 5σ level (for $\delta = 3$) where the RS and the ADD model could be separated up to $M_H \sim (2.5-3)\sqrt{s}$. Although this number is not large in comparison to those we've obtained in the other analyses above they provide the first indication that these two scenarios can be distinguished at a collider via indirect measurements.

In the process $e^+e^- \rightarrow W^+W^-$ the asymmetry is not symmetric in z in the SM so we can't use our shape fitting trick here as we did for fermions.

Summary and Conclusion

The results of our analysis are as follows: (i) Interference of SM and spin-2 graviton KK exchanges leads to contributions to the azimuthal asymmetry distributions which are odd in $\cos\theta$. Such odd terms do not contribute in the case of other new physics such as a Z', contact interactions, gauge boson KK excitations or the exchange of new scalars. (ii) It is possible to differentiate KK graviton/spin-2 exchanges from all other new physics contributions to contact interactions at the 5σ level up to ADD cutoff scales of $M_H \sim (3.5-4)\sqrt{s}$. (iii) Fitting to the shape of the full differential distribution itself increased the 5σ identification reach substantially to $M_H = (10-11)\sqrt{s}$, about a factor two improvement over what we obtained in the case of longitudinal polarization. (iv) In the ADD model, an additional imaginary piece of the amplitude is present in comparison to the RS model below KK production threshold. Applying a new asymmetry, produced through transverse polarization, allows RS and ADD model separation at 5σ up to masses $M_H = (2.5-3)\sqrt{s}$.

2.5 Seach for CP sensitive observables within the SM particle sector

2.5.1 Triple gauge boson couplings

An important feature of the electroweak Standard Model (SM) is the non-Abelian nature of its gauge group, which gives rise to gauge boson self-interactions, in particular to the triple gauge couplings (TGCs) γWW and ZWW. The most general vertices contain altogether 14 complex parameters [72], six of them CP violating. The SM predicts only four CP conserving real couplings to be non-zero at tree level.

The triple gauge boson vertex WWV (V=Z or γ) can be described in a most general form by an effective Lagrangian [72]

$$\begin{aligned}
\frac{\mathcal{L}^{WWV}}{ig_{WWV}} &= g_1^V V^\mu \left(W^-_{\mu\nu}W^{+\nu} - W^+_{\mu\nu}W^{-\nu}\right) + \kappa_V W^-_\mu W^+_\nu V^{\mu\nu} + \frac{\lambda_V}{M_W^2} V^{\mu\nu} W^{+\rho}_\mu W^-_{\rho\nu} \\
&- ig_4^V W^-_\mu W^+_\nu (\partial^\mu V^\nu + \partial^\nu V^\mu) \\
&+ ig_5^V \varepsilon^{\mu\nu\rho\sigma}\left[(\partial^\rho W^-_\mu)W^+_\nu - W^-_\mu(\partial^\rho W^+_\nu)\right] V_\sigma \\
&+ \frac{\tilde{\kappa}_V}{2} W^-_\mu W^+_\nu \varepsilon^{\mu\nu\rho\sigma} V_{\rho\sigma} + \frac{\tilde{\lambda}_V}{2M_W^2} W^-_{\rho\mu} W^{+\mu}{}_\nu \varepsilon^{\nu\rho\alpha\beta} V_{\alpha\beta},
\end{aligned} \tag{28}$$

which is parametrised by seven real couplings for each vertex. Their behavior under charge (C) and parity (P) conjugation can be used to divide them into four groups. The three couplings g_1^V,κ_V and λ_V conserve C and P, while g_5^V violates C and P but conserves CP. The couplings g_4^V,$\tilde{\kappa}_V$ and $\tilde{\lambda}_V$ violate CP, but g_4^V conserves P, while $\tilde{\kappa}_V$ and $\tilde{\lambda}_V$ conserve C. In the SM at tree level the couplings are g_1^V=κ_V=1, while all other are set to zero. For convenience we introduce $\Delta g_1^\gamma = g_1^\gamma - 1$, $\Delta g_1^Z = g_1^Z - 1$, $\Delta\kappa_\gamma = \kappa_\gamma - 1$ and $\Delta\kappa_Z = \kappa_Z - 1$ thus we are only considering deviations from the standard model values.

Electro-magnetic gauge invariance requires g_1^γ=1 and reduces the number of C and P conserving couplings to 5. SU(2)$_L$ $\times$ U(1)$_Y$ gauge invariance introduces

$$\begin{aligned}
\Delta\kappa_Z &= \Delta\kappa_\gamma \tan\theta_W + \Delta g_1^Z \\
\lambda_Z &= \lambda_\gamma
\end{aligned} \tag{29}$$

for the C and P conserving couplings, where θ_W is the Weinberg angle, thus reducing the number of free couplings further.

A precision measurement of the TGCs at high energies will be a crucial test of the validity of the SM, given that a variety of new physics effects can manifest itself by deviations from the SM predictions (for references see e.g. [73]). Though no deviation from the SM has been found for the TGCs from LEP data [74], the bounds obtained are comparatively weak. The tightest bounds on the anomalous couplings, i.e. on the differences between a coupling and its SM value, are of order 0.05 for Δg_1^Z and λ_γ, of order 0.1 for $\Delta\kappa_\gamma$ and of order 0.1 to 0.6 for the real and imaginary parts of C and/or P violating couplings. These numbers correspond to fits where all anomalous couplings except one are set to zero. Moreover, many couplings, e.g. the imaginary parts of C and P conserving couplings, have been excluded from the analyses so far.

At a future linear e^+e^- collider one will be able to study these couplings with unprecedented accuracy. A process particularly suitable for this is W pair production where both

Table 2.9: 1σ statistical errors in units of 10^{-3} on the real parts of CP conserving TGCs in the presence of all anomalous couplings at $\sqrt{s} = 500$ GeV, with unpolarised beams and with different beam polarisations.

	$\mathrm{Re}\,\Delta g_1^\gamma$	$\mathrm{Re}\,\Delta g_1^Z$	$\mathrm{Re}\,\Delta\kappa_\gamma$	$\mathrm{Re}\,\Delta\kappa_Z$	$\mathrm{Re}\,\lambda_\gamma$	$\mathrm{Re}\,\lambda_Z$	$\mathrm{Re}\,g_5^\gamma$	$\mathrm{Re}\,g_5^Z$
no polarisation	6.5	5.2	1.3	1.4	2.3	1.8	4.4	3.3
$(P_l^-, P_l^+) = (\mp 80\%, 0)$	3.2	2.6	0.61	0.58	1.1	0.86	2.2	1.7
$(P_l^-, P_l^+) = (\mp 80\%, \pm 60\%)$	1.9	1.6	0.40	0.36	0.62	0.50	1.4	1.1
$(P_t^-, P_t^+) = (80\%, 60\%)$	2.8	2.4	0.69	0.82	0.69	0.55	2.5	1.9

the γWW and the ZWW couplings can be measured at the scale given by the c.m. energy $\sqrt{s}$.

Study of TGC with optimal observables

In [73] the prospects to measure the full set of 28 (real) TGCs is systematically investigated for unpolarised beams as well as for longitudinal beam polarisation using optimal observables. They are constructed to give the smallest possible statistical errors for a given event distribution [80]. In addition, they take advantage of the discrete symmetries of the differential cross section. In W pair production the covariance matrix of these observables consists of four blocks that correspond to CP even or CP odd TGCs and to their real or imaginary parts. Within each block all correlations between couplings are taken into account.

Table 2.9 shows the errors on the real parts of CP conserving TGCs at $\sqrt{s} = 500$ GeV with unpolarised beams and with different beam polarisations, assuming an integrated luminosity of 500 fb^{-1}. Here, only those events are considered where one W boson decays into a quark-antiquark pair and the other one into $e\nu$ and $\mu\nu$. It is further assumed that the two jets of the hadronic W decay cannot be identified as originating from the up- and down-type (anti)quark. In the case of longitudinal polarisation the luminosity is distributed equally on both directions of the polarisation vectors and the results are then combined. The errors with unpolarised beams are between 10^{-3} and 10^{-2} in the parameterisation using photon and Z couplings.

At 800 GeV all errors (with or without polarisation) are smaller, notably for $\mathrm{Re}\,\Delta\kappa_\gamma$. For both c.m. energies the errors on the couplings in the γ-Z-parameterisation decrease by about a factor 2 when going from unpolarised beams to longitudinal e^- polarisation and an unpolarised e^+ beam. Going from unpolarised beams to polarised e^- and e^+ this factor is between 3 and 4 for all couplings, except for $\mathrm{Re}\,\Delta\kappa_Z$ at 800 GeV where it is 4.7.

It has been emphasized [80] that the following linear combinations [72] can be measured with much smaller correlations than the γ-Z couplings:

$$\begin{aligned} g_1^L &= 4\sin^2\theta_W\, g_1^\gamma + (2 - 4\sin^2\theta_W)\,\xi\, g_1^Z, \\ g_1^R &= 4\sin^2\theta_W\, g_1^\gamma - 4\sin^2\theta_W\,\xi\, g_1^Z, \end{aligned} \tag{30}$$

where $\xi = s/(s - m_Z^2)$, and similarly for the other couplings. The L- and R-couplings respectively appear in the amplitudes for left- and right-handed initial e^-. Therefore this parameterisation seems to be more "natural" in the presence of beam polarisation than

Table 2.10: Same as Table 2.9, but for the imaginary parts and with the L-R-parameterisation.

	$\mathrm{Im}\, g_1^L$	$\mathrm{Im}\, \kappa_L$	$\mathrm{Im}\, \lambda_L$	$\mathrm{Im}\, g_5^L$	$\tilde{h}_-$	$\tilde{h}_+$	$\mathrm{Im}\, \lambda_R$	$\mathrm{Im}\, g_5^R$
no polarisation	2.7	1.7	0.48	2.5	11	—	3.1	17
$(P_l^-, P_l^+) = (\mp 80\%, 0)$	2.6	1.2	0.45	2.0	4.5	—	1.4	4.3
$(P_l^-, P_l^+) = (\mp 80\%, \pm 60\%)$	2.1	0.95	0.37	1.6	2.5	—	0.75	2.3
$(P_t^-, P_t^+) = (80\%, 60\%)$	2.6	1.2	0.46	2.0	3.7	3.2	0.98	4.4

the conventional one. For detailed plots showing the sensitivity to the TGCs as a function of the degree of longitudinal polarisation we refer to [73]. There an extended optimal-observable method [81] has been used where correlations between TGCs are eliminated through appropriate energy- and polarisation-dependent reparameterisations.

For the imaginary parts of the CP conserving couplings, see Table 2.10, we further use the linear combinations $\tilde{h}_\pm = \mathrm{Im}(g_1^R \pm \kappa_R)/\sqrt{2}$ instead of $\mathrm{Im}\, g_1^R$ and $\mathrm{Im}\, \kappa_R$.

Sensitivity to TGCs at the LC in a true simulation

For comparison with a simulation of determining the charged current triple gauge couplings via a fit [82]. For the simulation we assume a luminosity of $500\,\mathrm{fb}^{-1}$ at a center-of-mass energy of 500 GeV, which is the expected amount of data after one or two years of running. For 800 GeV this corresponds to a luminosity of $1000\,\mathrm{fb}^{-1}$. At both energies we expect roughly 4 millions W-pair events. This huge amount of events give us the possibility to do high precision measurements of the TGCs.

The semileptonic decay channel ($WW \to q\bar{q}\ell\bar{\nu}_\ell$) is used, because of the high branching ration of $43\,\%$ and the good event reconstruction.

There is only one ambiguity in the hadronic decay angles. From LEP analysis [75] we know that the background is very small. The background samples were generated by PYTHIA [116] also including ISR and beamstrahlung.

For the simulation of the proposed detector design we use the fast simulation program SIMDET (version 3.02 [76]), which is based on the proposed detector design, described in the TESLA CDR [77]. It includes a tracking and calorimeter simulation and a reconstruction of energy-flow objects. Concerning more details about data selection see [82].

We use a simple χ^2 fit and apply as input variables the normalized $\cos\theta_W$-distribution and the elements of the spin density matrix of W^+W^- pair. The total cross section is not used. In the case of unpolarized beams we expect a luminosity of $500\,\mathrm{fb}^{-1}$ at a center-of-mass energy of 500 GeV and $1000\,\mathrm{fb}^{-1}$ at 800 GeV in one or two years of running. We consider radiative corrections like initial state radiation (ISR) and beamstrahlung and uncertainties in other measurement like the W-mass and the beam energy, which might have an impact on this measurement.

In the case of polarised beams the total luminosity for one center-of-mass energy is split up equally on both polarizations. In the case of electron polarization this is for an energy of 500 GeV $250\,\mathrm{fb}^{-1}$ on left-handed (L) and $250\,\mathrm{fb}^{-1}$ on right-handed (R) electrons with a polarization of $80\,\%$. In the case of additional polarized positrons the absolute value is $60\,\%$ with opposite polarization with respect to the electron polarization.

To get the maximal sensitivity for this measurement the data taken at both polarization combinations are fitted at the same time. Only this ensures that we can disentangle the WWZ- from the WWγ- couplings. To estimate the systematic error in the TGC measurement from the uncertainty in the polarization measurement the polarization is changed by $\Delta P = \pm 1\,\%$. We obtain that at an energy of 500 GeV all measurements are dominated by the polarization error. This error is $5 - 10$ times greater than the statistical error. At the higher energy the behavior is more mixed. Some couplings are almost not affected by the polarization error but others are. This is more pronounced in the case of electron and positron polarization. From this observations a polarization error of $\Delta P = 0.1 - 0.2\,\%$ is needed for a measurement which is not dominated by this polarization error. This translate into the following relative errors for electron polarization $\Delta\mathcal{P}^-/\mathcal{P}^- = 0.1 - 0.2\,\%$ and positron polarization $\Delta\mathcal{P}^+/\mathcal{P}^+ = 0.2 - 0.3\,\%$. One sees from Table 2.11 that the simulated results are in the same range as before.

	Δg_1^Z	$\Delta\kappa_\gamma$	λ_γ	$\Delta\kappa_Z$	λ_Z	g_4^Z	g_5^Z	$\tilde{\kappa}_Z$	$\tilde{\lambda}_Z$
500 GeV	38.1	4.8	12.1	8.7	11.5	85.8	27.7	64.9	11.4
800 GeV	39.0	2.6	5.2	4.9	5.1	41.8	28.5	29.6	4.9

	Δg_1^Z	$\Delta\kappa_\gamma$	λ_γ	$\Delta\kappa_Z$	λ_Z	g_4^Z	g_5^Z	$\tilde{\kappa}_Z$	$\tilde{\lambda}_Z$
500 GeV	24.8	4.1	8.2	5.0	8.9	79.9	22.8	50.6	10.3
800 GeV	21.9	2.2	5.0	2.9	4.7	31.8	24.3	24.1	4.4

	Δg_1^Z	$\Delta\kappa_\gamma$	λ_γ	$\Delta\kappa_Z$	λ_Z	g_4^Z	g_5^Z	$\tilde{\kappa}_Z$	$\tilde{\lambda}_Z$
500 GeV	15.5	3.3	5.9	3.2	6.7	45.9	16.5	39.0	7.5
800 GeV	12.6	1.9	3.3	1.9	3.0	18.3	14.4	14.3	3.0

Table 2.11: Expected sensitivity ($\times 10^{-4}$) for different couplings at a center-of-mass energy of 500 and 800 GeV and a luminosity of $500\,\mathrm{fb}^{-1}$ and $1000\,\mathrm{fb}^{-1}$. In the case of polarized beams the luminosity is split up equally on both combinations.

2.5.2 Use of transversely polarised beams for TGC's

In [106] it has been pointed out that the use of transversely polarised beams may be an important tool for studying TGC and longitudinal W_L, in particular for measuring relative phases of the helicity amplitudes in WW production.

In [79] TGC were studied with optimal observables using transversely polarised beams, see Table 2.9. If both beams have transverse polarisation, the errors on most couplings are approximately of the same size as in the situation where only the e^- beam has longitudinal polarisation. This resuls is confirmed by [78], where a first true simulation was done for studying TGC's in WW production and semileptonic decay with transversely polarised beams for the TESLA design using $\sqrt{s} = 500$ GeV, $\mathcal{L} = 500$ fb^{-1} and $|P_{e^-}| = 80\%$, $|P_{e^+}| = 60\%$ and including also ISR and beamstrahlung. For this simulation the program WHIZARD has been used. However, for one interesting coupling combination the use of transversely polarised beams is useful. The errors for $\mathrm{Re}\,\lambda_\gamma$, $\mathrm{Re}\,\lambda_Z$, $\mathrm{Re}\,\tilde{\lambda}_\gamma$ and $\mathrm{Re}\,\tilde{\lambda}_Z$ are they smaller with transversely polarised beams, viz. they are of the same size as with both beams longitudinally polarised. This is true for both energies.

If electron as well as positron polarisation is available we thus conclude that, regarding the 1σ-standard deviations on the TGCs (without assuming any coupling to be zero) *longitudinal* polarisation is the preferable choice, apart from one exception (see below). Note that we are better with longitudinal polarisation also for all CP violating couplings.

It has been shown in [73] that $\tilde{h}_+$ is not measurable from the normalised event distribution, neither with unpolarised beams nor with longitudinal polarisation. One can however measure this coupling with *transverse* beam polarisation with good sensitivity. In the γ-Z-parameterisation this means that the four couplings $\mathrm{Im}\, g_1^\gamma$, $\mathrm{Im}\, g_1^Z$, $\mathrm{Im}\, \kappa_\gamma$ and $\mathrm{Im}\, \kappa_Z$ are not simultaneously measurable without transverse polarisation.

Although for most couplings longitudinal polarisation of both beams is the advantageous choice, measurement of the full parameter space requires to spend part of the total luminosity of the collider on the transverse polarisation mode.

2.5.3 CP Violation in Jet Decays of the Z Boson at GigaZ

An interesting topic is the test of the CP symmetry in Z decays. Here a flavor-diagonal Z decay where CP-violating effects within the Standard Model (SM) are estimated to be very small [83] is studied. Thus, looking for CP violation in such Z decays means looking for new physics beyond the SM. Of particular interest are Z decays involving heavy leptons or quarks. Thus, the process Z $\rightarrow b\bar{b}G$, which is sensitive to effective CP-violating couplings in the $Zb\bar{b}G$ vertex, has been analysed theoretically in [84] and experimentally in [85]. No significant deviation from the SM has been found.

If CP-violating couplings are introduced in the $Zb\bar{b}G$ vertex, they will, because of gauge invariance of QCD, appear in the $Zb\bar{b}GG$ vertex as well. But the $Zb\bar{b}GG$ vertex could in principle contain new coupling parameters. The analysis of the 4 jet decays of the Z boson involving b quarks looks into both, 4- and 5-point vertices. This has been investigated theoretically in [86] and experimentally in [87]. Also in this case no significant deviation from the SM has been found.

In the GigaZ scenario [88, 110], these measurements which were performed at the electron-positron collider experiments at LEP could be redone with increased precision. In the following, the results of the calculations of the processes Z $\rightarrow$ 3 jets and Z $\rightarrow$ 4 jets including CP-violating couplings, with at least two of the jets originating from a b or $\bar{b}$ quark, for the GigaZ scenario assuming longitudinal beam polarization for electrons and positrons [89] are reviewed. All details of the calculation for unpolarized e^+, e^- beams can be found in [84, 86].

For a model independent study of CP violation in 3 jet and 4 jet decays of the Z boson the effective Lagrangian approach as explained in [83] can be used. One could add to the SM Lagrangian $\mathcal{L}_{SM}$ a CP-violating term $\mathcal{L}_{CP}$

$$\mathcal{L}_{CP}(x) = [\, h_{Vb}\, \bar{b}(x)\, T^a\, \gamma^\nu\, b(x) + h_{Ab}\, \bar{b}(x)\, T^a\, \gamma^\nu\, \gamma_5\, b(x)\,]\; Z^\mu(x)\, G^a_{\mu\nu}(x) \quad , \tag{31}$$

where $b(x)$ denotes the b quark field, $Z^\mu(x)$ and $G^a_{\mu\nu}(x)$ represent the field of the Z boson and the field strength tensor of the gluon, respectively, and $T^a = \lambda^a/2$ are the generators of $SU(3)_C$. In (31) h_{Vb} and h_{Ab} are real CP-violating vector and axial vector chirality conserving coupling constants. Dimensionless coupling constants $\widehat{h}_{Vb,Ab}$ using the Z mass as the scale parameter can be defined by $h_{Vb,Ab} = \frac{e\, g_s}{\sin\vartheta_W\, \cos\vartheta_W\, m_Z^2}\; \widehat{h}_{Vb,Ab}$.

Chirality conserving CP-violating interactions as introduced (31) can arise at one loop level in multi-Higgs extensions of the Standard Model [90]. They can also possibly be generated in models with excited quarks which is further investigated here. Excitations of quarks would be natural in a scenario where quarks have substructure and participate in a new type of strong interaction. This type of models and effects from excited quarks at hadron colliders have for instance been discussed in [91]. In particular, here it is assumed that b quarks have excited partners b' of spin $\frac{1}{2}$ and mass $m_{b'}$. Due to higher order dimensional operators in composite models chirality-conserving $Zb'b$ couplings at the scale of GigaZ energies are a priori possible (see e.g. [92]). Because of colour gauge invariance the $b'bG$ couplings can be expected to be chirality-flipping dipole couplings. Then, couplings $\widehat{h}_{Vb,Ab}$ as introduced in (31) can be generated by the following effective interactions of b' and b quarks, Z bosons and gluons:

$$\mathcal{L}'(x) = \; - \; \frac{e}{2\, \sin\vartheta_W\, \cos\vartheta_W}\, Z_\mu(x)\, \bar{b}'(x)\, \gamma^\mu\, (g'_V - g'_A\gamma_5)\, b(x)$$

$$- \; i \, \frac{g_s}{2m_{b'}} \, \hat{d}_c \, \bar{b}'(x) \, \sigma^{\mu\nu} \, \gamma_5 \, T^a \, b(x) \, G^a_{\mu\nu}(x) + \text{h.c.} \tag{32}$$

Here g'_V, g'_A and $\hat{d}_c$ are complex parameters, which can be expected to be of order one if the underlying dynamics is strongly interacting. In this model for $m_{b'} \gg m_Z$ one derives for the couplings [90] $\widehat{h}_{Vb} = \frac{m_Z^2}{m_{b'}^2} \, \mathrm{Re}(\hat{d}_c \, g'^*_A)$ and $\widehat{h}_{Ab} = -\frac{m_Z^2}{m_{b'}^2} \, \mathrm{Re}(\hat{d}_c \, g'^*_V)$

In this study it is assumed that one is able to flavor-tag the b quarks and to measure their momenta. This is justified due to the extremely good b-tagging capabilities foreseen at TESLA [110]. Then, the CP-violating couplings are analysed using CP-odd observables constructed from the momentum directions of the b and $\bar{b}$ quarks, $\widehat{\mathbf{k}}_b = \mathbf{k}_b/|\mathbf{k}_b|$ and $\widehat{\mathbf{k}}_{\bar{b}} = \mathbf{k}_{\bar{b}}/|\mathbf{k}_{\bar{b}}|$ (see [83,84]):

$$T_{33} = (\widehat{\mathbf{k}}_{\bar{b}} - \widehat{\mathbf{k}}_b)_3 \, (\widehat{\mathbf{k}}_{\bar{b}} \times \widehat{\mathbf{k}}_b)_3 \; , \tag{33}$$

$$V_i = (\widehat{\mathbf{k}}_{\bar{b}} \times \widehat{\mathbf{k}}_b)_3 \; . \tag{34}$$

The observable T_{33} transforms as tensor component, V_3 as vector component.

The expectation values of the observables (33), (34) have been calculated for different JADE cuts, as function of $\widehat{h}_b = \widehat{h}_{Ab} g_{Vb} - \widehat{h}_{Vb} g_{Ab}$ and $\widetilde{h}_b = \widehat{h}_{Vb} g_{Vb} - \widehat{h}_{Ab} g_{Ab}$.

For unpolarised e^+e^- beams a non-zero value $<\mathcal{O}> \neq 0$ for one of the CP-odd observables above is an unambiguous indicator of CP violation. For longitudinally polarised beams this holds if possible chirality flipping interactions at the e^+e^-Z vertex — which do not exist in the SM — are neglected. In very good approximation, it was found for Z $\rightarrow$ 3 jets and Z $\rightarrow$ 4 jets that the tensor observables are only sensitive to $\widehat{h}_b$ and the vector observables only to $\widetilde{h}_b$ [84,86].

Numerical results

The sensitivities $1/\delta\widehat{h}_b$, $1/\delta\widetilde{h}_b$ to $\widehat{h}_b$, $\widetilde{h}_b$ for the tensor (33), vector (34) observables have been calculated varying the jet resolution parameter y_{cut}. A total number of $N_{tot} = 10^9$ Z decays for unpolarized beams was assumed, following the GigaZ scenario [88,110]. A measurement of $\widehat{h}_b$, $\widetilde{h}_b$ has to produce a mean value larger than $\delta\widehat{h}_b$, $\delta\widetilde{h}_b$ to be able to claim a non-zero effect at the 1 s. d. level. Comparing with optimal observables it was found for unpolarized beams [84,86] that these simple observables (33,34) reach nearly optimal sensitivities. Therefore optimal observables are not considered in the following.

The inverse sensitivities $\widehat{h}_b$, $\widetilde{h}_b$ are shown in Fig. 21 (left) for Z $\rightarrow$ 3 jets for different longitudinal beam polarizations. The results for Z $\rightarrow$ 4 jets can be found in [89]. The sensitivity decreases with increasing y_{cut} for all observables due to the decrease in number of events available.

Because the expectation value of the tensor observable does not depend on longitudinal polarization, the differences in $\delta\widehat{h}_b$ for different polarization choices reflect only the change in statistics. For $P_+ = 0.6$ and $P_- = -0.8$ the enhancement of the Z production rate is largest. The differences in $\delta\widetilde{h}_b$ reflect both the change in statistics and the modification of the expectation value due to polarization. For $P_+ = 0.6$ and $P_- = -0.8$ the sensitivity increases by more than a factor of six compared to unpolarized beams. A convenient choice of the polarizations can even lead to a better sensitivity of the vector observable to $\widetilde{h}_b$ than of the tensor observable to $\widehat{h}_b$. The improvement in sensitivity due to positron polarization in addition to electron polarization is relative small.

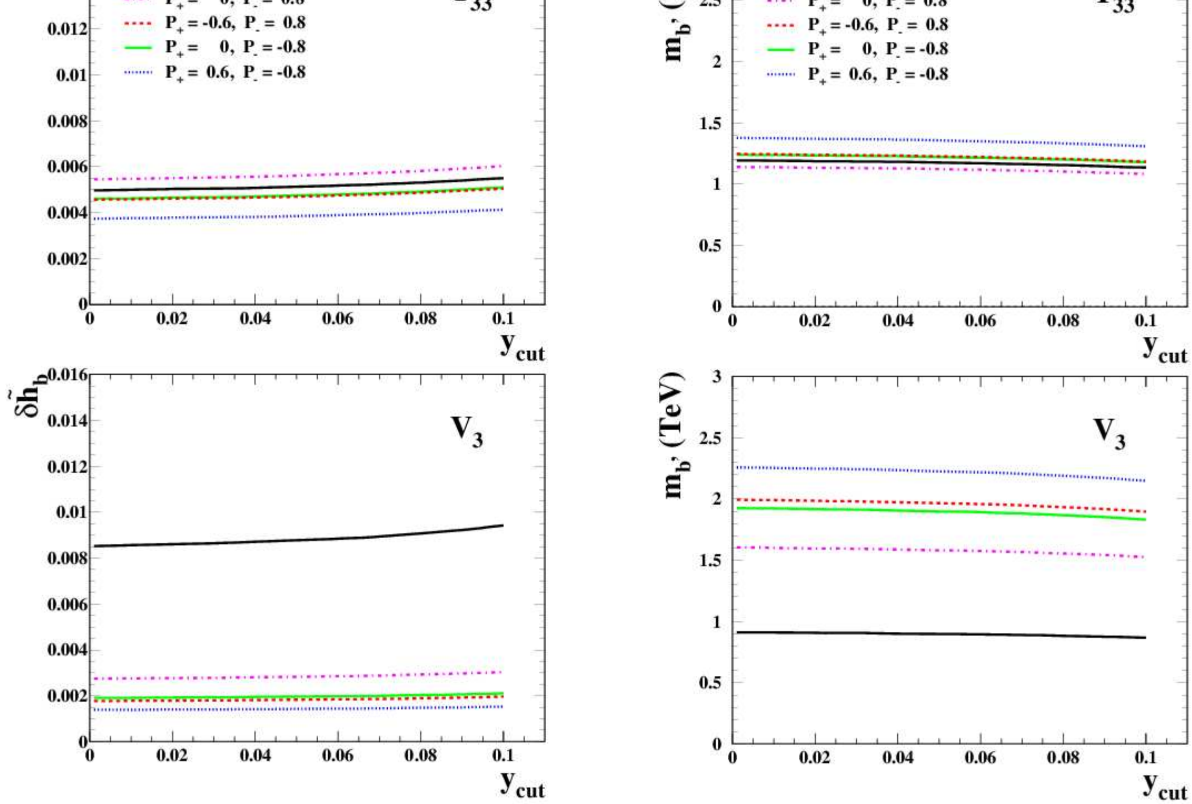

Figure 21: Left: The inverse sensitivities of tensor T_{33} and vector V_3 observables to $\widehat{h}_b$ and $\widetilde{h}_b$. Right: Lower limits on the excited quark mass $m_{b'}$ at the 1 s. d. level which can be derived from a measurement of those observables (couplings for the b' as discussed in the text are assumed). The results for Z $\to$ 3 jets are shown as function of the jet resolution parameter y_{cut} for different longitudinal polarizations of the e^+ and e^- beams.

If a measurement of $\widehat{h}_b$, $\widetilde{h}_b$ produces a mean value lower than $\delta\widehat{h}_b$, $\delta\widetilde{h}_b$ a non-zero effect at the 1 s. d. level cannot be claimed and therefore an upper limit on these couplings can be derived. As discussed above this can be translated into lower bounds on the excited quark mass $m_{b'}$. Assuming $\mathrm{Re}(\hat{d}_c\ g_A'^*) = \mathrm{Re}(\hat{d}_c\ g_V'^*) = 1$ these bounds are shown in Fig. 21 (right) for Z $\to$ 3 jets for different longitudinal beam polarizations. The results for Z $\to$ 4 jets can be found in [89].

Conclusions

If flavor tagging of b and $\bar{b}$ jets is available then, with a total number of 10^9 Z decays and choosing a cut parameter* $y_{cut} = 0.02$, the anomalous coupling constant $\widehat{h}_b$ can be determined with an accuracy of order 0.004 (Z $\to$ 3 jets) and 0.008 (Z $\to$ 4 jets) at 1 s. d. level using the tensor observable T_{33} (33) for the measurement. Here, $b-\bar{b}$ distinction is not necessary. These accuracies are close to the ones which already can be obtained with unpolarized beams. If in a measurement a non-zero effect at the 1 s. d. level is not observed excited quark masses $m_{b'}$ lower than 1.4 TeV (Z $\to$ 3 jets) and 0.94 TeV (Z $\to$ 4 jets) can be excluded if appropriate couplings are of a size characteristic of a strong interaction.

*This value of y_{cut} is, in fact, a relatively large number for a selection of events Z $\to$ 4 jets. So the numbers given in the following are conservative for this channel.

If $b - \bar{b}$ distinction is experimentally realizable, which should be the case at a future linear collider, the coupling constant $\widetilde{h}_b$ can be measured with an accuracy of order 0.0015 (Z $\rightarrow$ 3 jets) and 0.003 (Z $\rightarrow$ 4 jets) using the vector observable V_3 (34) and choosing $P_+ = 0.6$ and $P_- = -0.8$ as longitudinal polarizations of positron and electron, respectively. In case of a non-observation of an effect at the 1 s. d. level excited quark masses $m_{b'}$ lower than 2.2 TeV (Z $\rightarrow$ 3 jets) and 1.5 TeV (Z $\rightarrow$ 4 jets) can be excluded if the relevant couplings are of a size characteristic of a strong interaction.

Comparing 3 and 4 jet analyses [89] one finds that the sensitivity to the anomalous coupling $\widehat{h}_b$ is roughly constant as function of the cut parameter y_{cut} for $y_{cut} < 0.1$ in the 3 jet case. For the 4 jet case the sensitivity is found to increase as y_{cut} decreases. For $y_{cut} \approx 0.01$ the 4 jet sensitivity is found to become equal to that from 3 jets. Of course in an experimental analysis one should try to make both 3 and 4 jet analyses in order to extract the maximal possible information from the data.

In these theoretical investigations always 100% efficiencies are assumed and only the statistical errors are considered. Assuming systematic errors to be of the same size as the statistical ones, the accuracies in the determinations of $\widehat{h}_b$, $\widetilde{h}_b$ discussed above should indeed be better by more than one order of magnitude than those derived from LEP. As shown in [90] this will, for instance, give valuable information on the scalar sector in multi-Higgs extensions of the Standard Model. Moreover interesting information on models with excited quarks can be derived.

2.5.4 CP violation in $t\bar{t}$ production

Grzadkowski,Hioki,hep-ph/0004223
Rindani, hep-ph/0304046
Hinweis auch auf Ananthanarayan, CP violation in tau system

2.5.5 Searches for CP violation with transversely polarised beams

Overview

This is a précis of a recent preprint [70]. Transverse polarization (TP) enables novel CP violation search in the inclusive process $e^+e^- \to A + X$. When the spin of A is unobserved and m_e is neglected, only (pseudo-)scalar or tensor currents associated with a new-physics scale Λ can lead to CP-odd observables at leading order in the couplings from interference with γ and Z in the presence of TP.

In order to test CP violation, one needs more than the momenta of particles to be measured in $e^+e^- \to f\bar{f}$. The presence of TP provides such a vector, without observing final state polarization. This leads, e.g., to gain in statistics. CP violation due to beyond the standard model interactions may be parametrized in terms of contact interactions in a model independent manner. When m_e is neglected, with only TP interactions that transform as V and A cannot interfere at leading order in the new interactions with the standard model interactions to yield CP odd correlations, which can be inferred from general results of [71]. The tensor and (pseudo-)scalar interactions are accessible only at a higher order of perturbation theory without TP, even if longitudinal polarization is available.

In our application example we have evaluated the contributions to the differential cross-section due to (pseudo)-scalar and tensor contact interactions at leading order in the interaction strengths for the process $e^+e^- \to t\bar{t}$. This is used to construct an effective up-down asymmetry and a polar angle integrated version of the same. By assuming that the coefficients of the effective interaction that is suppressed by the second power of the new-physics scale Λ, to be of order unity, we show that at $\sqrt{s} = 500$ GeV and with an integrated luminosity $\int dt\mathcal{L} = 500\,\mathrm{fb}^{-1}$, we find that at the 90% confidence level, the scale Λ can be bounded at about 10 TeV, with perfect TP.

Theoretical framework

The Lagrangian we will use for our calculations is:

$$\mathcal{L} = \mathcal{L}^{SM} + \frac{1}{\Lambda^2}\sum_i (\, \alpha_i \mathcal{O}_i + \text{h.c.}\,), \tag{35}$$

where α_i are the coefficients which parameterize non-standard interactions, $\mathcal{O}_i$ are the effective dimension-six operators, and Λ is the scale of new physics.

After Fierz transformation the part of lagrangian containing the above four-Fermi operators can be rewritten as

$$\mathcal{L}^{4F} = \sum_{i,j=L,R}\Big[\, S_{ij}(\bar{e}P_i e)(\bar{t}P_j t) + V_{ij}(\bar{e}\gamma_\mu P_i e)(\bar{t}\gamma^\mu P_j t) + T_{ij}(\bar{e}\frac{\sigma_{\mu\nu}}{\sqrt{2}}P_i e)(\bar{t}\frac{\sigma^{\mu\nu}}{\sqrt{2}}P_j t)\,\Big], \tag{36}$$

where

$$S_{RR} = S^*_{LL}, \quad S_{LR} = S_{RL} = 0, \quad \text{and} \quad V_{ij} = V^*_{ij}, \quad \text{and} \quad T_{RR} = T^*_{LL}, \quad T_{LR} = T_{RL} = 0.$$

The z axis is chosen along the direction of the e^-. The differential cross sections for $e^+e^- \to t\bar{t}$, with the superscripts denoting the respective signs of the e^- and e^+ TP, are

$$\frac{d\sigma^{\pm\pm}}{d\Omega} = \frac{d\sigma^{\pm\pm}_{SM}}{d\Omega} \mp \frac{3\alpha\beta^2}{4\pi}\frac{m_t\sqrt{s}}{s-m_Z^2}\left(c^t_V c^e_A \mathrm{Re}S\right)\sin\theta\cos\phi, \tag{37}$$

$$\frac{d\sigma^{\pm\mp}}{d\Omega} = \frac{d\sigma^{\pm\mp}_{SM}}{d\Omega} \pm \frac{3\alpha\beta^2}{4\pi}\frac{m_t\sqrt{s}}{s-m_Z^2}\left(c_V^t c_A^e \mathrm{Im}S\right)\sin\theta\sin\phi, \tag{38}$$

where

$$\begin{aligned}
\frac{d\sigma^{+\pm}_{SM}}{d\Omega} \quad = \quad & \frac{d\sigma^{-\mp}_{SM}}{d\Omega} = \frac{3\alpha^2\beta}{4s}\left[\frac{4}{9}\left\{1+\cos^2\theta+\frac{4m_t^2}{s}\sin^2\theta \pm \beta^2\sin^2\theta\cos 2\phi\right\}\right. \\
& - \frac{s}{s-m_Z^2}\frac{4}{3}\left\{c_V^e c_V^t(1+\cos^2\theta + \frac{4m_t^2}{s}\sin^2\theta \pm \beta^2\sin^2\theta\cos 2\phi)\right. \\
& \left. + \ 2\, c_A^e c_A^t \beta\cos\theta\right\} + \frac{s^2}{(s-m_Z^2)^2}\left\{(c_V^{e\,2}+c_A^{e\,2})\right. \\
& \times\left[(c_V^{t\,2}+c_A^{t\,2})\beta^2(1+\cos^2\theta) + c_V^{t\,2}\frac{8m_t^2}{s}\right] + 8c_V^e c_A^e c_V^t c_A^t\beta\cos\theta \\
& \left.\left. \pm \ (c_V^{e\,2}-c_A^{e\,2})(c_V^{t\,2}+c_A^{t\,2})\beta^2\sin^2\theta\cos 2\phi\right\}\right]
\end{aligned} \tag{39}$$

The quantities $\sin\theta\sin\Phi$ and $\sin\theta\cos\Phi$ are CP-odd and CP-even. Here $\beta = \sqrt{1-4m_t^2/s}$, and we have defined

$$S \equiv S_{RR} + \frac{2c_A^t c_V^e}{c_V^t c_A^e}T_{RR}, \tag{40}$$

where c_V^i, c_A^i are the couplings of Z to e^-e^+ and $t\bar{t}$, and where we have retained the new couplings to linear order only. In (40) the contribution of the tensor term relative to the scalar term is suppressed by a factor $2c_A^t c_V^e/c_V^t c_A^e \approx 0.36$. In what follows, we will consider only the combination S, and not S_{RR} and T_{RR} separately.

CP-odd asymmetries and numerical results

We construct the CP-odd asymmetry, which we call the up-down asymmetry as

$$A(\theta) = \frac{\displaystyle\int_0^\pi \frac{d\sigma^{+-}}{d\Omega}d\phi - \int_\pi^{2\pi}\frac{d\sigma^{+-}}{d\Omega}d\phi}{\displaystyle\int_0^\pi \frac{d\sigma^{+-}}{d\Omega}d\phi + \int_\pi^{2\pi}\frac{d\sigma^{+-}}{d\Omega}d\phi} \tag{41}$$

and also the θ-integrated version,

$$A(\theta_0) = \frac{\displaystyle\int_{-\cos\theta_0}^{\cos\theta_0}\int_0^\pi \frac{d\sigma^{+-}}{d\Omega}d\cos\theta d\phi - \int_{-\cos\theta_0}^{\cos\theta_0}\int_\pi^{2\pi}\frac{d\sigma^{+-}}{d\Omega}d\cos\theta d\phi}{\displaystyle\int_{-\cos\theta_0}^{\cos\theta_0}\int_0^\pi \frac{d\sigma^{+-}}{d\Omega}d\cos\theta d\phi + \int_{-\cos\theta_0}^{\cos\theta_0}\int_\pi^{2\pi}\frac{d\sigma^{+-}}{d\Omega}d\cos\theta d\phi} \tag{42}$$

In the latter, a cut-off θ_0 angle has been introduced.

In a numerical study we put limits on the parameters using the integrated asymmetry $A(\theta_0)$. The figures are presented for $\sqrt{s} = 500$ GeV and the ideal condition of 100% beam polarizations for e^- as well as e^+. We will comment later on about the result for more realistic polarizations. As we can see from Fig. 22, the value of $A(\theta_0)$ increases with the cut-off, because the SM cross section in the denominator of eq. (42) decreases with cut-off faster than the numerator.

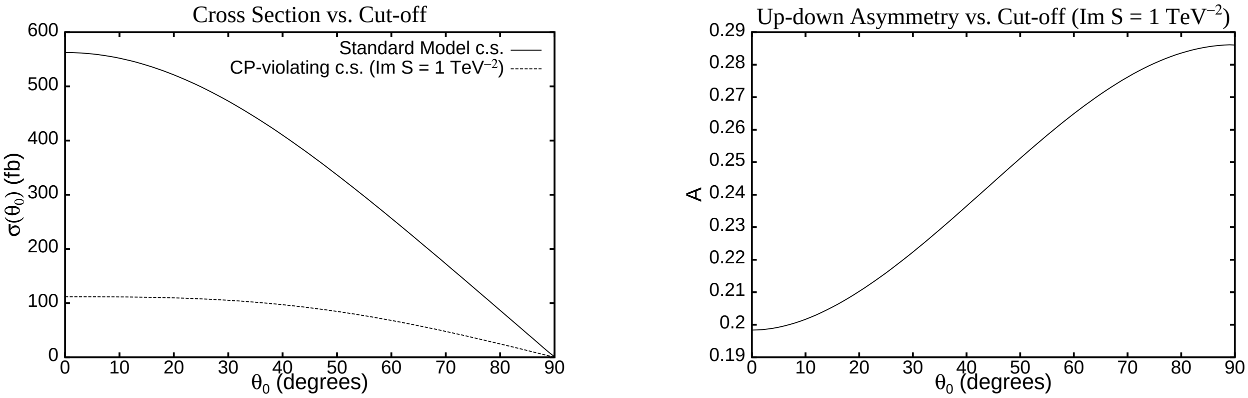

Figure 22: Left:The SM cross section (solid line) and the numerator of the asymmetry $A(\theta)$ in eq. (41) (broken line) as for the quantities integrated over θ with a cutoff θ_0, plotted as a function of θ_0; Right: The asymmetry $A(\theta_0)$ defined in eq. (42) plotted as a function of θ_0 for Im $S = 1$ TeV^{-2}.

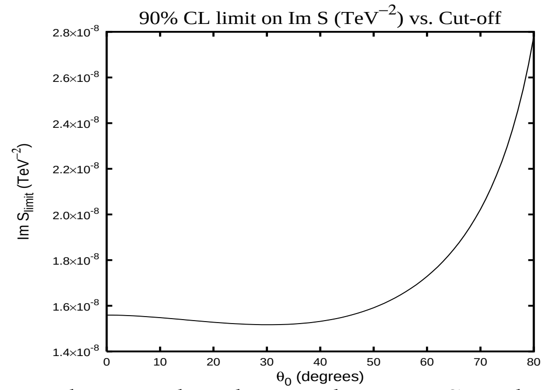

Figure 23: The 90% C.L. limit that can be obtained on Im S with an integrated luminosity of 500 fb^{-1} plotted as a function of the cut-off angle θ_0.

Fig. 23 shows the 90% confidence level (C.L.) limits that could be placed on $\mathrm{Im}S$ for an integrated luminosity of $L = 500$ fb^{-1}. The limit is the value of Im S which would give rise to an asymmetry $A_{\text{lim}} = 1.64/\sqrt{L\Delta\sigma}$, where $\Delta\sigma$ is the SM cross section. This limit translates to a value of Λ of the order of 8 TeV, assuming that the coefficients α_i in (35) are of order 1. The corresponding limit for $\sqrt{s}$ of 800 GeV with the same integrated luminosity is ~ 9.5 TeV.

Using realistic polarisation degrees of 80% and 60% for TP, the up-down asymmetry $A(\theta)$ or $A(\theta_0)$ gets multiplied by a factor $\frac{1}{2}(P_1 - P_2)$ for e^- and e^+ beams respectively. For $P_1 = 0.8$ and $P_2 = -0.6$, this means a reduction of the asymmetry by a factor of 0.7. Since the SM cross section does not change, this also means that the limit on the parameter Im S goes up by a factor of $1/0.7 \approx 1.4$, and the limit on Λ goes down by a factor of $\sqrt{0.7} \approx 0.84$, to about 6.7 TeV. If the positron beam is unpolarized, however, the sensitivity goes down further.

In summary, TP can be used to study CP-violating asymmetry arising from the interference of new-physics scalar and tensor interactions with the SM interactions. These interference terms cannot be seen with longitudinally polarized or unpolarized beams. Moreover, such an asymmetry would not be sensitive to new vector and axial-vector interactions (as for example, from an extra Z' neutral boson), or even electric or "weak" dipole interactions of heavy particles, since the asymmetry vanishes if $m_e \sim 0$.

2.6 Precision measurements of the electroweak theory at GigaZ

2.6.1 Measurement of $\sin^2\theta_{eff}$ – Application of the Blondel Scheme

The option GigaZ refers to running the LC at the Z resonance with to about 10^9 Z events and makes possible the most sensitive test of the SM ever made.

In the SM the left–right asymmetry A_{LR} depends only on the effective leptonic weak mixing angle:

$$A_{LR} = \frac{2(1-4\sin^2\Theta^l_{eff})}{1+(1-4\sin^2\Theta^l_{eff})^2}. \tag{43}$$

The statistical power of the data sample can be fully exploited only when $\delta(A_{LR}(pol)) < \delta(A_{LR}(stat))$. For $10^8 - 10^9$ Z's this occurs when $\delta(P_{eff}) < 0.1\%$. In this limit $\delta(\sin^2\theta_{eff}) \sim 10^{-5}$, which is an order–of–magnitude smaller than the present value of this error. Thus it will be crucial to minimize the error in the determination of the polarization. Although the improvements in Compton polarimetry achieving a precision $< 0.1\%$ may be difficult. The desired precision should, nevertheless, be attainable with the Blondel Scheme, where it is not necessary to know the beam polarization with such extreme accuracy, since A_{LR} can be directly expressed via cross sections for producing Z's with longitudinally polarized beams:

$$\begin{aligned} \sigma &= \sigma_{unpol}[1 - P_{e^-}P_{e^+} + A_{LR}(P_{e^+} - P_{e^-})], & (44)\\ A_{LR} &= \sqrt{\frac{(\sigma^{RR}+\sigma^{RL}-\sigma^{LR}-\sigma^{LL})(-\sigma^{RR}+\sigma^{RL}-\sigma^{LR}+\sigma^{LL})}{(\sigma^{RR}+\sigma^{RL}+\sigma^{LR}+\sigma^{LL})(-\sigma^{RR}+\sigma^{RL}+\sigma^{LR}-\sigma^{LL})}}. & (45)\end{aligned}$$

In this formula the absolute polarisation values of the left- and the right-handed states are assumed to be the same. Corrections have to be determined experimentally by means of polarimetry techniques; however, only relative measurements are needed, so that the absolute calibration of the polarimeter cancels [4].

As can be seen from (45) the Blondel scheme also requires some luminosity for the less favoured combinations (LL, RR). However only about 10% of running time will be needed for these combinations to reach the desired accuracy for these high precision measurements. Fig. 24 shows the statistical error on A_{LR} as a function of the positron polarisation for $P_{e^-} = 80\%$. Already with 20% positron polarisation the goal of $\delta\sin^2\theta_{eff} \sim 10^{-5}$ can be reached. The comparison of different beam polarisation configurations and the gain for the A_{LR} Measurements see also [5].

As an example of the potential of the GigaZ $sin^2\theta_{eff}$ measurement Fig. 25 compares the present experimental accuracy on $sin^2\theta_{eff}$ and M_W from LEP/SLD/Tevatron and the prospective accuracy from the LHC and from a LC without GigaZ option with the predictions of the SM and the MSSM. With GigaZ a very sensitive test of the theory will be possible.

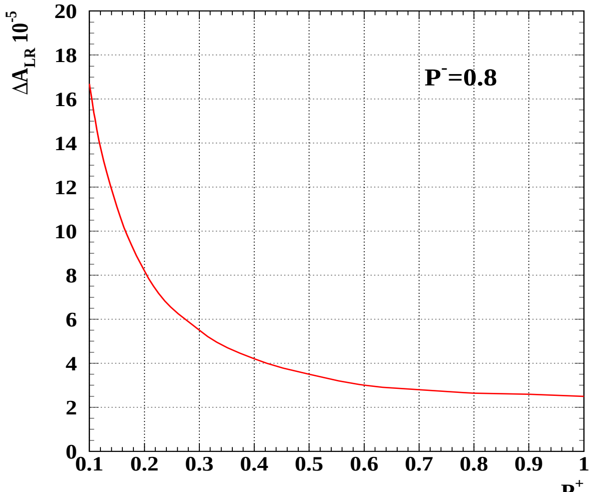

Figure 24: Test of Electroweak Theory: The statistical error on the left–right asymmetry A_{LR} of $e^+e^- \to Z \to \ell\bar{\ell}$ at GigaZ as a function of the positron polarization $P(e^+)$ for fixed electron polarization $P_{e^-} = \pm 80\%$ [4].

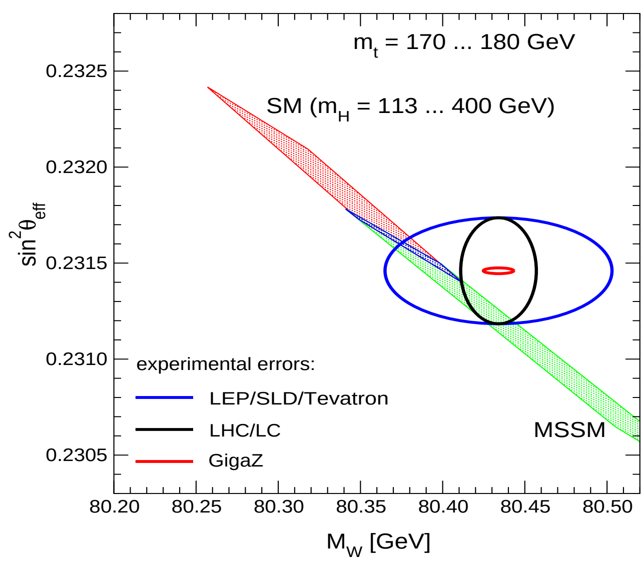

Figure 25: Test of Electroweak Theory: A high-precision measurement at GigaZ of the left–right asymmetry A_{LR} and consequently of $\sin^2\Theta^l_{eff}$ allows to test the electroweak theory at an unprecedented level. The allowed parameter space of the SM and the MSSM in the $\sin^2\Theta^l_{eff}$–M_W plane is shown together with the experimental accuracy reachable at GigaZ. For comparison, the present experimental accuracy (LEP/SLD/Tevatron) and the prospective accuracy at the LHC and a LC without GigaZ option (LHC/LC) are also shown [6,7].

2.6.2 Higgsmass versus electroweak mixing angle

The precise measurement of the effective leptonic weak mixing angle at the Z-boson resonance, $\sin^2\theta_{\rm eff}$, at GigaZ will allow a very sensitive test of the electroweak theory [7]. With both beams polarized, i.e. 80% polarization for electrons and 60% polarization for positrons, an accuracy of $\Delta\sin^2\theta_{\rm eff} = \pm 1.3\times 10^{-5}$ can be achieved [8]. If only electron polarization were available, this would result in an accuracy of only about $\Delta\sin^2\theta_{\rm eff} = \pm 9.5\times 10^{-5}$ [9].

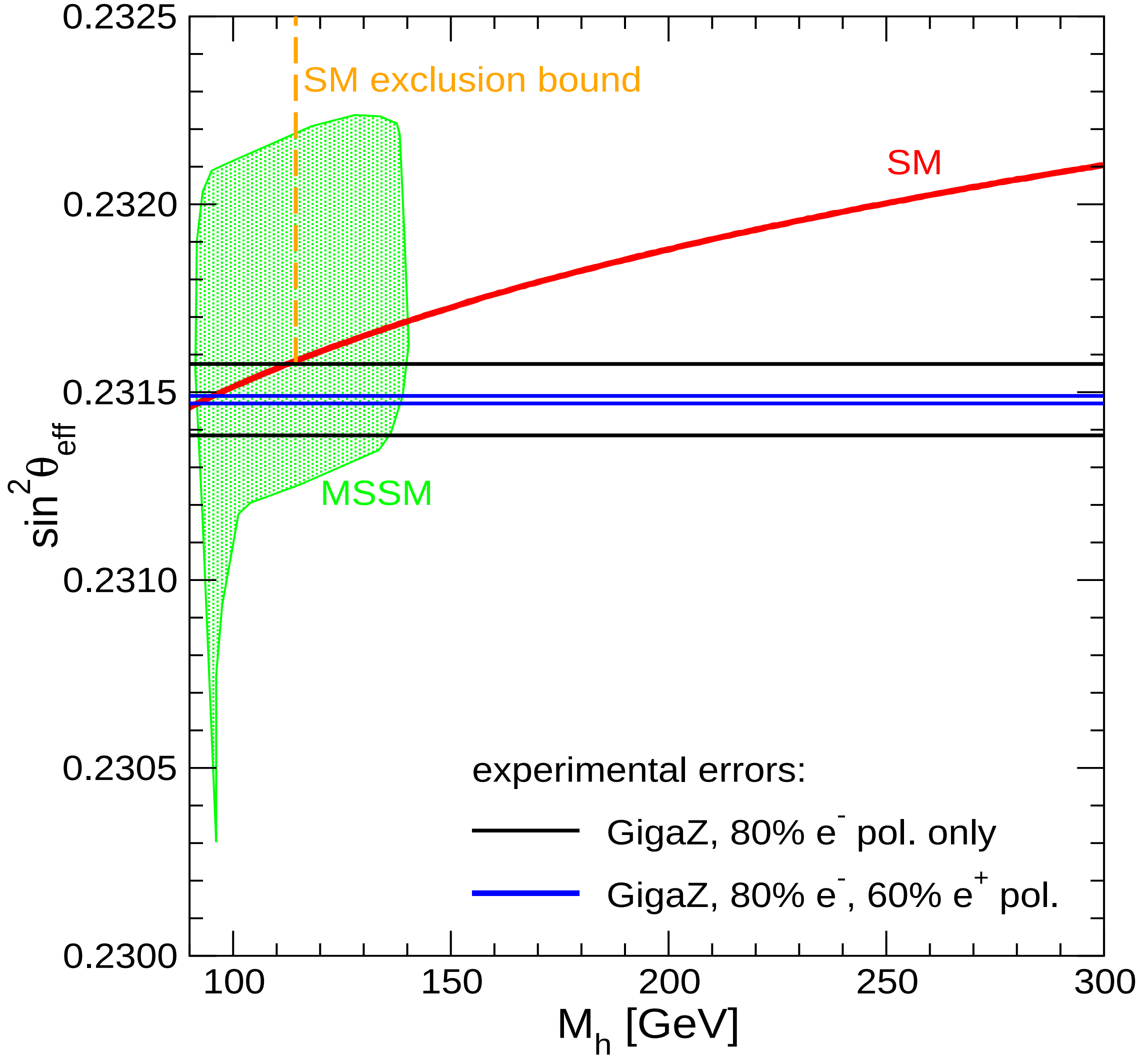

Figure 26: The predictions for $\sin^2\theta_{\rm eff}$ in the SM and the MSSM as a function of M_h, which corresponds to the Higgs-boson mass in the SM and the mass of the lightest $\mathcal{CP}$-even Higgs boson in the MSSM. The exclusion bound on the SM Higgs mass of $M_h > 114.4$ GeV [10] is indicated in the plot. The SM prediction is given for $m_t = 175 \pm 0.1$ GeV, while in the MSSM the SUSY parameters have been scanned. The theory predictions are compared with the experimental accuracies obtainable at GigaZ with an 80% polarized electron beam only and with the case of simultaneous polarization of both beams.

The impact of the more precise measurement for testing the electroweak theory is indicated in Fig. 26, where the experimental accuracy (using the current experimental central value of $\sin^2\theta_{\rm eff}$ [11]) is compared with the predictions in the SM and the MSSM. The theoretical predictions are shown as a function of M_h, which corresponds to the Higgs-boson mass in the SM and the mass of the lightest $\mathcal{CP}$-even Higgs boson in the MSSM. In the region where both models overlap, $M_h \lesssim 135$ GeV [12], the SM prediction corresponds to the MSSM result in the limit where all SUSY partners are heavy. The area corresponding to the MSSM prediction was obtained by varying all relevant SUSY parameters independently, taking into account the constraints from the direct search for SUSY particles and the LEP Higgs search. The MSSM predictions are based on the results described in Ref. [13], and the Higgs mass predictions have been obtained with *FeynHiggs2.0* [14].

Within the SM, the precision in $\sin^2\theta_{\rm eff}$ achievable with both beams polarized constrains the Higgs-boson mass to an interval of few GeV (neglecting the uncertainties from unknown higher-order corrections), while the precision corresponding to electron polarization leaves an uncertainty of about ± 25 GeV in M_h. Within the MSSM the parameter space in the M_h–$\sin^2\theta_{\rm eff}$ plane is reduced by about a factor 7 with the $\sin^2\theta_{\rm eff}$ measurement based on simultaneous polarization of both beams as compared to the case with electron polarization only. This puts sensitive constraints on the possible values of the underlying SUSY parameters. Combined with direct information on the SUSY spectrum the precise measurement of $\sin^2\theta_{\rm eff}$ will allow a very stringent consistency test of the MSSM.

2.7 Tools: Monte Carlo Event Generators and Beam Polarization

The use of numerical programs based on Monte Carlo (MC) techniques has become essential in performing any detailed experimental analysis in collider physics. In this section we will briefly recall the key features of these programs and discuss the inclusion of beam polarization effects. We will limit ourselves to the so-called event generators. These programs must be interfaced to both detector simulations and beam energy spectra to give a complete picture of the actual physics process.

In general the MC event generation process can be split into a number of phases.

- The hard process where the particles in the hard collision and their momenta are generated, usually according to the leading-order scattering matrix element (ME).
- The parton-shower (PS) phase where the coloured particles in the event are perturbatively evolved from the hard scale of the collision to the infrared cut-off. The emission of electromagnetic radiation from charged particles can be handled in a similar way.
- Those particles which decay before hadronization, *e.g.* the top quark, are decayed usually according to a calculated branching ratio with a ME to give the momenta of the decay products. Any coloured particles produced in these decays are then evolved by the PS algorithm.
- A hadronization phase in which the partons left after the perturbative evolution are formed into the observed hadrons.

Most MC event generators fall into one of two classes: *general-purpose (or multi-purpose) event generators* which aim to perform the full simulation of the event starting with the initial-state collider beams, proceeding through the hard scattering process and finishing with the final-state hadrons; the second class of programs (hereafter, *parton-level event generators*) typically performs the hard scattering part of the simulation only, perhaps including decays, and relies on one of the general-purpose generators for the rest of the simulation.

During the LEP-era the experiments relied on the general-purpose event generators for the description of hadronic final states together with more accurate parton-level programs interfaced to the former ones for specific processes, *e.g.* two- and four-fermion production. At a future linear collider (LC), as one wishes to study final states with higher multiplicities, for example six or even eight particles, this mixed approach will become more important as these final states cannot be described by the general-purpose event generators.

2.7.1 General-purpose Event Generators

Historically the main general-purpose event generators have been HERWIG [114], ISAJET [115] and PYTHIA [116]. While the general philosophy of these programs is similar, they use different phenomenological models and approximations. In general, at least for $\mathrm{e^+e^-}$ collisions, the range of hard scattering processes implemented is very similar. All these generators have a wide range of Standard Model (SM) processes available, reactions predicted by the Minimal Supersymmetric Standard Model (MSSM) as well as various selections of channels from other models too (*e.g.* extra gauge-bosons).

The major differences between the programs are in the approximations used in the PS evolution and the hadronization stage. While ISAJET still adopts the original PS algorithm which only re-sums collinear logarithms, both HERWIG and PYTHIA include the effects of soft logarithms via either an angular-ordered PS in the case of HERWIG, or an angular veto in the case of PYTHIA. For the hadronization process HERWIG uses the cluster model, ISAJET the independent fragmentation model and PYTHIA the Lund string model.

There are also major differences between the generators in the treatment of spin correlation and polarization effects. Both ISAJET and HERWIG include longitudinal polarization effects in both SM and Supersymmetric (SUSY) production processes, while PYTHIA includes both longitudinal and transverse polarizations in many processes. Another important difference is in the treatment of the subsequent decay of any heavy particle produced in the hard process. While HERWIG includes the full correlations in any subsequent decays using the method described in [117] both ISAJET and PYTHIA only include these effects in some processes, *e.g.* W pair production. To extend the method used in [117] to include transverse polarization also in the HERWIG production stage is certainly possible.

While these codes will continue to be used in the near future a major programme is underway to produce a new generation of general-purpose event generators in C++. The main aim of it is to provide the tools needed for the Large Hadron Collider (LHC). However, these tools will be used also for the next generation of LCs. The only program currently available in C++ which is capable of generating physics results is SHERPA (based on the APACIC++ [118] PS). Work is however underway to rewrite both PYTHIA [119] and HERWIG [120] in C++. These programs should be available in the next few years and we expect them to be the major tools for event generator at a future LC. Given the new design and structure of these programs the treatment of both spin correlation and polarization effects should be much better than in the current FORTRAN programs. For example HERWIG++, should include full polarization and correlation effects in the perturbative phase of the event using the method of [117].

2.7.2 Parton-Level Event Generators

There are a large number of programs available which calculate an individual hard process, or some set of hard processes, and are interfaced to one of the general-purpose generators, most often PYTHIA, to perform the PS and hadronization. It is impossible to review all such programs here. As many of the two- [121] and four-fermion [122] generators were used by the LEP collaborations, we refer to the report of the LEP-II MC workshop for their detailed discussion. Some programs, *e.g.*, LUSIFER [123], SIXFAP [124], EETT6F [125] and SIXPHACT [126], have been written specifically for six fermion processes. Many of these codes use helicity amplitude techniques to calculate the MEs and therefore either already include polarization effects or could easily be modified to do so.

Given the vast physics programme of future LCs, it is likely that one will also regularly resort to programs which are capable of calculating and integrating the MEs for large numbers of final-state particles automatically. There are a number of such codes available.

– AMEGIC++ [127] makes use of helicity amplitude techniques to evaluate the ME together with efficient multi-channel phase space integration to calculate the cross section. This package is part of SHERPA.

– COMPHEP [128] is an automatic program for calculation of cross sections for processes with up to eight external particles†. It uses the traditional trace techniques to evaluate the ME together with a modified adaptive integrator to compute the cross section, so it is at present not suitable for studies intended to investigate polarization/spin effects. However, the conversion to the use of helicity amplitudes techniques is currently planned.

– GRACE [129] (with the accompanying packages BASES and SPRING) combines the calculation of MEs via helicity amplitude techniques with adaptive integration.

– HELAC/PHEGAS uses the approach of [130] which is based on the Dyson-Schwinger equation together with multi-channel integration [131] to calculate the cross section.

– MADGRAPH/MADEVENT [132] uses helicity amplitude techniques for the ME together with an efficient multi-channel phase space integrator to compute the cross section. These packages are based on the HELAS [133] subroutines.

– WHIZARD [134] is a multi-channel integration package which can use either COMPHEP, MADGRAPH or O'MEGA‡ [136] to calculate the MEs.

All of these codes apart from HELAC/PHEGAS§ are publicly available. In order to simulate events these programs need to be interfaced to the general-purpose event generators. Most use *ad hoc* interfaces to one of the major general-purpose event generators with the details varying from one package to another. Recently, generic (*i.e.*, program-independent) FORTRAN common blocks have been proposed for the transfer of event configurations from parton level programs to showering and hadronization event generators [137].

The implementation of polarization and correlation effects differs between these programs. In general, apart from COMPHEP (as noted), these programs are all based on helicity amplitude techniques at some point in the calculation and therefore the inclusion of both transverse and longitudinal beam polarization is possible even where it is not currently implemented.

2.7.3 SUSY

Polarization and spin correlation effects are particularly important in studying SUSY scenarios, in order to measure the fundamental parameters of the underlying model. Thus, it is worth commenting in more detail on the inclusion of these effects in SUSY processes (hereafter, we assume the particle content of the MSSM).

HERWIG, PYTHIA and ISAJET all include longitudinal polarization effects in SUSY production processes. There is also a parton-level program SUSYGEN [138], interfaced to PYTHIA, which includes these effects.

All these programs also differ in the inclusion of the correlations in the subsequent decays of the particles. While SUSYGEN includes these correlations using helicity amplitude techniques and HERWIG uses the method of [117], these effects are generally not included in either PYTHIA or ISAJET.

†COMPHEP can have up to six final-state particles for scattering processes and seven for decays.

‡O'MEGA uses the approach of [135] to evaluate the ME but does not include yet any QCD processes.

§Contact: papadopo@alice.nuclear.demokritos.gr.

Among the parton-level programs, at present only `COMPHEP` and `GRACE` include SUSY processes, although both `MADGRAPH` and `AMEGIC++` can be extended to add the additional interactions which are needed.

2.8 Summary of the Physics Cases

We agreed in the POWER meeting that we should provide a table (like table 1 in GMP, Steiner, hep-ph/0106155) summarising (also quantitatively) the effects of having $P(e^+)$ in addition to $P(e^-)$.

*** still under work ***

Chapter 3

Machine Issues

3.1 Polarised Electrons for Linear Colliders

The SLC established that reliable electron beams with a polarization at high energy approaching 80% can be provided over periods of years. However, the beam structures planned for future colliders present new demands, and in addition higher polarization is desirable. The prospect for meeting these needs is outlined below. The electron beam for JLC/NLC is required to have a 270 ns macropulse at the IP consisting of 192 micropulses spaced 1.4 ns apart. At the IP each micropulse should have a charge of 0.75×1010 e^-. If a conventional dc-biased polarized electron gun based on GaAs-type photocathodes is used, it is assumed the gun must produce 1.5×1010 e^- for each micropulse, or a total of 2.9×1012 e^- in a single macropulse, which is over an order of magnitude more charge than produced for SLC. The problem is that as the current density in the macropulse increases beyond the SLC level, a dynamic barrier due to photoexcited electrons temporarily trapped in surface states limits the charge that can be extracted from the cathode. A satisfactory solution has been found that works well for conventional dc-biased guns: a very high dopant density at the GaAs surface promotes the tunneling of holes to the surface where efficient recombination rapidly disposes of the trapped electrons. Using this technique, macropulses (no micropulse structure) with current densities in excess of JLC/NLC requirements have recently been demonstrated. Although the charge in a single micropulse for TESLA is roughly twice that of JLC/NLC, the spacing between micropulses is 337 ns, which precludes a surface charge limit problem.

Highly polarized electrons are obtained from GaAs (or its tertiary and quaternary analogues) by directing a circularly-polarized laser beam tuned to the band-gap edge to a thin (typically 100 nm), strained epilayer of p-doped GaAs. Only a small fraction of the photons are absorbed in the epilayer. Electrons with zero momentum are promoted from the valence band maximum (VBM) to the conduction band minimum (CBM) upon the absorption of laser photons. A biaxial compressive strain produced by a lattice mismatch with the substrate or by the quantum confinement associated with short-period superlattice structures breaks the degeneracy of the heavy-hole (hh) and light-hole (lh) bands at the VBM. Hh-lh separations of 80 meV are readily achieved, which in carefully grown structures is sufficient to allow the selection of electrons from the hh band only. Because of angular momentum selection rules, this results in CB electrons of exclusively one spin state. A thin epilayer is chosen to minimize strain relaxation away from the heterojunction. As the CB electrons diffuse to the surface, they undergo some depolarization, primarily by interaction with holes. This effect can be considerably reduced by decreasing the dopant density (everywhere but the last few nanometers near the surface, often called 'gradient doping'). Near the surface, the energy levels for pdoped GaAs bend downwards. Most of the electrons reaching the surface are confined to this band-bending region (BBR) for a finite time until they are emitted to vacuum or lose sufficient energy to be trapped in surface states. The BBR is depleted of holes. However, the confined but still mobile electrons in the BBR lose energy by scattering from optical phonons, as a result of which the amplitude and phase of the spin precession vector is continuously reoriented, leading to a significant depolarization. The probability for electrons to escape to vacuum can be as high as 20% if the surface is properly activated with cesium and an oxide to create a negative electron affinity (NEA). Energy dispersion studies show that most of these electrons have energies below that of the CBM in the bulk, while time-resolved polarization measurements demonstrate that the polarization of the emitted electrons drops continuously with time, consistent with the depolarization mechanism in the BBR described above.

The maximum polarization of the SLC beam was 78% at the source, produced using a 100 nm thick GaAsP/GaAs strained-layer photocathode. By decreasing the dopant density in the bulk, the polarization of this type of cathode was slightly improved for the initial run of a PV experiment (E158-I) at SLAC that required beam parameters similar to those for JLC/NLC. Higher polarization is an ongoing R&D endeavor. Several laboratories have demonstrated electron beams with polarization of 90% or even higher. The problem is that such high values are universally achieved only with a cathode surface having a relatively low quantum efficiency (QE), defined as number of photoemitted electrons per incident photon. Recent improvements in polarization while maintaining a high QE have been achieved with strained GaAsP/GaAs superlattice structures. Each layer of the superlattice (typically 4 nm) is considerably thinner than the critical thickness (10 nm) for the onset of strain relaxation, while the transport efficiency for electrons in the conduction band still can be high. In addition the effective band gap for such superlattices is larger than for GaAs alone, which improves the maximum NEA value and thus the surface escape probability. Today, 100 nm thick, gradient-doped GaAsP/GaAs superlattice photocathodes routinely yield at least 85% polarization at low energy with a maximized QE of 1%. This type of cathode was successfully used during the summer 2003 dedicated run at SLAC of E158-III, for which the polarization at high energy, measured by a Moller polarimeter, was (905% except for short periods following refreshment of the cathode QE (accomplished every few days by adding a small amount of Cs to the surface). This experience points to the possibility of a constant 90% polarization if a technique to control the minimum surface barrier can be developed without reintroducing the surface charge limit effect. Data for 2 SL photocathodes are compared with that for the strain-layer cathode in Table 1. The absolute accuracy of the polarimeters is on the order of 5%

The NLC ZDR describes a dc-biased polarized electron gun operating at 120 kV, i.e., very similar to that of the SLC polarized electron source. For JLC/NLC, because of space-charge effects, such a gun would have to produce first a 270 ns dc pulse. Before acceleration, the microstructure of the electron macropulse would then be generated by rf subharmonic bunchers, which will increase the rms normalized transverse emittance of the beam to the order of 10-4 m. Two alternatives are currently being investigated that would allow the micropulse structure to be generated by the laser itself: very high dc-bias and an

Cathode Structure	Growth Method	$P_e max$	λ_0 (nm)	$QE_{max}(\lambda_0)$	Polarimeter	Ref
1a GaAsP/GaAs strained SL	MOCVD	0.92	775 warm	0.005	Mott Nagoya	a
1b GaAsP/GaAs strained SL	MBE	0.86	783 warm	0.006	CTS Mott SLAC	b
		0.90	780 cold	0.008	Møller E158-III SLAC	c
2 GaAsP/GaAs strained-layer	MOCVD	0.82	805 warm	0.001	CTS Mott SLAC	d
		0.85	800 cold	0.004	Møller E158-I SLAC	e

Table 3.1: Comparison of the data for a 2 SL photocathodes and for the strain layer cathode .

rf gun. Advances in the technology of dc-guns may allow electric fields at the cathode as high as 20 MV/m or more, which is an order of magnitude higher than the SLC polarized electron source. The extracted beam should have a low transverse emittance, but since the energy is still quite low, the energy spread will be large so that after some acceleration the microbunches may need to be compressed. An rf gun offers the potential of a very low emittance beam (on the order of 10-6 m) at energies of several MeV so that additional bunch compression is not necessary. With either option the transport and accelerator capture efficiency will be improved so that the charge required for each micropulse would be significantly reduced. A low emittance beam will reduce damping ring requirements. It has not yet been demonstrated that the necessary surface properties of an activated GaAs photocathode will survive for a reasonable time in an operating rf gun.

Because of the large micropulse separation, the TESLA microstructure must be produced by the laser. The required 3 MHz (later 6 MHz), 3 W average power (during the 1-ms macropulse) laser (assuming cathode QE of 1% and capture/acceleration efficiency of 50%) with a repetition rate of only a few hertz can in principle be used with either a low-voltage dc gun (each micropulse ¿0.5 ns), a high-voltage dc gun, or using a ¡100 ps pulsewidth with an L-band rf gun. The JLC/NLC micropulse structure can be produced by amplifying a shaped 300-ns string of 714 MHz oscillator micropulses to the level of just over 200 W using, for example, a regenerative amplifier with multiple pumps. Neither laser system has been demonstrated, but both appear to be reasonably doable. The SLC demonstrated that the longitudinally polarized electrons produced at the gun can be transported to the IP with virtually no loss of polarization. Because the JLC/NLC damping ring will operate at constant energy far from a resonance, the polarization of the virtually monoenergetic electron beam, with the spin vector flipped to vertical, will undergo no loss during damping. While there is also no loss of polarization during acceleration in a linac, a loss of 1% is expected in the 180-degree turnaround into the main linac at 8 GeV due to spin diffusion. In the SLC, the polarization vector in the linac had a transverse component to accommodate control of the flat beam. The spin vector was adjusted to longitudinal at the IP by use of spin bumps in the arcs that were independent of the controls for the orientation of the flat beam.

3.2 Positron Polarisation

3.2.1 Laser-Compton Based Polarized Positron Source

This chapter describes the design of a laser-Compton based polarized positron source [139]. In this design, the Compton scattering of circularly polarized laser light off a relativistic electron beam is utilized. Polarized γ-rays are created in the scattering, and then polarized positrons are produced in the subsequent pair-creation on a thin conversion target. Linear colliders usually require huge amount of positrons with multi-bunch/multi-train timing structure, but details of timing structure depend on design of main linacs. Here we assume the requirements of GLC design [140]. In order to meet this requirements, we employ 10 CO_2 lasers, a high current and low emittance electron beam, and multiple laser-electron collision points (see Fig. 1). The electron and laser beams have a multi-bunch structure. As for the time structure of the beam of the main linac, the choice in the polarized positron option is different from that in the standard GLC design, i.e. 96 bunches with a bunch spacing of 2.8 ns in a train. Therefore, the bunch spacings of the electron and laser beams for the positron production, which must agree with that of the main linac, are also 2.8 ns. The 2.8 ns bunch spacing is chosen in order to facilitate the arrangement of the laser optics for the positron source. The number of positrons (electrons) in a bunch for the main linac becomes 1.1×10^{10}, instead of 0.75×10^{10} in the standard GLC design.

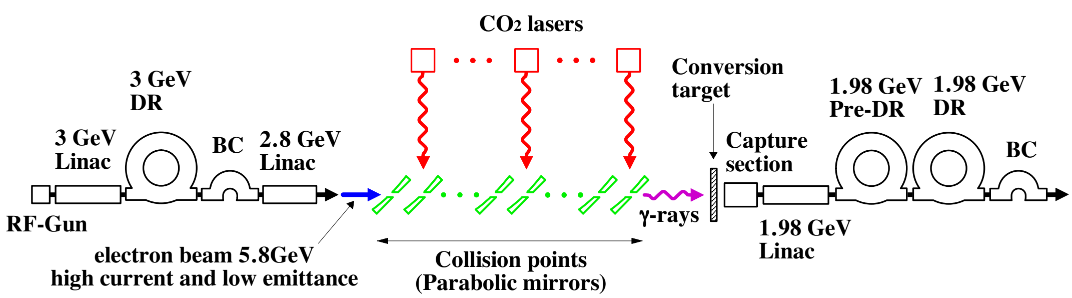

Figure 1: Configuration

A pair of off-axis parabolic mirrors located on the electron beam line is employed for each laser-electron collision point. The first mirror changes the direction of laser propagation, and focuses the laser beam as well, so that the laser beam and the electron beam run on the same axis in opposite directions. The focal length of the mirror is 90 mm and the rms spot size of the laser beam at the focal point is 17 μm. The laser beam collides head-on with the electron beam at the focal point of the laser beam. After the collision, the laser beam is extracted by the second mirror, as shown in Fig. 2. Each mirror has a hole at the center along the electron beam axis. The electron beam and the back-scattered γ-rays pass through these holes. The length of a mirror pair is approximately 200 mm. This compactness allows us to put many pairs in the electron beam line to have multiple collision points.

For multiple collisions of an electron beam at many collision points spread along the beam line, the electron beam is required to have a very low emittance, which is necessary to create a tightly focused beam over a long distance. A 3 GeV multi-bunch electron beam, which is delivered from a linac, is damped by the damping ring to achieve low emittance: 1.25×10^{-6} rad-m in both the horizontal and vertical directions. The damping ring is operated in full horizontal-vertical coupling mode. Then, the electron beam is accelerated again by another linac up to 5.8 GeV. Since the emittance of the electron beam is small, a focus system with a large β value ($\beta^* = 3.6$ m) can be employed. The spot size of the electron beam at the waist is 20 μm in sigma, and the spot size remains 23 μm even at 2.1 m away from the waist. We put 20 pairs of the parabolic mirrors in one section, in which 20 collision points are available (see Fig. 2). A single laser provides laser bunches in those 20 collision points through all 20 parabolic mirror pairs. The laser beam firstly enters the pair located at the most downstream position of the electron beam, and travels to the upstream pair. Thus, the laser beam goes from one pair to the next pair, and finally reaches the 20-th pair, which is located at the most upstream position of the electron beam. The number of electrons in a bunch is 5×10^{10} and the laser bunch energy is 0.25 J. A train of the electron beam contains 96 bunches, while a train of the laser beam contains 115 bunches. These extra laser bunches are necessary to realize collisions at all of the 20 collision points. Then, when the distance and laser path length between adjacent collision points are properly arranged, it can be realized that all 96 bunches in the electron beam collide 20 times at the 20 collision points.

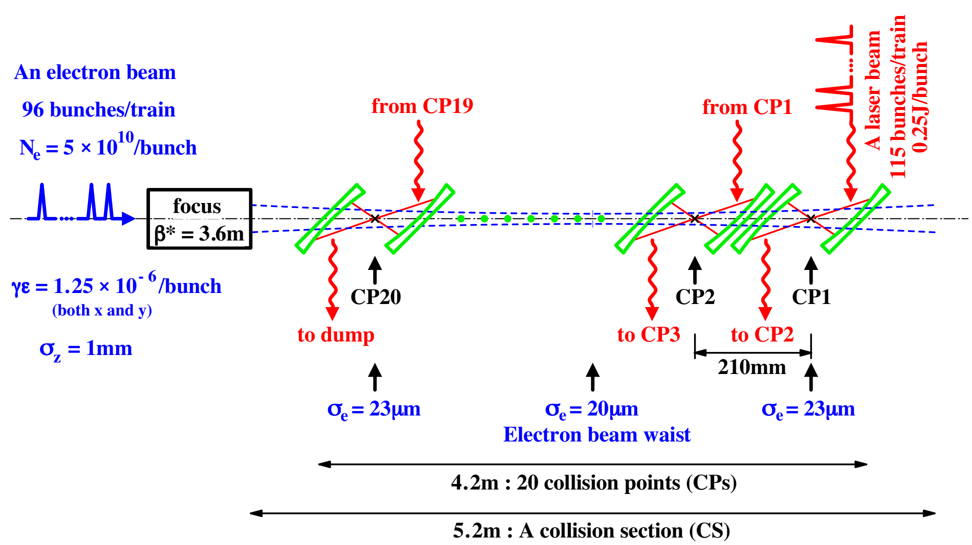

Figure 2: A collision section.

The number of γ-rays generated in the 20 collisions is not large enough to create the required number of positrons. Therefore, the electron beam is refocused so as to make another 20 collisions in the next section, to which another laser beam from another CO_2 laser is delivered. Such refocusing of the electron beam is repeated 9 times. Thus, the entire system has 200 collision points in 10 collision sections (Fig. 3).

The number of γ-rays generated in the 200 collisions is 8.3×10^{11}/bunch (see Fig. 4(a)). Out of them, 5.5×10^{11} γ-rays pass the collimators, which are located along the electron beam line to protect mirrors against radiation damage, and reach the conversion target. The electron-laser collision is simulated by using CAIN [141]. The thickness of the con-

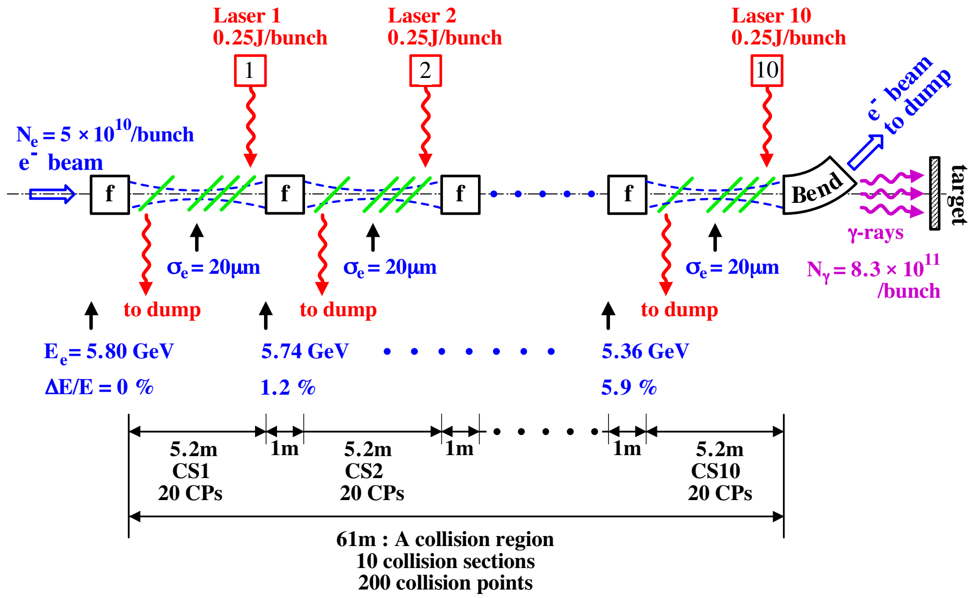

Figure 3: Entire collision region. There are 10 collision sections in total. Between adjacent collision sections, there are refocusing magnets to maintain an electron beam size small in every collision points. Many collimators (they are not written) are put in the electron beam line for mirror protection.

version target is 0.5 radiation length, and the target is made of tungsten. The number of positrons created from γ-rays is 6.9×10^{10} in each bunch (see Fig. 4(b)). The energy deposit on the target by a train (96 bunches) of γ-ray beam is about 10 J, and thermal stress caused by this deposit is estimated to be within tolerable range. The continuous heat load on the target is rather small, 1.5 kW.

A positron capture section consisting of an L-band accelerating structure with a 6 Tesla solenoid magnet is equipped just after the conversion target. The linac, the pre-damping ring, and the damping ring all having an energy of 1.98 GeV follow the capture section (see Fig. 1), which can capture $18\ \%$ of pair-created positrons at the relatively high energy side of the spectrum. As a result, 1.2×10^{10} positrons/bunch are captured, and the achieved magnitude of the polarization is $54\ \%$.

A rough estimation shows that the total power consumption, including every compornents shown in Fig. 1, of the positron source to be applroximately 22 MW.

At KEK, it has been pursued thta the development of advanced technologies for polarized γ-ray generation using the 1.28 GeV electron beam of KEK-ATF and a Nd-YAG laser beam [142]. It is remarked that recently the polarization of short pulse γ-rays has been successfully measured [143], and we plan to take a further steps of to produce polarized positrons and to measure of their polarization.

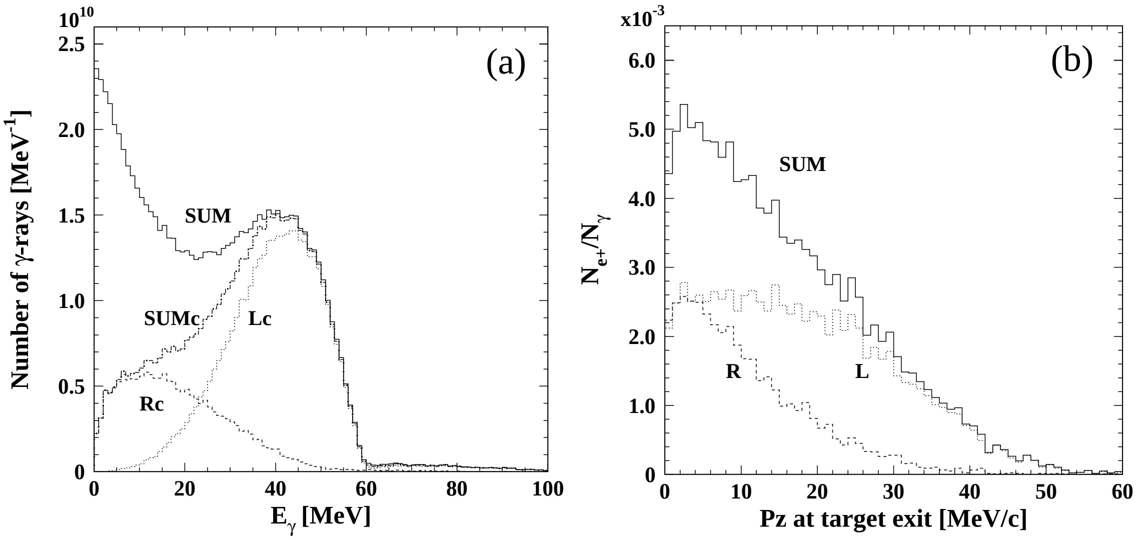

Figure 4: (a) Energy distribution of the whole γ-rays generated by a simulation of 200 collisions (SUM). Also, the γ-rays which pass all collimators and reach the target are indicated separately for the left-handed ones (Lc), the right-hand ones (Rc), and the total (SUMc). Here we assume that the initial laser beams have 100% right-handed polarization. (b) The energy distributions of the positrons at the target exit. The vertical axis is the number of positrons per MeV/c normalized by the total number of γ-rays on the target. Three lines show all positrons (SUM), positrons which have left-hand (L) and right-hand (R) helicity, respectively.

3.2.2 Undulator-based polarised positron source

contribution from John Sheppard

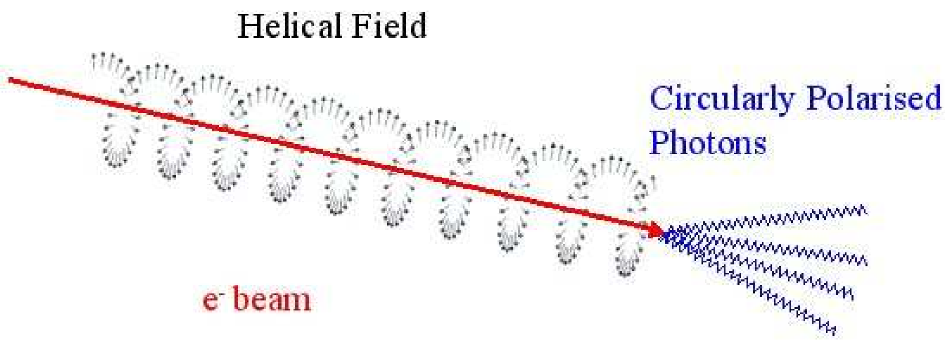

Figure 5: Helical field generating circularly polarised photons

3.2.3 Helical undulator design at Daresbury

ASTeC is involved in designing a helical undulator for the TESLA project.

One of the greatest challenges for any of the proposed Next Linear Colliders is efficient positron production. One of the possible schemes involves using radiation created by the main electron passing through a very long (100m) undulator. This radiation hits a special target in which electron and positron pairs are produced. The positrons can then be captured and accelerated down the main positron linac.

To create a polarised positron beam circularly polarised light from a helical undulator is needed. The transverse magnetic field of a helical undulator means that an electron would follow a helical trajectory through the device - emitting circularly polarised photons. (shown in Figure)

As the energy of the radiation increases so does the rate of electron positron production in the target - up to an energy of 20MeV. To create the highest radiation flux the period of the undulator needs to be as small as possible so that there are as many periods as possible in the available space (100m). These parameters along with the 250 GeV energy of the TESLA beam mean that for a particular undulator period the required on-axis field is easily defined. The shorter the period the higher the field required.

Required on axis field as a function of undulator period to produce 20MeV circularly polarised radiation with a 250 GeV electron beam.

After looking at many different designs including pure permanent magnet planar helical device and other novel magnetic arrangements two different solutions have been recommended.

The first is a super-conducting bi-filar wire. Here two s-c wires are wrapped in a double helix around the vacuum vessel. When current is passed through the wires the longitudinal components of the magnetic field cancel leaving only the rotating (helical) field required on axis.

Schematic of wires wrapped in helix around a former showing different current directions.

The second option is based on permanent magnet technology. Here a dipole field is create by a ring of permanent magnet blocks, with each blocks magnetisation vector rotated around the ring. Many rings are then stacked together so that along a period the

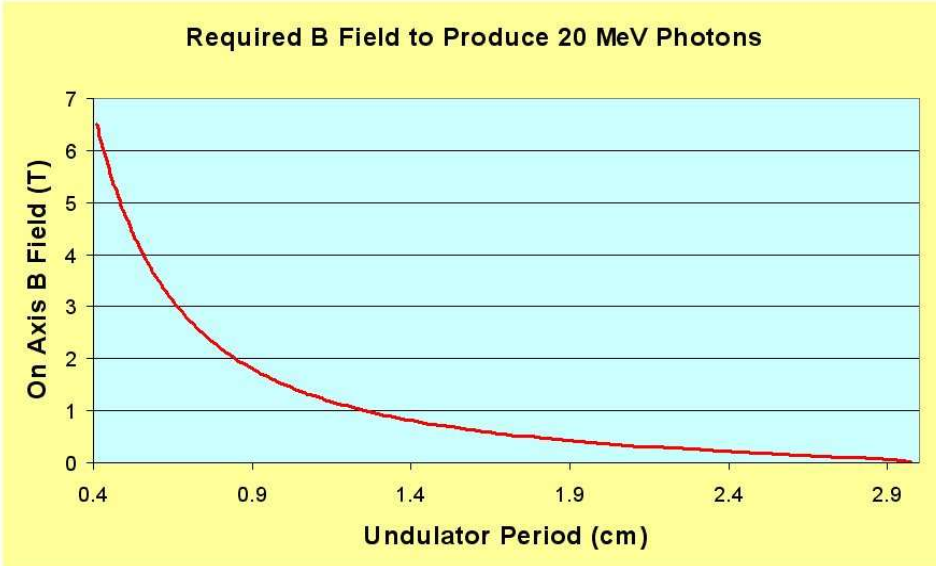

Figure 6: On-axis-B-field versus undulator period

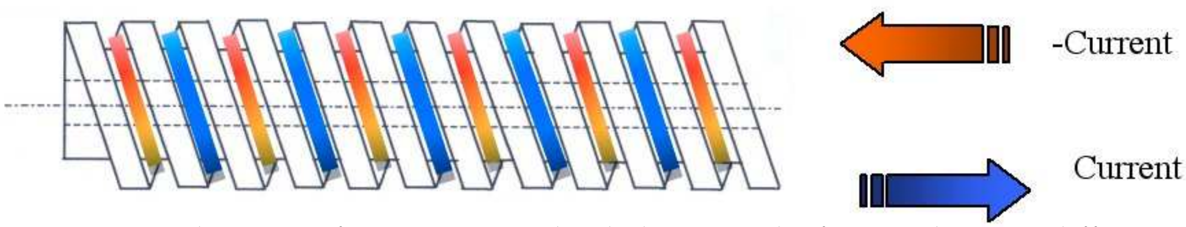

Figure 7: Schematic of wires wrapped in helix around a former showing different current directions.

Figure 8: SC prototype

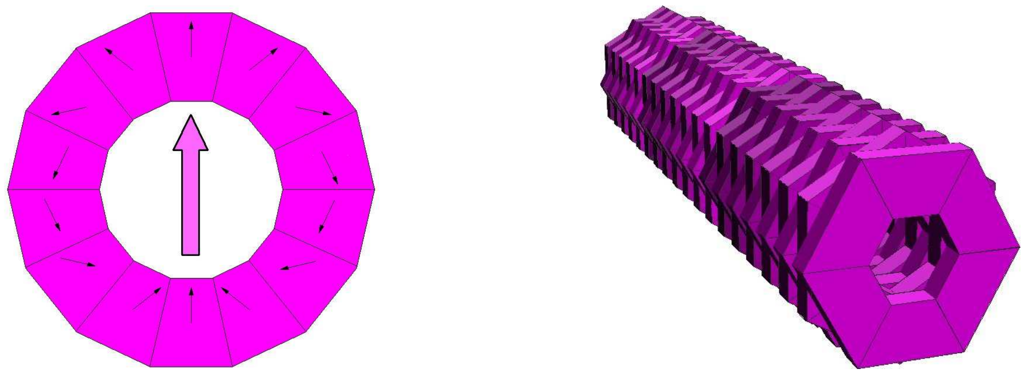

Figure 9: PPM design

Period	On-Axis Field	Magnet Aperture	Material	Current density	Length	Full Module
14 mm	0.85 T	6 mm	NbTi	1000 A/mm^2	30 cm	1-2 m

Table 3.2: SC helical undulator design at Daresbury

dipole field is rotated by 360 degrees. This type of arrangement is called a HALBACH helical undulator.

Dipole field created by many blocks arranged in a ring. Many rings are stacked together to create the helical field

The work done has shown that devices with a period of 14mm look feasible for both different types of technology. It is hoped that over the next year construction of prototypes of both different technologies will commence in order to provide a better understanding of the pros and cons of each design. Each prototype will be around ten or twenty periods long. They are to be used to measure the quality of the magnetic field on axis and to give an initial assessment of the engineering difficulties in constructing such devices, which have not widely been built. The following basic parameters for each device are to be used for the prototypes.

It has been decided that for the prototypes both devices will have a period of 14mm to allow for a good comparison between the two. As can be seen from the numbers modelling of the permanent magnet device suggests that it can produce a higher on axis field than is required so possibly the period could be reduced. However magnet inhomogenieties, magnetisation vector misalignments and engineering tolerances will mean that the measured on axis field will be less. How much is less is one of the reasons for building a prototype.

For the super-conducting device use of Niobium-Tin as a material could increase the on axis magnetic field and so allow for the period to be reduced. This material is relatively

Period	On-Axis Field	Magnet Aperture	Material	Length	Full Module
14 mm	0.83 T	4 mm	NbFeB (1.3 T)	15 cm	5 m

Table 3.3: PPM helical undulator design at Daresbury

new and difficult to work with and so has not been considered for the prototype. The use of iron poles to increase the flux density on-axis is also being considered - although this makes fabrication of the former more difficult.

There are still a number of technical issues that need to be solved and effects that are dependant on the beam properties of the machine that need to be calculated. It is hoped that in the near future a fully working proto-type module will be built. This will further test the engineering difficulties of the design and look at the emitted radiation characteristics.

3.3 Transverse Polarisation

Contribution from John Sheppard

Chapter 4

Polarisation Measurement

4.1 Polarisation Measurement at the NLC

The primary polarimeter measurement at the NLC will be performed by a Compton polarimeter located in the extraction line approximately 60 meters downstream from the Interaction Point [144]. An accuracy of $(\Delta P_{e^-}/P_{e^-}) = 0.25\%$ should be achievable [145]. The location in the extraction line is shown in Figure 1. It is at a secondary focus in the middle of a chicane with 20 mm dispersion, but with no net bend angle with respect to the primary IP. At the middle of the chicane the Compton scattering will occur and the scattered electron is confined to a cone having a half-angle of $\theta = 2$ rad and is effectively collinear with the initial electron direction. This extraction line geometry is feasible in the NLC design due to the non-zero crossing angle at the IP; beam losses in the extraction line are acceptable, both for machine protection [146,147] and for detector backgrounds. A location downstream of the IP is chosen so that beam-beam depolarization effects [148,149] can be measured directly by comparing beams in and out of collision. Also, spin precession effects due to the final focus optics and beam-beam deflections can be studied by correlating the polarization and IP BPM measurements.

Compton polarimetry is chosen as the primary polarimetry technique for several reasons:

- The physics of the scattering process is well understood QED, with radiative corrections less than 0.1% [150];
- Detector backgrounds are easy to measure and correct for by using laser off pulses;
- Polarimetry data can be taken parasitic to physics data;
- The Compton scattering rate is high and small statistical errors can be achieved in a short amount of time (sub-1% precision in a few minutes is feasible);
- The laser helicity can be selected on a pulse-by-pulse basis;
- The laser polarization is readily determined with 0.1% accuracy.

A frequency doubled Nd:YAG laser will be used with a wavelength of 532 nm (2.33 eV). The laser will fire on every 7^{th} pulse train, but every 10 seconds will fire instead on the 6^{th} pulse train; this gives an average repetition frequency of 17 Hz. The laser pulse energy will be 200 mJ. The duration of the Q-switched laser pulse is 6 nano-seconds (if desired, this can be sliced to achieve a narrower pulse). The kinematic endpoint for Compton electrons scattered from a 250 GeV beam occurs at 25.1 GeV with an analyzing power of 98%. Figure 2 shows the resulting $J_z = 3/2$ and $J_z = 1/2$ Compton cross sections and analyzing power. The laser rms spot size at the Compton interaction point will be 100 m. Comparison of the electron and laser beam sizes at the Compton IP is shown in Figure 3 (need to update).

A segmented electron detector sampling the flux of scattered electrons near the kinematic endpoint will provide a good polarization measurement with high analyzing power. The counting rate is high with xxx Compton electrons per GeV at the endpoint energy of 25.1 GeV. We plan to use a threshold Cerenkov detector, similar to that employed in the SLD Compton polarimeter [151]. Using propane with an index of refraction of 1.0011 gives the threshold energy as 11 MeV. Figure 4 shows the y-distribution of the Compton scattered electrons at the Cerenkov detector located 21 meters downstream of the Compton interaction point. The Compton-edge electrons peak at 18 cm while the tails of the electron beam extend out only a few centimeters. There is good separation between the Compton edge electrons and the disrupted beam as seen in Figure 4.

The analyzing power for a power asymmetry measurement by an integrating Compton photon detector is much lower at x.x%. A photon detector [152] interferes with the large beam stay clear needed in this region to accommodate the beamstrahlung photons. An invasive measurement with an insertable photon detector and the beams out of collision can be useful, however, as a systematic cross check of the polarization scale. Ideally, detectors should allow for measurements of both backscattered electrons and photons, and possibly to compare single and multi-Compton counting. These independent techniques can be extremely useful for evaluating systematic errors.

The luminosity-weighted beam polarization will differ from the measured polarization due to disruption and radiation in the beam-beam collision process. There are also effects from polarization spread and spin transport to the IP. At the NLC, the largest source of polarization spread before the IP is expected to result from the 180-degree turnaround after the pre-Linac, where the beam energy is 8 GeV. The 0.25% energy spread there results in a spin diffusion of 1% rms. The polarization spread for different bunches along the bunch train is expected to be small; we plan to measure the polarization for different bunches by varying the timing of the laser pulse. The polarization spread at the IP will have some correlation with the energy, E, and z (longitudinal position of electrons within a bunch) of the particle distributions at the IP. Because the luminosity may depend on E and z, this can lead to the $\Delta P = P^{lumi-wt} - P^{polarimeter}$ being non-zero. Spin precession and spin diffusion from the final focus magnets are additional sources of ΔP. Also, the detector solenoid and the crossing angle result in a transverse B-field component that causes a small amount of spin precession between the IP and the Polarimeter. Beambeam effects contribute to ΔP due to the disruption and deflection angles and due to spinflip beamstrahlung radiation [148, 149] The estimated systematic uncertainties for the measurement of polarization asymmetries is summarized in Table 1, together with the results achieved for the SLD Experiment.

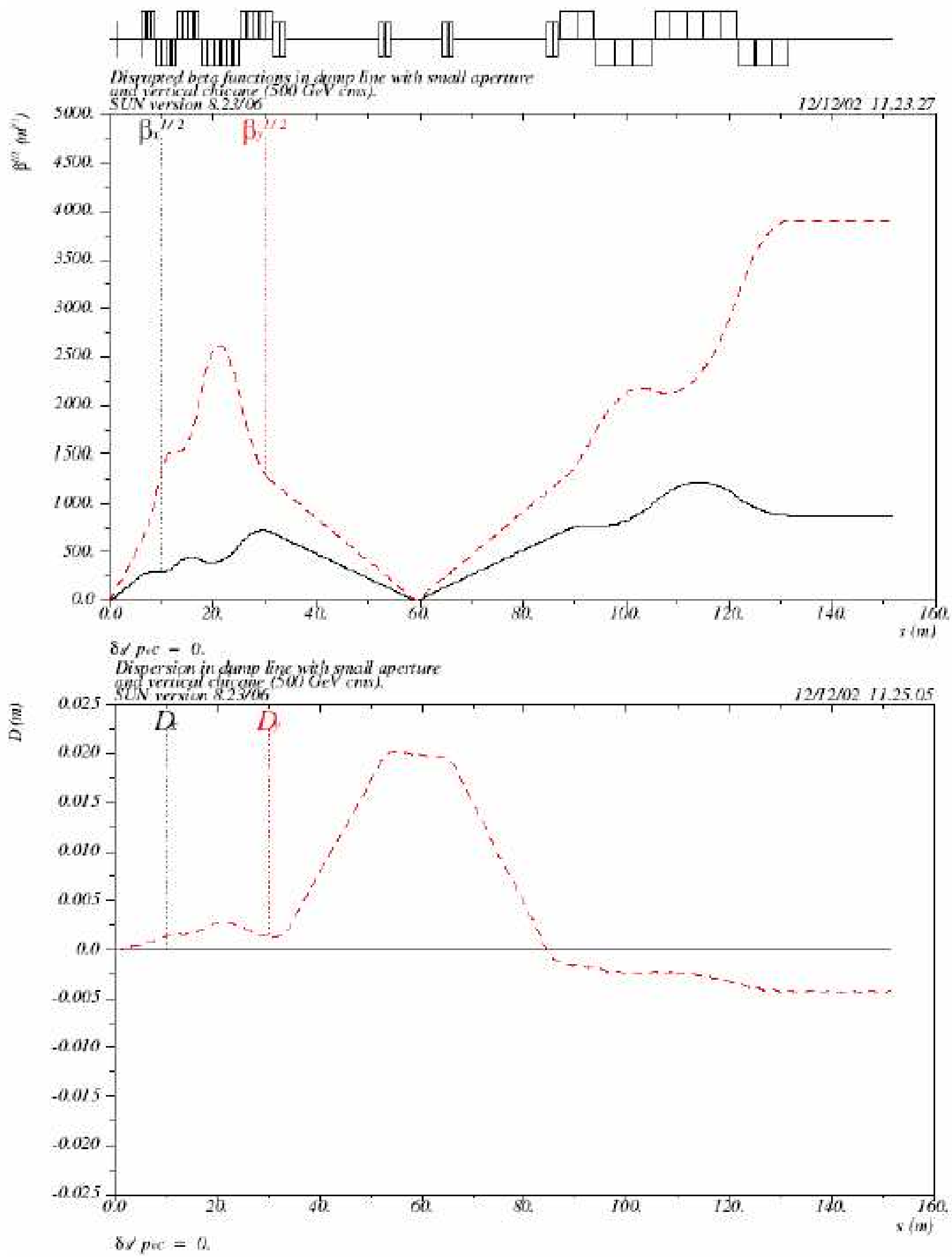

Figure 1: Beta-functions and dispersion in the extraction line as a function of distance from the IP. The Compton IP wll be located at the secondary focus 59.32 meters downstream.

Item	SLD Result	NLC-500
Laser Polarisation	0.1%	0.1%
Detector Linearity	0.2%	0.1 %
Analysing Power	0.4%	0.2%
Electronic Noise	0.2%	0.05 %
Lumi-weighting corrections	0.1%	0.1 %
TOTAL	0.5%	0.27%

Table 4.1: Systematic Uncertainties in Polarization Measurement, achieved at SLD and expected at NLC Item SLD Result NLC-500 Laser

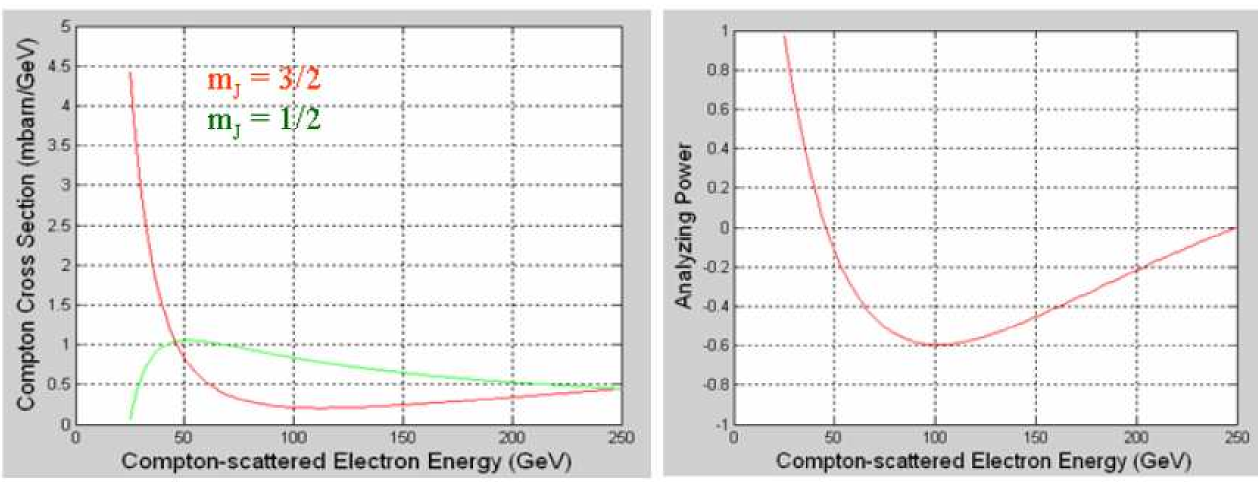

Figure 2: Compton cross section for scattering of 532 nm photons with a 250-GeV electron beam. The J=3/2 (1/2) cross section for electron and photon spins aligned (anti-aligned) is shown in red (green).

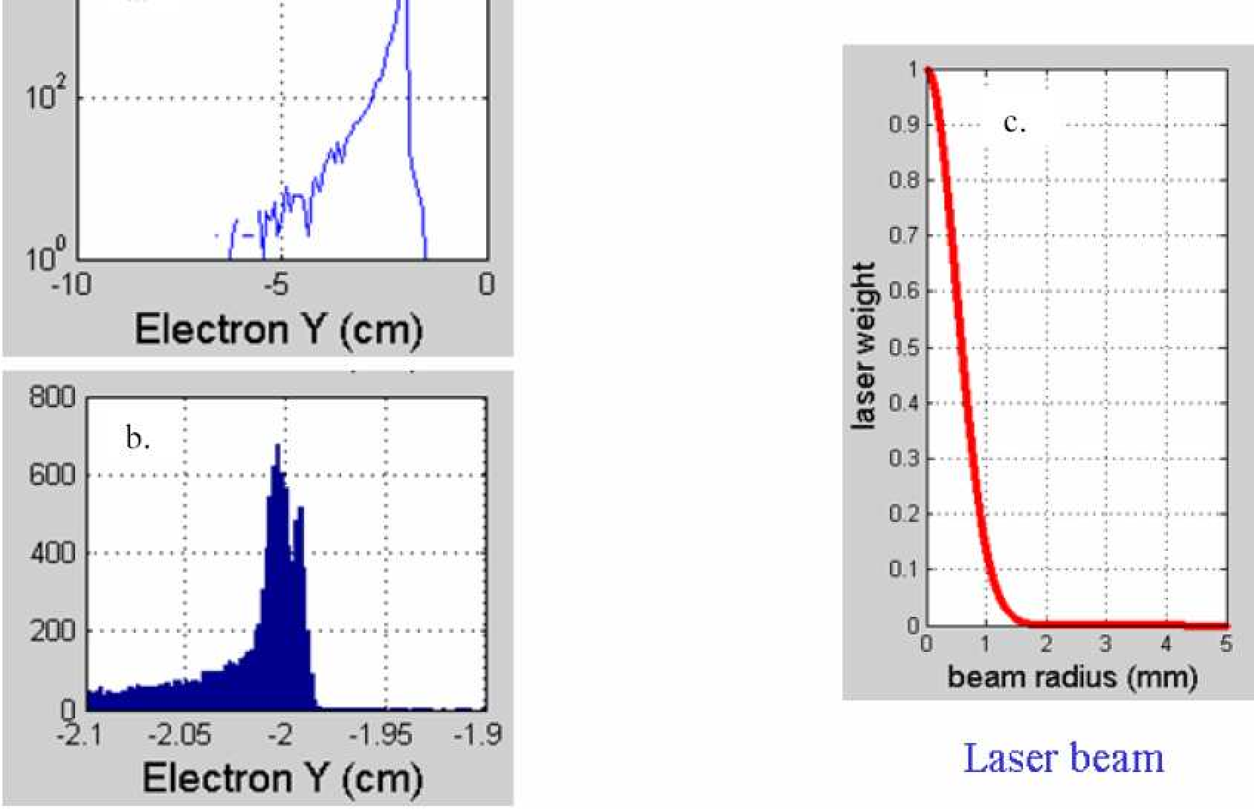

Figure 3: Electron distributions (a. and b.) with energy spread and beam disruption effects included; c) Laser beam size. All are at the Compton IP at mid-chicane.

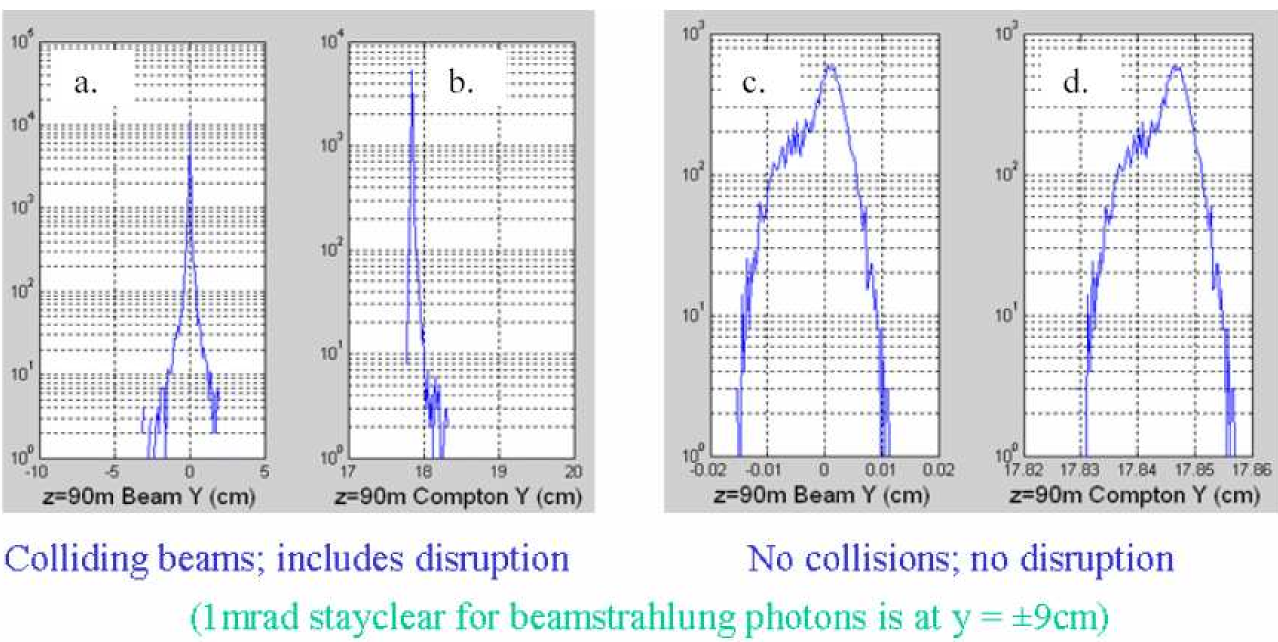

Figure 4: Beam electron (a. and c.) and Compton-edge electron (b. and d.) distributions at the detector located 21 meters downstream of the Compton collision point. The distributions on the left are for colliding beams and include disruption effects. The plots on the right are for e+e- beams out of collision.

4.2 Polarisation Measurement at TESLA

Contribution from Peter Schueler

4.3 Polarisation Measurements with Annihilation Data

Polarisation measurements with polarimeters are limited to a total precision around 0.25%. In addition polarimeters measure either the polarisation of the incoming beam that has not been depolarised by the beam-beam interaction or the one of the outgoing beam which has been depolarised three to four time as much as the interacting particles. On the other hand there are several processes at a linear collider whose polarisation structure is known and which might be used to measure the polarisation directly from data. The large luminosity of the linear collider offers the possibility to reach a precision much better then the polarimeters.

One example is the $\sin^2\theta_{\mathrm{eff}}$ measurement with the Blondel scheme at GigaZ (see sec. 2.6) where the relevant observables can be extracted directly from the data without the use of polarimeters. One has, however, to take into account that all methods using annihilation data involve some physics assumptions that have to be considered in the framework of the model in which the data are analysed. The data driven methods also cannot replace completely the polarimeters. The data methods need a large luminosity to get to a precise result while polarimeters are completely systematics limited and statistics is no problem. In any case polarimeters are thus needed for a fast machine tuning. In addition there are some assumptions in the data-methods that have to be verified or corrected with the polarimeters. In all cases the data methods need the assumption that the absolute values of the polarisations of the left and right handed states are the same. If electron and positron polarisation is available the effective polarisations, explained in sec. 1.3 and the formulae to obtain the polarisation involve linear and quadratic terms of the polarisations. For these reasons any correlations between the two beam polarisations need to be known from beam-beam simulations and polarimeters.

4.3.1 Measurements with Electron Polarisation only

If only electron polarisation is available not only the Lorenz structure of the used process is needed but the exact helicity structure needs to be known. The only process fulfilling this requirement is the V-A structure of the W-fermion couplings. This coupling can be utilised in two processes at a linear collider, single W production and W-pair production. As can be seen from figure 5 both processes have a cross section of several pb so that a few million events are expected.

W-pair production proceeds through the Feynman diagrams shown in figure 6. In general the process is a complicated mixture of the neutrino t-channel exchange, only determined by the W-fermion couplings, and the γ and Z s-channel exchange that involve also anomalous gauge couplings. However, as shown in figure 7, the forward pole is completely determined by the neutrino exchange and insensitive to the anomalous couplings. For this reason it is possible to extract the polarisation and the triple gauge couplings [153] simultaneously from the W-pair data sample. The expected precision is $\Delta\mathcal{P}_{e^-}/\mathcal{P}_{e^-} = 0.1\%$ for a luminosity of $500\,\mathrm{fb}^{-1}$ at $\sqrt{s} = 340\,\mathrm{GeV}$. The correlation with the anomalous gauge couplings is negligible and the only assumption involved is that no right-handed W-fermion couplings appear. Experimental details of the analysis can be found in [154].

If electron and positron polarisation is available, both can be measured simultaneously from the W-pair sample. With equal luminosity at all four helicity combinations and

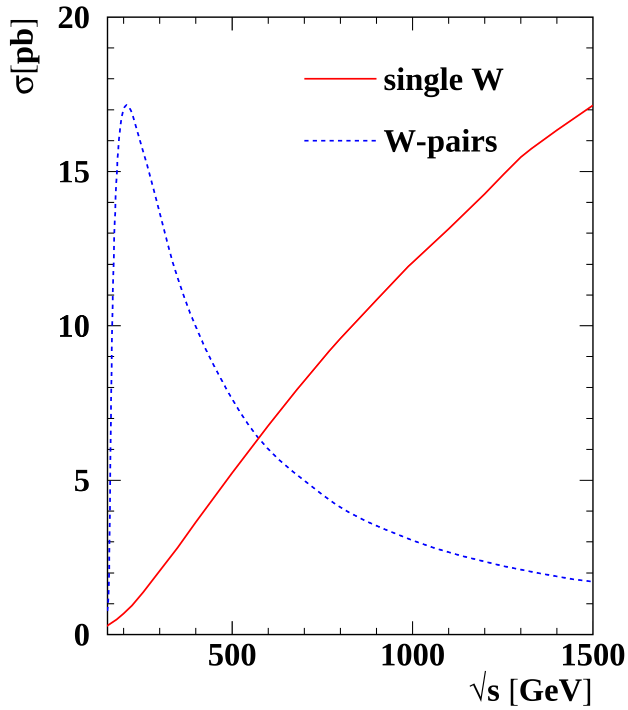

Figure 5: Cross section for single W and W-pair production at a LC

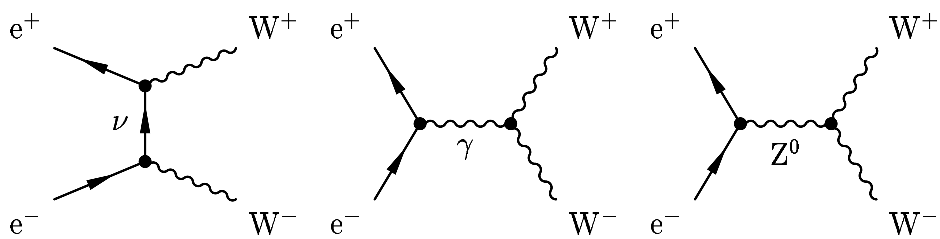

Figure 6: Feynman graphs for the production of W-pairs in $\mathrm{e}^+\mathrm{e}^-$-annihilation.

$\mathcal{P}_{e^-} = 0.8$, $\mathcal{P}_{e^+} = 0.6$ one gets $\Delta\mathcal{P}_{e^-}/\mathcal{P}_{e^-} \approx 0.1\%$ and $\Delta\mathcal{P}_{e^+}/\mathcal{P}_{e^+} \approx 0.2\%$ and negligible correlations between the polarisations and between the polarisation and the couplings. If only 10% of the luminosity is spent on the equal helicities the polarisation errors increase by roughly a factor two with -50% correlation.

Single W production is dominated by the Feynman diagram shown in figure 8. Since this process involves the V-A coupling of the W to fermions a W^- can only be produced from a left-handed electron and a W^+ from a right-handed positron. Measuring the W-charge the polarisation can thus be measured for electrons and positrons separately. The outgoing electron usually disappears in the beampipe so that the W charge has to be reconstructed from the W decay products. This means that only leptonic W-decays can be used for the analysis. No detailed simulation study exists yet. The experimental signature is a single lepton in the detector which can be measured with high efficiency and small background. Because of the usually small W energy also the interference with W-pair production should be very small. Assuming $\sqrt{s} = 500\,\mathrm{GeV}$, $\mathcal{L} = 1\mathrm{ab}^{-1}$ and 100% efficiency for $W^- \to e^-, \mu^-$ an error of $\Delta\mathcal{P}_{e^-}/\mathcal{P}_{e^-} \sim 0.15\%$ is expected.

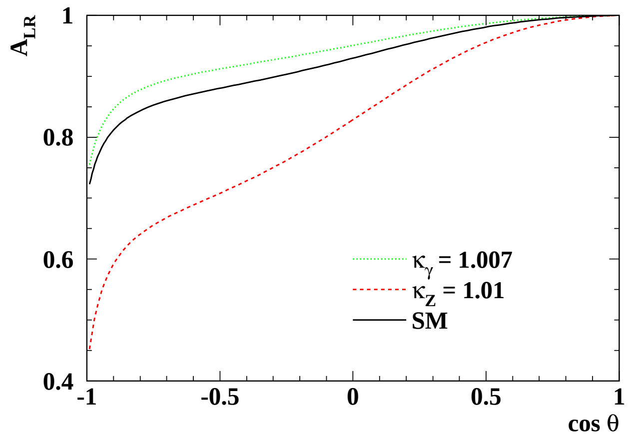

Figure 7: Left-right asymmetry of W-pair production as a function of the polar angle in the Standard Model and with anomalous triple gauge couplings.

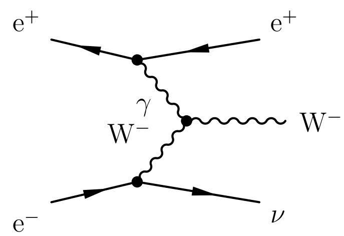

Figure 8: Dominating Feynman graph for single W production in $\mathrm{e^+e^-}$-annihilation.

4.3.2 The Blondel scheme

If a process $\mathrm{e^+e^-} \to \mathrm{f\,f}$ is mediated by pure s-channel vector-particle exchange the cross section for the different polarisation states with electron and positron polarisation available can be written as

$$\sigma \;=\; \sigma_u \left[1 - \mathcal{P}_{e^+}\mathcal{P}_{e^-} + \mathrm{A_{LR}}(\mathcal{P}_{e^+} - \mathcal{P}_{e^-})\right], \tag{1}$$

where $\mathcal{P}_{e^+}$ and $\mathcal{P}_{e^-}$ are the longitudinal polarisations of the positrons and electrons measured in the direction of the particle's velocity. σ_u denotes the unpolarised cross section and $\mathrm{A_{LR}}$ the left-right asymmetry. If the signs of the two polarisations can be switched independently four cross sections can be measured for four unknowns. From these cross sections the polarisations can be obtained, if $\mathrm{A_{LR}} \neq 0$:

$$\mathcal{P}_{e^\pm} \;=\; \sqrt{\frac{(\sigma_{+-}+\sigma_{-+}-\sigma_{++}-\sigma_{--})(\mp\sigma_{+-}\pm\sigma_{-+}-\sigma_{++}+\sigma_{--})}{(\sigma_{+-}+\sigma_{-+}+\sigma_{++}+\sigma_{--})(\mp\sigma_{+-}\pm\sigma_{-+}+\sigma_{++}-\sigma_{--})}}$$

where in σ_{ij} i denotes the sign of the positron- and j the sign of the electron-polarisation. As a drawback of this method some luminosity needs to be spent with the same helicities for both beams which is not very interesting for most physics processes.

To measure the polarisation with this scheme two processes have been considered,

- $\mathrm{e^+e^-} \to \mathrm{f\,f}$ with $\sqrt{s'} \approx \sqrt{s}$;

- radiative return events ($e^+e^- \rightarrow Z\gamma \rightarrow f\bar{f}\gamma$).

The cross section and left right asymmetry for the two processes at $\sqrt{s} = 350$ and $500\,\mathrm{GeV}$ is given in table 4.2. Both cross sections scale approximately with $1/s$. The high energy

$\sqrt{s}$	σ_{RR}	$\mathrm{A_{LR}}(RR)$	σ_{HE}	$\mathrm{A_{LR}}(HE)$
$340\,\mathrm{GeV}$	$17\,\mathrm{pb}$	0.19	$5\,\mathrm{pb}$	0.50
$500\,\mathrm{GeV}$	$7\,\mathrm{pb}$	0.19	$2\,\mathrm{pb}$	0.50

Table 4.2: Cross section and asymmetry for high energy and radiative return $f\bar{f}$ events.

events can be measured with high efficiency and almost no background. However the analysis relies on the assumption of s-channel vector-exchange, so for analyses like the search for R-parity violating sneutrinos the results cannot be used.

On the contrary radiative return events contain on-shell Z-decays which are well understood from LEP1 and SLD. In about 90% of the events the high-energy photon is lost in the beampipe. These events can be reconstructed kinematically and most backgrounds can be rejected. However, at TESLA energies the cross section for the fusion process $e^+e^- \rightarrow Ze^+e^-$ is of the same order as the signal. In those events one electron has almost the beam energy and stays at low angle while the other is extremely soft and also often lost in the beampipe resulting in a $\sim 30\%$ background of Zee events in the radiative return sample. The only way Zee events can be rejected is to require a photon above 7° where photons and electrons can be separated by the tracking detectors. Applying some additional event selection cuts on the hadronic mass and the balance of the event about 9% of the radiative return events are accepted with only a small Zee background. However in these events the slow electron is seen in the detector, so that they can easily be rejected by vetoing on an isolated electron.

Assuming $\mathcal{P}_{e^-} = 80\%$, $\mathcal{P}_{e^+} = 60\%$, an integrated luminosity of $500\,\mathrm{fb}^{-1}$ at $\sqrt{s} = 340\,\mathrm{GeV}$ and 50% or 10% of the luminosity spent with both beam polarisations with the same sign table 4.3 shows the obtainable errors on the two polarisations and their correlation. Due to the scaling of the cross sections the errors are about a factor $\sqrt{2}$ larger at $500\,\mathrm{GeV}$. It should be noted that the relative errors scale approximately with the product of the polarisations.

	$\mathcal{L}_{\pm\pm}/\mathcal{L} = 0.5$			$\mathcal{L}_{\pm\pm}/\mathcal{L} = 0.1$		
	HE	rr	WW	HE	rr	WW
$\Delta\mathcal{P}_{e^-}/\mathcal{P}_{e^-}$ [%]	0.10	0.51	0.07	0.21	1.11	0.11
$\Delta\mathcal{P}_{e^+}/\mathcal{P}_{e^+}$ [%]	0.12	0.53	0.11	0.15	1.13	0.21
corr	-0.49	-0.91	0	-0.56	-0.93	-0.52

Table 4.3: Relative polarisation error using the Blondel scheme for $\sqrt{s} = 340\,\mathrm{GeV}$, $\mathcal{L} = 500\,\mathrm{fb}^{-1}$, $\mathcal{P}_{e^-} = 0.8$, $\mathcal{P}_{e^+} = 0.6$ (HE = High energy events, rr = radiative return, WW = W-pair production).

Radiative corrections to the form of equation (1) have been checked with the KK MonteCarlo [155]. For the high energy events and for the radiative return events with a seen photon they are negligible. For the radiative return events where the photon is lost in the beampipe, which are not used in this analysis, the corrections are on the percent level.

Because of the high losses in the selection of the radiative return events the errors on the single polarisations seem rather large. However the large negative correlation reduces the error substantially for the effective polarisations needed in the analysis. Table 4.4 compares the errors on the effective polarisations for the setups shown in table 4.3 and for polarimeter measurements assuming 0 or 50% correlation between the two polarimeters.

The effective polarisations considered are:

- $\mathcal{P}_{\rm eff} = \frac{\mathcal{P}_{e^-}+\mathcal{P}_{e^+}}{1+\mathcal{P}_{e^-}\mathcal{P}_{e^+}}$, relevant for $\mathrm{A_{LR}}$ with s-channel vector exchange;
- $\mathcal{P}_{e^-}\mathcal{P}_{e^+}$, relevant for the cross section suppression/enhancement with s-channel vector exchange;
- $\mathcal{P}_{e^-} + \mathcal{P}_{e^+} - \mathcal{P}_{e^-}\mathcal{P}_{e^+}$, relevant for the cross section suppression/enhancement for t-channel W-pair production.

Due to the high anti-correlation even the results from the radiative return analysis with one tenth of the luminosity at the low cross sections are competitive to polarimetry with an optimistic 0.5% error.

	value	Rel. error [%]							
		$\mathcal{L}_{\pm\pm}/\mathcal{L} = 0.5$			$\mathcal{L}_{\pm\pm}/\mathcal{L} = 0.1$			Polarimeter	
		HE	rr	WW	HE	rr	WW	$\rho{=}0$	$\rho{=}0.5$
$(\mathcal{P}_{e^-}{+}\mathcal{P}_{e^+})/(1{+}\mathcal{P}_{e^-}\mathcal{P}_{e^+})$	0.95	0.02	0.08	0.02	0.05	0.17	0.02	0.13	0.16
$\mathcal{P}_{e^-}\mathcal{P}_{e^+}$	0.48	0.11	0.22	0.13	0.18	0.42	0.18	0.71	0.87
$\mathcal{P}_{e^-}{+}\mathcal{P}_{e^+}{-}\mathcal{P}_{e^-}\mathcal{P}_{e^+}$	0.92	0.03	0.12	0.03	0.06	0.25	0.03	0.19	0.21

Table 4.4: Relative error on the effective polarisations for the discussed setups and $\sqrt{s} = 340\,\mathrm{GeV}$, $\mathcal{L} = 500\,\mathrm{fb}^{-1}$, $\mathcal{P}_{\mathrm{e}^-} = 0.8$, $\mathcal{P}_{\mathrm{e}^+} = 0.6$. For the polarimeter a total error of 0.5% has been assumed. (HE = High energy events, rr = radiative return, WW = W-pair production).

4.3.3 Experimental Aspects

Although the methods presented here measure in the luminosity weighted polarisation directly from the annihilation data some experimental assumptions are involved. In all cases it is assumed that the absolute values of the polarisation of the left- and right-handed state are the same and possible corrections have to be obtained from polarimeters. If the polarisation is written as $\mathcal{P} = \pm\langle|\mathcal{P}|\rangle + \delta\mathcal{P}$ The shift in the measured polarisation using Ws in the case of electron polarisation only is given by $\Delta\mathcal{P}/\mathcal{P} = \delta\mathcal{P}$

Using the Blondel scheme with electron and positron polarisation the corresponding errors are

$$\begin{aligned}\Delta\mathcal{P}_{e^-} &= 1.0\delta\mathcal{P}_{e^-} + 0.6\delta\mathcal{P}_{e^+}\\ \Delta\mathcal{P}_{e^+} &= -0.5\delta\mathcal{P}_{e^-} - 0.7\delta\mathcal{P}_{e^+}\end{aligned}$$

for the high energy events and

$$
\begin{aligned}
\Delta\mathcal{P}_{e^-} &= 2.4\delta\mathcal{P}_{e^-} + 2.1\delta\mathcal{P}_{e^+} \\
\Delta\mathcal{P}_{e^+} &= -1.7\delta\mathcal{P}_{e^-} - 1.7\delta\mathcal{P}_{e^+}
\end{aligned}
$$

for the radiative return sample.

The corresponding corrections have to be obtained from polarimeters. This is possible in a Compton polarimeter where the laser polarisation can be flipped easily. To assure that the electron-laser luminosity does not depend on the laser polarisation, or to correct for such effects, one should have a multichannel polarimeter with a large lever arm in the analysing power.

If electron and positron polarisation is available, in the formulae for the effective polarisations and for the Blondel scheme products of the two polarisations appear so that one has to understand the correlations between the electron and positron polarisation. In principle there can be a correlation due to the depolarisation in the bunch. Studies with CAIN [156], however, indicate that these correlations are small. Another source of correlation can come from time dependencies or spatial correlations due to the beam delivery system. If half of the luminosity is taken with a polarisation 5% higher and the other half 5% lower than average the polarisations obtained with the Blondel scheme are off by around 0.25% affecting the effective polarisation by the same amount. Measuring the polarisation with polarimeters would only result in a 0.16% error in the effective polarisation.

Time correlations have to be tracked with polarimeters. Spacial correlations due to the beam delivery system have to be obtained from simulations and should be minimised already in the design.

Chapter 5

Summary and Outlook

Le grand F I N A L E

Acknowledgements

Bibliography

[1] B. C. Allanach *et al.*, in *Proc. of the APS/DPF/DPB Summer Study on the Future of Particle Physics (Snowmass 2001)* ed. N. Graf, Eur. Phys. J. C **25** (2002) 113 [eConf **C010630** (2001) P125] [hep-ph/0202233].

[2] C. Blochinger, H. Fraas, G. Moortgat-Pick and W. Porod, Eur. Phys. J. C **24** (2002) 297 [hep-ph/0201282].

[3] D.J. Summers, Phys. Lett. D 274, 1992, 209

[4] R. Hawkings and K. Moenig, EPJ*direct* C 8 (1999) 1.

[5] G. Alexander and E. Reinherz-Aronis,*The Gain to Polarimetry and A(LR) Measurements from a Polarised Positron Beam in TESLA*, LC-PHSM-2003-032.

[6] S. Heinemeyer, Th. Mannel, G. Weiglein, hep-ph/9909538, LC Workshop, Sitges 1999; S. Heinemeyer, G. Weiglein, hep-ph/0012364, LCWS 2000, Chicago, Ocober 2000.

[7] J. Erler, S. Heinemeyer, W. Hollik, G. Weiglein and P. M. Zerwas, Phys. Lett. B **486** (2000) 125 [arXiv:hep-ph/0005024].

[8] R. Hawkings and K. Mönig, Eur. Phys. J. directC **1** (1999) 8 [arXiv:hep-ex/9910022].

[9] K. Mönig, private communication.

[10] [The LEP Higgs Working Group], Phys. Lett. B **565** (2003) 61 [arXiv:hep-ex/0306033].

[11] P. Wells, talk presented at HEP2003 Europhysics Conference, Aachen, July 2003.

[12] S. Heinemeyer, W. Hollik and G. Weiglein, Eur. Phys. J. C **9** (1999) 343 [arXiv:hep-ph/9812472];
G. Degrassi, S. Heinemeyer, W. Hollik, P. Slavich and G. Weiglein, Eur. Phys. J. C **28** (2003) 133 [arXiv:hep-ph/0212020].

[13] S. Heinemeyer and G. Weiglein, JHEP **0210** (2002) 072 [arXiv:hep-ph/0209305].

[14] S. Heinemeyer, W. Hollik and G. Weiglein, Comput. Phys. Commun. **124** (2000) 76 [arXiv:hep-ph/9812320];
T. Hahn, S. Heinemeyer, W. Hollik and G. Weiglein, in preparation;
The code is obtainable at `www.feynhiggs.de`.

[15] T. Omori, KEK-PREPRINT-98-237 *Presented at the 1st ACFA Workshop on Physics Detector at the Linear Collider, Beijing, China, 26-28 Nov 1998*.

[16] S. Riemann, *Fermion-Pair Production at a Linear Collider - A Sensitive Tool for New Physics Searches*, TESLA note LC-TH-2001-007.

[17] R. Casalbuoni et al., *Z′ indication from new APV data in Cesium and searches at linear colliders*, TESLA note LC-TH-2000-006.

[18] T. Hahn, S. Heinemeyer and G. Weiglein, Nucl. Phys. B **652** (2003) 229 [arXiv:hep-ph/0211204]; Nucl. Phys. Proc. Suppl. **116** (2003) 336 [arXiv:hep-ph/0211384].

[19] F. Franke and H. Fraas, Standard Model," Int. J. Mod. Phys. A **12** (1997) 479 [arXiv:hep-ph/9512366] and references therein.

[20] F. Franke, H. Fraas and A. Bartl, Phys. Lett. B **336** (1994) 415 [arXiv:hep-ph/9408217].

[21] F. Franke and H. Fraas, Z. Phys. C **72** (1996) 309 [arXiv:hep-ph/9511275].

[22] U. Ellwanger and C. Hugonie, Eur. Phys. J. C **5** (1998) 723 [arXiv:hep-ph/9712300].

[23] S. Hesselbach, F. Franke and H. Fraas, Eur. Phys. J. C **23** (2002) 149 [arXiv:hep-ph/0107080] and references therein.

[24] F. Franke and S. Hesselbach, Phys. Lett. B **526** (2002) 370 [arXiv:hep-ph/0111285].

[25] S. Hesselbach and F. Franke, arXiv:hep-ph/0210363.

[26] G. Moortgat-Pick, S. Hesselbach, F. Franke and H. Fraas, arXiv:hep-ph/9909549.

[27] S. Hesselbach, F. Franke and H. Fraas, arXiv:hep-ph/0003272.

[28] N. Ghodbane and H. U. Martyn, arXiv:hep-ph/0201233.

[29] B. C. Allanach *et al.*, Eur. Phys. J. C **25** (2002) 113 [eConf **C010630** (2001) P125] [arXiv:hep-ph/0202233].

[30] B. de Carlos and J. R. Espinosa, Phys. Lett. B **407** (1997) 12 [arXiv:hep-ph/9705315].

[31] S. Y. Choi, J. Kalinowski, G. Moortgat-Pick and P. M. Zerwas, Eur. Phys. J. C **22** (2001) 563 [Addendum-ibid. C **23** (2002) 769] [arXiv:hep-ph/0108117].

[32] M. Heyssler, R. Rückl, H. Spiesberger, Proceedings of the LC–Workshop, Sitges 1999 and private communication with H. Spiesberger.

[33] H. E. Haber an G. L. Kane, Phys. Rep. **117** (1985) 75.

[34] TESLA Technical Design Report, Part III, eds. R.-D. Heuer, D. Miller, F. Richard and P. Zerwas, [arXiv:hep-ph/0106315].

[35] Y. Kizukuri and N. Oshimo, Phys. Lett. **B 249** (1990) 449.

[36] S. Y. Choi, H. S. Song and W. Y. Song, Phys. Rev. **D 61** (2000) 075004.

[37] A. Bartl, H. Fraas, O. Kittel and W. Majerotto, [arXiv:hep-ph/0308141]; A. Bartl, H. Fraas, O. Kittel and W. Majerotto, [arXiv:hep-ph/0308143].

[38] A. Bartl, T. Kernreiter, O. Kittel, [arXiv:hep-ph/0309340].

[39] L. J. Hall and J. Polchinski, Phys. Lett. **B 152** (1989) 335.

[40] I. S. Altarev et al., Phys. Lett. **B 276** (1992) 242; I. S. Altarev et al., Phys. Atom. Nucl.**59** (1996) 1152 and Yad. Fiz. **59 N 7**; E. D. Commins, S. B. Ross, D. DeMille, B. C. Regan, Phys. Rev. **A 50** (1994) 2960.

[41] G. Moortgat-Pick, H. Fraas, A. Bartl and W. Majerotto, Eur. Phys. J. **C 9** (1999) 521; Erratum-ibid. **C 9** (1999) 549.

[42] G. Moortgat-Pick, in *Proc. of the APS/DPF/DPB Summer Study on the Future of Particle Physics (Snowmass 2001)* ed. N. Graf, eConf **C010630**, E3008 (2001) [arXiv:hep-ph/0202082]; G. Moortgat-Pick, A. Bartl, H. Fraas and W. Majerotto, Eur. Phys. J. C **18** (2000) 379.

[43] S. Y. Choi, H. S. Song and W. Y. Song, Phys. Rev. D **61** (2000) 075004 [arXiv:hep-ph/9907474].

[44] Y. Kizukuri and N. Oshimo, Phys. Lett. B **249** (1990) 449.

[45] G. Moortgat-Pick, H. Fraas, A. Bartl and W. Majerotto, Eur. Phys. J. C **9**, 521 (1999) [Erratum-ibid. C **9**, 549 (1999)] [arXiv:hep-ph/9903220].

[46] A. Bartl, H. Fraas, O. Kittel and W. Majerotto, arXiv:hep-ph/0308141.

[47] E. Boos, H. U. Martyn, G. Moortgat-Pick, M. Sachwitz, A. Sherstnev and P. M. Zerwas, Eur. Phys. J. C **30** (2003) 395 [arXiv:hep-ph/0303110];

[48] A. Bartl et al., Eur. Phys. J. direct C **2** (2000) 6.

[49] A. Bartl et al., Z. Phys. C **76** (1997) 549; H. Eberl, A. Bartl and W. Majerotto, Nucl. Phys. B **472** (1996) 481; H. Eberl, S. Kraml and W. Majerotto, JHEP **9905** (1999) 016; S. Kraml, arXiv:hep-ph/9903257.

[50] M. Berggren et al., arXiv:hep-ph/9911345.

[51] T. Abe, S. Chen, B. Dobos, T. Dorland, J. Goodson, J. Gray, A. Han, A. Martinez, U. Nauenberg, J. Proulx, *Positron Polarization and Supersymmetry Measurements*

[52] Graham Wilson, LC-PHSM-2001-010

[53] L. Vacavant, I. Hinchcliffe, ATL-PHYS-2000-016, hep-ex/0005033.

[54] E. Eichten, K. Lane and M. E. Peskin, Phys. Rev. Lett. **50** (1983) 811;
R. Rückl, Phys. Lett. B **129** (1983) 363.

[55] A. A. Babich, P. Osland, A. A. Pankov and N. Paver, Phys. Lett. B **518** (2001) 128 [hep-ph/0107159].

[56] A. A. Babich, P. Osland, A. A. Pankov and N. Paver, LC Note LC-TH-2001-021 (2001), hep-ph/0101150.

[57] A. A. Babich, P. Osland, A. A. Pankov and N. Paver, Phys. Lett. B **481** (2000) 263 [hep-ph/0003253].

[58] K. Flottmann, DESY-95-064;

[59] K. Fujii and T. Omori, KEK-PREPRINT-95-127.

[60] B. Schrempp, F. Schrempp, N. Wermes and D. Zeppenfeld, Nucl. Phys. B **296** (1988) 1.

[61] W.T. Eadie, D. Drijard, F.E. James, M. Roos, B. Sadoulet, *Statistical methods in experimental physics* (American Elsevier, 1971).

[62] F. Cuypers and P. Gambino, Phys. Lett. B **388** (1996) 211 [hep-ph/9606391];
F. Cuypers, hep-ph/9611336.

[63] C. J. S. Damerell, D.J. Jackson, in *Proceedings of the 1996 DPF/DPB Summer Study on New Directions for High Energy Physics* (Snowmass 96), Edited by D.G. Cassel, L. Trindle Gennari, R.H. Siemann (SLAC, 1997) p. 442.

[64] A. A. Pankov and N. Paver, [hep-ph/0209058], to appear in Eur. Phys. J. C.

[65] N. Arkani-Hamed, S. Dimopoulos and G. R. Dvali, Phys. Lett. B **429** (1998) 263 [hep-ph/9803315].

[66] For a review see, *e.g.*, J. Hewett and M. Spiropulu, Ann. Rev. Nucl. Part. Sci. **52** (2002) 397 [hep-ph/0205106].

[67] J. L. Hewett, Phys. Rev. Lett. **82** (1999) 4765 [hep-ph/9811356].

[68] P. Osland, A. A. Pankov and N. Paver, [hep-ph/0304123], to be published in Phys. Rev. D.

[69] T. G. Rizzo, Phys. Rev. D **59** (1999) 113004 [hep-ph/9811440].

[70] B. Ananthanarayan and S. D. Rindani, arXiv:hep-ph/0309260.

[71] G. V. Dass and G. G. Ross, Phys. Lett. B **57** (1975) 173; G. V. Dass and G. G. Ross, Nucl. Phys. B **118** (1977) 284.

[72] K. Hagiwara, R. D. Peccei, D. Zeppenfeld and K. Hikasa, Nucl. Phys. B **282** (1987) 253.

[73] M. Diehl, O. Nachtmann and F. Nagel, Eur. Phys. J. C **27** (2003) 375 [arXiv:hep-ph/0209229].

[74] ALEPH Collaboration, Eur. Phys. J. C **21** (2001) 423 [arXiv:hep-ex/0104034];
DELPHI Collaboration, Phys. Lett. B **459** (1999) 382;
L3 Collaboration, Phys. Lett. B **467** (1999) 171 [arXiv:hep-ex/9910008];
L3 Collaboration, Phys. Lett. B **487** (2000) 229 [arXiv:hep-ex/0007005];

[75] G. Abbiendi *et al.* [OPAL Collaboration, Eur. Phys. J. C **19** (2001) 1 [arXiv:hep-ex/0009022];
OPAL Collaboration, Eur. Phys. J. C **19** (2001) 229 [arXiv:hep-ex/0009021].

[76] M. Pohl and H. J. Schreiber, DESY-99-030

[77] R. . (. Brinkmann, G. . (. Materlik, J. . (. Rossbach and A. . (. Wagner, DESY-97-048

[78] F. Franco-Sollova, LC note.

[79] M. Diehl, O. Nachtmann and F. Nagel, arXiv:hep-ph/0306247.

[80] M. Diehl and O. Nachtmann, Z. Phys. C **62** (1994) 397.

[81] M. Diehl and O. Nachtmann, Eur. Phys. J. C **1** (1998) 177 [arXiv:hep-ph/9702208].

[82] W. Menges, *A Study of Charged Current Triple Gauge Couplings at TESLA*, LC-PHSM-2001-022.

[83] W. Bernreuther, U. Löw, J. P. Ma and O. Nachtmann, Z. Phys. C **43** (1989) 117; J. G. Körner, J. P. Ma, R. Münch, O. Nachtmann and R. Schöpf, Z. Phys. C **49** (1991) 447.

[84] W. Bernreuther, G. W. Botz, D. Bruß, P. Haberl and O. Nachtmann, Z. Phys. C **68** (1995) 73 [arXiv:hep-ph/9412268]; P. Haberl, arXiv:hep-ph/9611430.

[85] D. Buskulic *et al.* [ALEPH Collaboration], Phys. Lett. B **384** (1996) 365.

[86] O. Nachtmann and C. Schwanenberger, Eur. Phys. J. C **9** (1999) 565 [arXiv:hep-ph/9901343]; O. Nachtmann and C. Schwanenberger, Eur. Phys. J. C **13** (2000) 315 [arXiv:hep-ph/9909527].

[87] T. Pauly, "Suche nach CP-Verletzung in den 4-Jet-Zerfällen des Z^0", Diploma thesis, University of Heidelberg (unpublished).

[88] F. Richard, J. R. Schneider, D. Trines and A. Wagner, "TESLA Technical Design Report Part I: Executive Summary," arXiv:hep-ph/0106314;

[89] O. Nachtmann and C. Schwanenberger, Eur. Phys. J. C **32** (2004) 253 [arXiv:hep-ph/0308198].

[90] W. Bernreuther, A. Brandenburg, P. Haberl and O. Nachtmann, Phys. Lett. B **387** (1996) 155 [arXiv:hep-ph/9606379]; W. Bernreuther and O. Nachtmann, Eur. Phys. J. C **9** (1999) 319 [arXiv:hep-ph/9812259].

[91] U. Baur, I. Hinchliffe and D. Zeppenfeld, Int. J. Mod. Phys. A **2** (1987) 1285; U. Baur, M. Spira and P. M. Zerwas, Phys. Rev. D **42** (1990) 815.

[92] T. Han and J. L. Hewett, Phys. Rev. D **60** (1999) 074015 [arXiv:hep-ph/9811237].

[93] J. L. Hewett and T. G. Rizzo, Phys. Rept. **183**, 193 (1989).

[94] A. Leike, Phys. Rept. **317**, 143 (1999) [arXiv:hep-ph/9805494]; M. Cvetic and S. Godfrey, arXiv:hep-ph/9504216.

[95] W. Buchmuller, R. Ruckl and D. Wyler, Phys. Lett. B **191**, 442 (1987) [Erratum-ibid. B **448**, 320 (1999)]; J. L. Hewett and T. G. Rizzo, Phys. Rev. D **58**, 055005 (1998) [arXiv:hep-ph/9708419], Phys. Rev. D **56**, 5709 (1997) [arXiv:hep-ph/9703337] and Phys. Rev. D **36**, 3367 (1987).

[96] J. Kalinowski, R. Ruckl, H. Spiesberger and P. M. Zerwas, Phys. Lett. B **414**, 297 (1997) [arXiv:hep-ph/9708272]; J. Kalinowski, R. Ruckl, H. Spiesberger and P. M. Zerwas, Phys. Lett. B **406**, 314 (1997) [arXiv:hep-ph/9703436]; T. G. Rizzo, Phys. Rev. D **59**, 113004 (1999) [arXiv:hep-ph/9811440].

[97] F. Cuypers and S. Davidson, Eur. Phys. J. C **2**, 503 (1998) [arXiv:hep-ph/9609487].

[98] J. L. Hewett, Phys. Rev. Lett. **82**, 4765 (1999) [arXiv:hep-ph/9811356]; G. F. Giudice, R. Rattazzi and J. D. Wells, Nucl. Phys. B **544**, 3 (1999) [arXiv:hep-ph/9811291]; T. Han, J. D. Lykken and R. J. Zhang, Phys. Rev. D **59**, 105006 (1999) [arXiv:hep-ph/9811350]; T. G. Rizzo, Phys. Rev. D **59**, 115010 (1999) [arXiv:hep-ph/9901209].

[99] For an overview of RS phenomenology, see H. Davoudiasl, J. L. Hewett and T. G. Rizzo, Phys. Rev. D **63**, 075004 (2001) [arXiv:hep-ph/0006041]; Phys. Lett. B **473**, 43 (2000) [arXiv:hep-ph/9911262]; Phys. Rev. Lett. **84**, 2080 (2000) [arXiv:hep-ph/9909255]; J. L. Hewett, F. J. Petriello and T. G. Rizzo, JHEP **0209**, 030 (2002) [arXiv:hep-ph/0203091].

[100] N. Arkani-Hamed, S. Dimopoulos and G. R. Dvali, Phys. Lett. B **429**, 263 (1998) [arXiv:hep-ph/9803315]; I. Antoniadis, N. Arkani-Hamed, S. Dimopoulos and G. R. Dvali, Phys. Lett. B **436**, 257 (1998) [arXiv:hep-ph/9804398]; N. Arkani-Hamed, S. Dimopoulos and G. R. Dvali, Phys. Rev. D **59**, 086004 (1999) [arXiv:hep-ph/9807344].

[101] L. Randall and R. Sundrum, Phys. Rev. Lett. **83**, 3370 (1999).

[102] See, for example, I. Antoniadis, Phys. Lett. B **246**, 377 (1990); T. G. Rizzo and J. D. Wells, Phys. Rev. D **61**, 016007 (2000) [arXiv:hep-ph/9906234]; M. Masip and A. Pomarol, Phys. Rev. D **60**, 096005 (1999) [arXiv:hep-ph/9902467]; T. G. Rizzo, Phys. Rev. D **64**, 015003 (2001) [arXiv:hep-ph/0101278].

[103] S. Cullen, M. Perelstein and M. E. Peskin, Phys. Rev. D **62**, 055012 (2000) [arXiv:hep-ph/0001166].

[104] G. Pasztor and M. Perelstein, in *Proc. of the APS/DPF/DPB Summer Study on the Future of Particle Physics (Snowmass 2001)* ed. R. Davidson and C. Quigg, arXiv:hep-ph/0111471.

[105] R. Budny, Phys. Rev. **D14**, 2969 (1976); H.A. Olsen, P. Osland and I. Overbo, Phys. Lett. **B97**, 286 (1980); K. Hikasa, Phys. Rev. **D33**, 3203 (1986); C.P. Burgess and J.A. Robinson, Int. J. Mod. Phys. **A6**, 2709 (1991); A. Djouadi, F.M. Renard and C. Verzegnassi, Phys. Lett. **B241**, 260 (1990); F.M. Renard, Z. Phys. **C44**, 75 (1989); J.L. Hewett and T.G. Rizzo, Z. Phys. **C36**, 209 (1987); for a recent discussion of this option at the LC, see K. Desch, talk given at the *International Workshop on the Linear Collider, LCWS2002*, Jeju Island, Korea, Aug. 2002.

[106] J. Fleischer, K. Kolodziej and F. Jegerlehner, Phys. Rev. **D49**, 2174 (1994.)

[107] G. Moortgat-Pick, private communication.

[108] T.G. Rizzo, JHEP 0210 013 2002.

[109] E. Eichten, K. Lane and M. Peskin, Phys. Rev. Lett. **50**, 811 (1983).

[110] J. A. Aguilar-Saavedra *et al.* [ECFA/DESY LC Physics Working Group Collaboration], "TESLA Technical Design Report Part III: Physics at an e+e- Linear Collider," arXiv:hep-ph/0106315; S. Riemann, TESLA Linear Collider Note LC-TH-2001-007'

[111] For a review of the current and anticipated future collider reaches for extra dimensions, see J. Hewett and M. Spiropulu, "Particle physics probes of extra spacetime dimensions," arXiv:hep-ph/0205106.

[112] A. Datta, E. Gabrielli and B. Mele, hep-ph/0210318.

[113] More details can be found in T.G. Rizzo, JHEP 0302 008 2003.

[114] G. Corcella *et al.*, interfering gluons (including supersymmetric processes)," JHEP **0101** (2001) 010 [hep-ph/0011363]; G. Corcella *et al.*, hep-ph/0210213.

[115] H. Baer, F. E. Paige, S. D. Protopopescu and X. Tata, hep-ph/0001086.

[116] T. Sjöstrand, P. Edén, C. Friberg, L. Lönnblad, G. Miu, S. Mrenna and E. Norrbin, Comput. Phys. Commun. **135** (2001) 238 [hep-ph/0010017]; T. Sjöstrand, L. Lönnblad and S. Mrenna, hep-ph/0108264.

[117] P. Richardson, JHEP **0111**, 029 (2001) [hep-ph/0110108].

[118] R. Kuhn, F. Krauss, B. Ivanyi and G. Soff, Comput. Phys. Commun. **134**, 223 (2001) [hep-ph/0004270]. `SHERPA` is available from: `http://www.physik.tu-dresden.de/~krauss/hep/`.

[119] M. Bertini, L. Lönnblad and T. Sjöstrand, Comput. Phys. Commun. **134**, 365 (2001) [hep-ph/0006152].

[120] S. Gieseke, hep-ph/0210294.

[121] M. Kobel *et al.*, hep-ph/0007180.

[122] M. W. Grunewald *et al.*, hep-ph/0005309.

[123] S. Dittmaier and M. Roth, Nucl. Phys. B **642**, 307 (2002) [hep-ph/0206070].

[124] G. Montagna, M. Moretti, O. Nicrosini and F. Piccinini, Eur. Phys. J. C **2**, 483 (1998) [hep-ph/9705333];
F. Gangemi *et al.*, Eur. Phys. J. C **9**, 31 (1999) [hep-ph/9811437] and Nucl. Phys. B **559**, 3 (1999) [hep-ph/9905271];
F. Gangemi, hep-ph/0002142.

[125] K. Kołodziej, Eur. Phys. J. C **23**, 471 (2002) [hep-ph/0110063] and Comput. Phys. Commun. **151**, 339 (2003) [hep-ph/0210199];
A. Biernacik and K. Kołodziej, Nucl. Phys. Proc. Suppl. **116** (2003) 33 [hep-ph/0210405].

[126] E. Accomando, A. Ballestrero and M. Pizzio, Nucl. Phys. B **547** (1999) 81 [hep-ph/9807515];
E. Accomando, A. Ballestrero and M. Pizzio, hep-ph/9709277.

[127] F. Krauss, R. Kuhn, and G. Soff, JHEP **02**, 044 (2002) [hep-ph/0109036].

[128] A. Pukhov *et al.*, hep-ph/9908288. `COMPHEP` is available from:
`http://theory.sinp.msu.ru/comphep/`.

[129] MINAMI-TATEYA group, T. Ishikawa *et al.*, KEK-92-19. `GRACE` is available from:
`http://minami-home.kek.jp/`.

[130] A. Kanaki and C. G. Papadopoulos, Comput. Phys. Commun. **132**, 306 (2000) [hep-ph/0002082].

[131] C. G. Papadopoulos, Comput. Phys. Commun. **137**, 247 (2001) [hep-ph/0007335].

[132] F. Maltoni and T. Stelzer, JHEP **02**, 027 (2003) [hep-ph/0208156];
T. Stelzer and W. F. Long, Comput. Phys. Commun. **81**, 357 (1994) [hep-ph/9401258].
`MADGRAPH/MADEVENT` is available from:
`http://madgraph.physics.uiuc.edu/`.

[133] H. Murayama, I. Watanabe and K. Hagiwara, KEK-91-11.

[134] T. Ohl, hep-ph/0011287;
W. Kilian, LC-TOOL-2001-039 *In '2nd ECFA/DESY Study 1998-2001', 1924-1980*.
`WHIZARD` is available from:
`http://www-ttp.physik.uni-karlsruhe.de/Progdata/whizard/`. For `O'MEGA`, see:
`http://heplix.ikp.physik.tu-darmstadt.de/~ohl/omega/`.

[135] F. Caravaglios and M. Moretti, Phys. Lett. **B358**, 332 (1995) [hep-ph/9507237].

[136] M. Moretti, T. Ohl, and J. Reuter, hep-ph/0102195.

[137] E. Boos *et al.*, hep-ph/0109068.

[138] N. Ghodbane, hep-ph/9909499;
S. Katsanevas and P. Morawitz, Comput. Phys. Commun. **112**, 227 (1998) [hep-ph/9711417]. `SUSYGEN` is available from:
`http://lyoinfo.in2p3.fr/susygen/susygen3.html`.

[139] T. Omori, T. Aoki, K. Dobashi, T. Hirose, Y. Kurihara, T. Okugi, I. Sakai, A. Tsunemi, J. Urakawa, M. Washio, K. Yokoya, Nucl. Instr. Meth **A500**, 232 (2003) and Nucl. Instr. Meth. **A503**, 658 (2003).

[140] K. Abe et al., KEK Report 2003-7.

[141] K. Yokoya, CAIN, http://www-acc-theory.kek.jp/members/cain/default.html

[142] I. Sakai, T. Aoki, K. Dobashi, M. Fukuda, A. Higurashi, T. Hirose, T. Iimura, Y. Kurihara, T. Okugi, T. Omori, J. Urakawa, M. Washio, and K. Yokoya Phys. Rev. ST Accel. Beams **6**, 091001 (2003).

[143] M. Fukuda, T. Aoki, K. Dobashi, T. Hirose, T. Iimura, Y. Kurihara, T. Okugi, T. Omori, I. Sakai, J. Urakawa, and M. Washio, Phys. Rev. Lett. **91**, 164801 (2003).

[144] D. Cinabro, E. Torrence and M. Woods, Status of (Next) Linear Collider Beam Instrumentation Design, LCD-ALCPG-03-0001 (2003); M. Woods, Int.J.Mod.Phys. A13 (1998) 2517. [hep-ex/9802009]

[145] P.C. Rowson and M. Woods, SLAC-PUB-8745. [hep-ex/0012055]

[146] Y.M. Nosochkov and K. A. Thompson, LCC-0049, 2000.

[147] Y.M. Nosochkov and T.O. Raubenheimer, SLAC-PUB-8313, 1999.

[148] Kathleen A. Thompson, SLAC-PUB-8716, 2001.

[149] K. Yokoya and P. Chen. SLAC-PUB-4692, 1988.

[150] M. L. Swartz, Phys.Rev. D58 (1998) 014010. [hep-ph/9711447]

[151] M. Woods, SLAC-PUB-7319, 1996.

[152] D. V. Onoprienko, SLAC-Report-556, 2000.

[153] M. Bilenky et al., Nucl. Phys. **B409** (1993) 22.

[154] K. Mönig, *The use of Positron Polarisation for precision Measurements*, LC-PHSM-2000-59

[155] S. Jadach et al. Comp. Phys. Comm. **130** (2000) 260.

[156] P. Chenand, T. Ohgaki, T. Takahashi, A. Spitkovsky and K. Yokoya, Nucl.Instr.Meth. **A397**, 458 (1997).